ADVANCEMENT OF BLINKING SUPPRESSED QUANTUM DOTS FOR ENHANCED SINGLE MOLECULE IMAGING

A Dissertation
Presented to
The Academic Faculty

by

Lucas A. Lane

In Partial Fulfillment
of the Requirements for the Degree
Doctor of Philosophy in the
Department of Biomedical Engineering

Georgia Institute of Technology
August, 2014

ADVANCEMENT OF BLINKING SUPPRESSED QUANTUM DOTS

FOR ENHANCED SINGLE MOLECULE IMAGING

Approved by:

Dr. Shuming Nie, Advisor
School of Biomedical Engineering
Georgia Institute of Technology

Dr. Younan Xia
School of Biomedical Engineering
Georgia Institute of Technology

Dr. Mostafa El-Sayed
School of Chemistry
Georgia Institute of Technology

Dr. Gang Bao
School of Biomedical Engineering
Georgia Institute of Technology

Dr. Adam Marcus
School of Oncology
Emory University

Date Approved: May 2, 2014

ACKNOWLEDGEMENTS

First, I wish to thank my family for their support and help throughout my life. The closeness and care received, even from multiple extended family members, made a childhood which started with a great tragedy a joyous one. Next, I would like to thank all of the Nie group members for supporting such a great collaborative and welcoming atmosphere to work in. I am also grateful for the multiple professors who have helped and inspired me of whom were either instructors of classes I have taken or guided research I have been involved in which include: Younan Xia, Carl M. Bender, Mohan Srinivasarao, Uzi Landman, James M. McKelvey, Amyn Teja, Cynthia Lo, Amy Shen, Radhakrishna Sureshkumar, and Anders Carlsson. Tim Lian and his research group are acknowledged for providing and assisting with the spectroscopy tools used in a significant portion of this dissertation work. Finally, I would like to thank my graduate research advisor Shuming Nie for the plentitude of expert advice, guidance, and motivational support he has given me over the course of five years. In addition, I am truly appreciative for the abundant freedom in which Dr. Nie allows in one's research which has enabled me to learn a great deal in a number of different scientific disciplines.

TABLE OF CONTENTS

LIST OF FIGURES

SUMMARY

Semiconductor nanocrystalline quantum dots (QDs) have been intensely studied in bioimaging applications due to their exceptional optical properties such as size-tunable narrow emission spectra, broad absorption envelopes, and high resistance to chemical and photodegradation in comparison to conventional fluorophores or fluorescent proteins. An inherent problem that quantum dots have shared with other single emitters is fluorescent intermittency, or otherwise referred to as blinking. The blinking of a single molecule or single QD refers to random transitions amid absorption and emission cycles followed by sustained intervals of time without fluorescence regardless of continuous laser excitation. Frequent and prolonged off times raise difficulties in correspondence between frames when tracking the position of single molecules in cellular experiments due to cells not being homogeneous vessels with a single diffusion coefficient. In the last six years there has been success suppressing the blinking of quantum dots in practice, but were limited to thick shell particles with large diameters, gradient dots with overlapping multi-peak emission, or immersing the probes in specific solutions of reducing reagents. All of these methods present major difficulties when considering application to live molecular tracking experiments. Within the past year, however, efforts have demonstrated success in overcoming a few of these hurdles, but still lack a general methodology in creating blinking suppressed probes. Among these reports, only one to date has demonstrated single molecule tracking potential.

This study composes a generalizable framework by means of physical-chemical theory undertaking the mechanisms of fluorescent intermittency and synthesis measures designed in light of this information, to develop blinking suppressed particles which are better suited for single molecule imaging than currently available QDs and validates their use in a biological setting. Such probes were found to provide superior frame correspondence in trajectory reconstruction of tracking studies due to having short-infrequent off times. Controlling blinking towards brief and infrequent off times offer negligible signal loss, leading to continuous dynamical information at higher acquisition rates. In addition to the enhanced on times, the emission spectra were observed to be single peaked with thin full width at half maximums (FWHMs) due to synthesis techniques preserving monodispersity, thus permitting multiplexed single molecule tracking of different species.

The innovation of the study is synthesizing QDs within a general framework that have greatly diminished fluorescent off times while preserving small sizes, solution independency, and no multi-peak emission. The work presented yields the following outcomes: First, it establishes a general structure based on theoretical forethought in which to synthesize blinking suppressed imaging probes. Next, synthesis techniques are developed to produce QDs with the structure outlined within the general framework. Finally, a comparative test of blinking suppressed to conventional core/shell particles elucidating the benefits is shown in a single molecule tracking experiment. These studies present that when adhering to the prescribed framework outlined, one can produce blinking suppressed QDs with sensible sizes for single molecule tracking experiments with minimal signal loss.

CHAPTER 1

INTRODUCTION

The prefix of nano originates from the Greek word for dwarf. One nanometer (nm) is quite small as it is just one billionth of a meter. To put this into perspective, the width of a human hair is near 100,000 nm wide. The first conceptualization of using technologies on such a small length scale was presented by Richard Feynman in the lecture, "There's plenty of room at the bottom." In this lecture Feynman proposed one could manipulate and order atoms in such a way that the entire Encyclopedia Britannica could be written on the head of a pin. Not too long after, IBM within the efforts of the electronic industry to miniaturize devices, developed the use of electron beam lithography to create objects less than 100 nm.

Research in the optical properties of nanosized particles actually dates back to the time of Faraday's experiments of colloidal solutions, though unknowingly of the exact sizes of the samples. In these experiments, Faraday witnessed the extraordinary dependence of gold's color based only on particulate size without changes in the material's chemical composition. More than one hundred years later, the optical properties of nanometer sized crystals composed of semiconductor materials too were shown to depend on size by Ekimov and co-workers in their experiments on semiconductor-doped glasses. Since then research towards understanding and utilizing

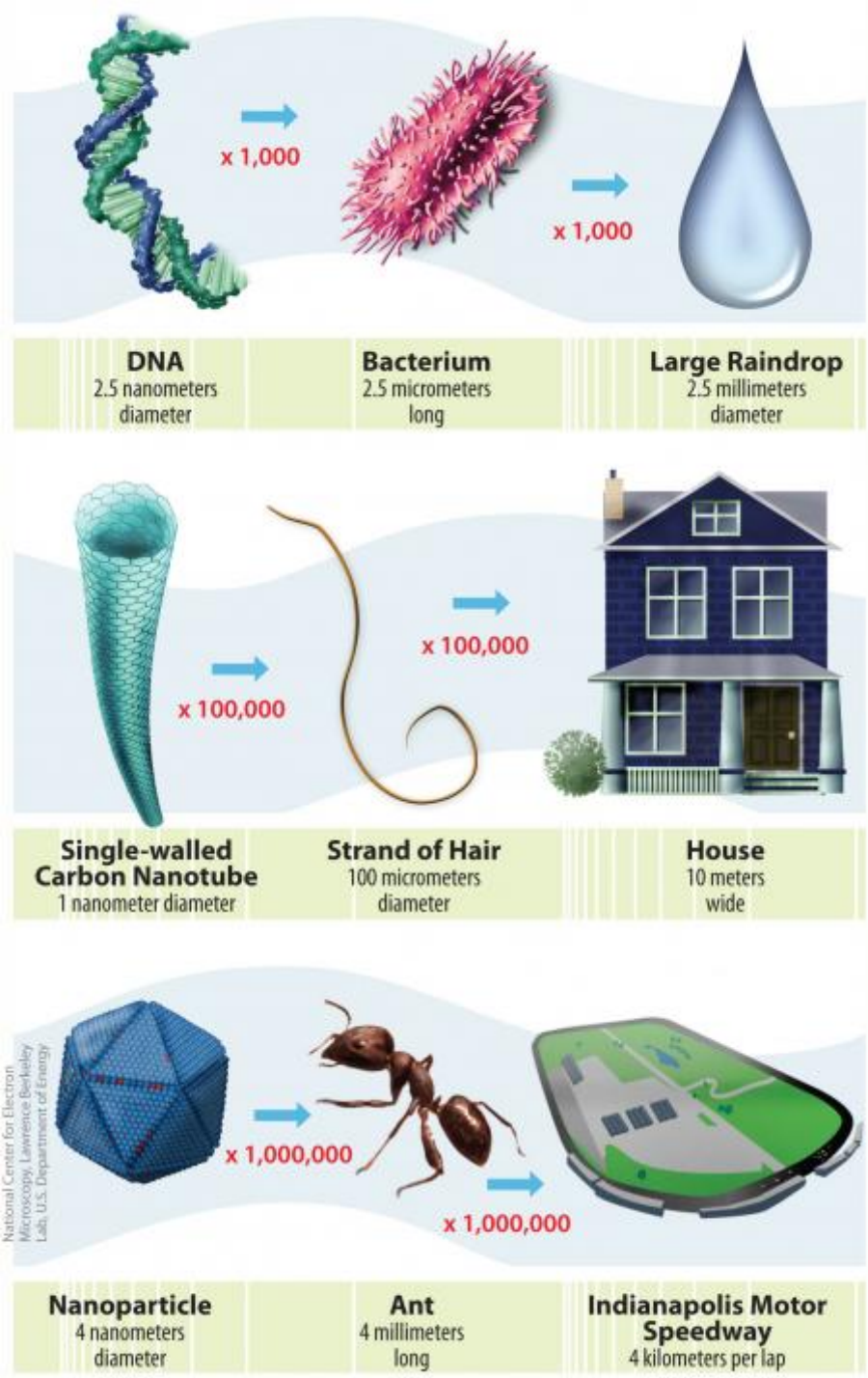

Figure 1.1 The Size and Scale of Nanotechnology. Illustration showing how small nanometer sized objects are. [From National Nanotechnology Initiative]

the physical properties of semiconductor nanocrystals, otherwise known as quantum dots (QDs), has been developing at a rapid pace. Interest in QDs was originally motivated by more scholarly aims to comprehend these particles' unique optical and spectroscopic features, but has of late been advanced by numerous technological developments for useful applications. In addition to typical semiconductor material applications in electro-optical devices, such as light emitting diodes,[1-4] and photovoltaic cells,[5,6] there are also abundant uses of QDs in biological based technologies as well.[7-12]

The prevalent biological application of fluorescence labeling biomolecules as a means for implementing immunoassays, cellular labeling, and tissue imaging, traditionally relied on organic molecule based fluorophores and fluorescent proteins.[13-15] These routinely used organic dyes and fluorescent proteins, however, have inherent disadvantages that limit successful use in targeted imaging applications. Such limitations include narrow absorption envelopes, broad photoluminescence spectra, and poor resistance to chemical and photodegradation.[16-18] Photoluminescent QDs, on the other hand, offer several distinctive properties which present considerable advantages over traditional organic and protein fluorophores.[17,19-22] For instance, QDs have light emission over a broad range of wavelengths in the visible and near infrared (NIR) regions of the electromagnetic spectrum depending on the material composition and size of the particles,[16,23-25] of which the size can be tuned by growth times during synthesis. Such emission can be considerably brighter than traditional fluorophores owing to a greater absorption cross section in addition to high quantum yields, thus leading to improved signal to noise ratios in fluorescence imaging experiments. Moreover, because they have

broad absorption envelopes, spanning from the ultraviolet (UV) to the band edge, it is feasible to simultaneously excite different color QDs with a single wavelength, making them naturally appropriate for multiplexing applications.

A difficulty of which quantum dots shared with conventional fluorophores, one that is of great significance in the intended application of single molecule tracking of this study, is fluorescent intermittency or more commonly called blinking. Blinking is referred to the random interchanging between bright (where light is fluoresced) and dark periods (where no light is fluoresced) during continuous laser excitation which seems to be universal among all fluorophores including organic emitters[26] as well as inorganic quantum dots, wires, and rods.[27] Apart from fluorescent dyes which have typical nonradiative intervals of 0.5 ms (but can subsequently photobleach), commercially available QDs can show dark periods of up to 100 seconds (though do not photobleach), consequently preventing their use for single molecule tracking in cellular studies where diffusion coefficients can near 1 $\mu m^2/s$.[28] Long off times such as 100 seconds, translating to diffusive length scales near the size of the entire cell (~10 μm), create significant difficulties in the correspondence between frames of an image stack in a tracking study.[29] Though there are algorithms used to reconstruct the missing trajectories when a QD was in an off state,[30-32] these have limited accuracy for long off states as cells are very heterogeneous and dynamic which is far from a well-mixed vessel to be precisely described with a single constant isotropic diffusion coefficient.[33] Advancing QDs in single molecule studies necessitates control of blinking to truly take advantage of the distinctive optical properties over conventional fluorophores.

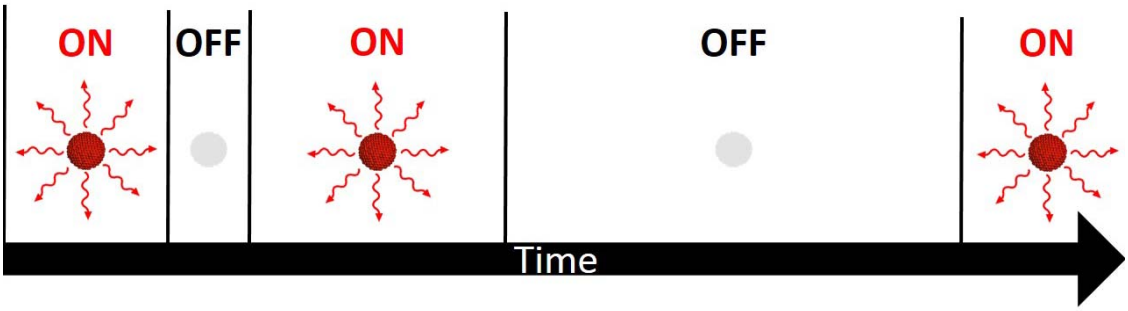

Figure 1.2 Quantum Dot Blinking. Depiction of the switching among fluorescent (on) and nonfluorescent (off) state periods of a quantum dot with time under continuous excitation.

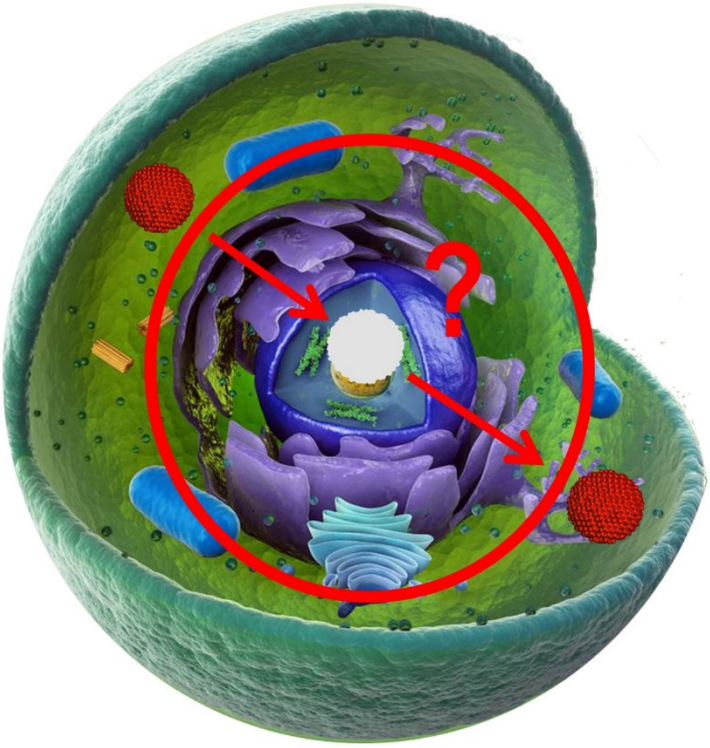

Figure 1.3 Path Uncertainty for a Quantum Dot in an Off State. A QD in a prolonged off state can travel the length of an entire cell before returning to an emissive state. Such situations leave large regions of uncertainty in the path traveled by the QD.

After blinking was first observed in the fluorescence of single QDs,[34] several researchers embarked on a journey to comprehend the mechanisms and develop methodologies to suppress and perhaps entirely eliminate this blinking phenomena. QD blinking is generally associated with the physical mechanisms of Auger recombination and carriers being accepted into trap states.[35] Theoretical studies to date have primarily narrowed on the Auger process where the energy of an exciton is transferred nonradiatively into another charge carrier.[36-41] Experimental measures which have been employed to diminish blinking have included; solvating the particles in solutions of short chain thiols[42] or propyl gallate,[43] adding multiple monolayers of cadmium sulfide (CdS) shell material around a cadmium selenide (CdSe) QD core,[44] or through smooth parabolic gradient shells created by diffusing zinc cations into CdSe QDs.[45] Solution based blinking suppression methods of beta-mercaptoethanol or propyl gallate require concentrations in the millimolar range to be effective. Such high concentrations of these agents are beyond the micromolar range found in culture mediums and the amount to induce apoptosis in cells.[46] Therefore solution based strategies cannot be used for live cell single molecule tracking experiments. For the multiple monolayer shelled QDs, otherwise known as the giant shell QDs, have size ranges that can near 20 nm. This is about twice the hydrodynamic size of IgG,[47] which can significantly alter the dynamics of the tagged biomolecule, especially when considering the additional size from the solvating ligands required to stabilize the particle in solution. Though more recently there has been a couple of reports showing blinking suppression using less monolayers of CdS shell surrounding a CdSe core than the giant QDs,[48,49] methods beyond using these two materials must be developed if a wider variety of fluorescent wavelengths are to be utilized for biological tracking experiments. In addition, a more generalized

method for blinking suppression should be able to extend to multiple material systems. The nonblinking gradient alloy QDs[45] have smaller size ranges and a more generalizable method towards creating blinking suppressed probes using other materials, but the diffusion of cations into the QD core to create the required parabolic gradient profile claimed to be optimal in blinking suppression is difficult to control and reproduce. Therefore, in order to expand the applicability of blinking suppressed probes, a synthesis method that combines a generalizable method like the parabolic gradient alloy QDs while using a facile approach in likeness to the giant shell QDs is needed.

The first article on tracking single biological molecules using QDs was published more than a decade ago[11] and since several studies have followed showing motions of individually QD labeled plasma membrane proteins and lipids.[50-52] Especially in neurobiology, QDs have found great use to study the motion of single specific receptors in synapses under various cellular conditions and stimuli.[53] Despite the increasing number in blinking suppressed quantum dot papers along with single molecule tracking research using QDs, only a couple of articles known to date have been circulated using blinking suppressed probes in single molecule tracking studies.[54,55] Therefore, there is a great void in the scientific community of research in using blinking suppressed probes in single molecule tracking.

1.1 Thesis Themes and Structure

This thesis has the following themes: First, it presents a shell composition profile backed by physical theory in designing blinking suppressed probes. Next, it frames a synthetic route which is favorable in producing particles with the intended shell composition profile. Finally, the fluorescent intermittency properties of the blinking suppressed quantum dots are evaluated and a comparative study to conventional (more blinking) core/shell QDs are performed in a cellular single molecule tracking experiment. Below is are brief descriptions for each chapter of the dissertation.

Chapter 1- Here QD blinking in single molecule tracking is introduced along with the themes and structure of the thesis.

Chapter 2- This chapter provides a review of the physics, chemistry, and biological applications of quantum dots to aid in the understanding of the dissertation work.

Chapter 3- The design and synthesis measures for creating blinking suppressed quantum dots are presented in this section.

Chapter 4- In this chapter the fluorescent behavior of the blinking suppressed probes are inspected on the single particle level through time correlated single photon counting.

Chapter 5- Here a single molecule tracking experiment is performed on cellular membrane receptors comparing diffusional and trajectory data from the blinking suppressed quantum dots and commercially available ones.

Chapter 6- Finally, a rundown is given for each chapter emphasizing the main findings and conclusions. Afterwards, ideas are presented for future directions to build upon the work of this dissertation.

1.2 Conclusion

Blinking suppressed probes can have a great impact in biological single molecule tracking studies. Single molecule research has already revealed secrets in nature including EGFR signaling,[56] infection pathways of viruses,[57] and the thermodynamics of nucleosome deposition on DNA.[58] As knowledge about the mechanisms of the cell and infectious agents grows, we can develop better cures for aberrations of cellular processes such as cancer or prevent cell invasion from viruses. Having better tools to obtain this information will accelerate the gain of understanding such life processes. It is believed that blinking suppressed particles could be used to help obtain such dynamical information without the need for interpolating data by an erroneous assumption of the system to be a small well mixed vessel when signals are lost for extended durations.

CHAPTER 2

PHYSICS, CHEMISTRY, AND BIOLOGICAL APPLICATIONS OF SEMICONDUCTOR NANOCRYSTALS

Spherically shaped nanometer sized (1-100 nm) crystals made of semiconductor materials, otherwise known as quantum dots (QDs), exhibit emergent phenomena which are not present in their bulk counterparts. The most fascinating property of these nanocrystals is that their absorption and photoluminescence properties can be tuned based on the size of the crystal. This is in stark contrast to what is observed in macroscopic objects, whereby cutting a material into smaller pieces one would observe no change in the material's optical properties. The effect where a difference in the nanometer size of semiconductor crystals does result in the change of its optical properties is termed quantum confinement which was discovered by Ekimov and Efros,[59,60] where smaller crystals result in larger band gaps. The increasing energy in the bandgap as particles get smaller is akin with the results one finds of higher energy levels from smaller barrier widths in the prototypical particle in a box example in quantum mechanics. Early synthesis methods of these crystals involved them being inclusions within bulk glasses, after which preferred colloidal synthesis methods were developed by Brus and Bawendi.[61-63] Colloidal methods proved to be robust and facile which aided in the great leap in number of researchers who sought to explore the multiple chemical and physical phenomena which are associated with these particles and apply these new effects in a multitude of applications. In particular, Alivisatos and Nie simultaneously demonstrated the first uses of QDs as biological fluorophores in 1998.[12,64] Since, there

has been a drastic increase in the interest and publication of work exploring the use of these nanocrystals in the biological field. In this chapter the physical, chemical, and biological foundation for this interest is presented. First, the important physical principles of semiconductors materials are detailed (**Section 2.1**), and the size-dependent properties of nanocrystals are discussed (**Section 2.2**). Next, the strategies used to chemically synthesize QDs are described (**Section 2.3**). Finally, relevant application of QDs to biological experiments are presented (**Section 2.4**).

2.1 Semiconductor Physics

The previous century has observed a great number of theoretical and experimental developments in semiconductor physics resulting in numerous electronic devices. The more recent interest in nanoscale semiconductor materials, such as QDs, along with the ubiquitous electronic devices in our daily lives moving to smaller platforms would indicate that such curiosities will endure for quite some time. Appreciation of the unique properties of semiconductor nanocrystals and their potential in a wide variety of applications necessitates an understanding of the fundamental concepts within semiconductor physics. This review of the physics of semiconductors is presented to offer a theoretical background for the research described in this thesis. More thorough explanations of solid state physics,[15] semiconductor physics,[18,19] quantum mechanics,[20,21] and quantum confinement[1,4,8] can be found within the cited literature.

2.1.1 The Electronic Bandgap

The solution to the time independent Schrodinger equation,

$$\frac{-\hbar^2}{2m}\nabla^2\psi + V\psi = E\psi \,, \tag{2.1}$$

of isolated atoms gives a series of discrete energy level values. Optical transitions amid these energy levels give rise to sharp lines in the absorption and emission spectra. As one may recall from a freshman chemistry class, these are the colorful lines in the spectra obtained from the atoms of an element. When moving to a solid with multiple atoms bonded together, however, more intricacy is placed into the admissible energy states of the system. Properties of the individual atoms of the solid are still present, but new physics arise such as the creation of continuous energy bands from the delocalization of the atomic states. The development of discrete energy levels in single atoms to continuous energy bands in a solid can be illustrated in the simplified example of particles in boxes to the Kronig Penney model of a one dimensional lattice of a periodic potential.

The discrete energy lines of a single atom can be envisioned by the prototypical example in quantum mechanics of the particle in a box, whereby an electron is confined in an infinite well potential. Considering a particle of mass m trapped in an infinite well of width a, after having solved the Schrodinger equation, one obtains energies which take on the values

$$E_n = \frac{h^2 n^2}{8ma^2} \ , \tag{2.2}$$

where n is integer values of 1, 2, etc. with wave function solutions of

$$\psi(x) = \sqrt{\frac{2}{a}} \sin\left(\frac{n\pi}{a} x\right). \tag{2.3}$$

Now consider the case where there is two equivalent square potentials separated by a barrier as shown in the **Figure 2.1**. If the barrier is high and/or wide enough, then the particle is prohibited from traveling from one well to the other resulting in two independent states, one for each well. When the separating barrier potential between the two wells is dropped enough, so that the well does not prevent the particle passage from one well to another, the two regions will be coupled. This coupling necessitates one Schrodinger equation to be solved for the entire system. Such a condition changes the previous results had for independent wells both having energy separations of the single well with an infinite potential. The coupling for this case creates a symmetric (lower in energy) and antisymmetric (higher in energy) solution from the originally two independent eigenstates. The result obtained is analogous to the LCAO approximation used in chemistry where the lower energy symmetric solution which has higher electron probability between the wells is the bonding state and the higher energy antisymmetric solution with less probability between the wells is the antibonding state.

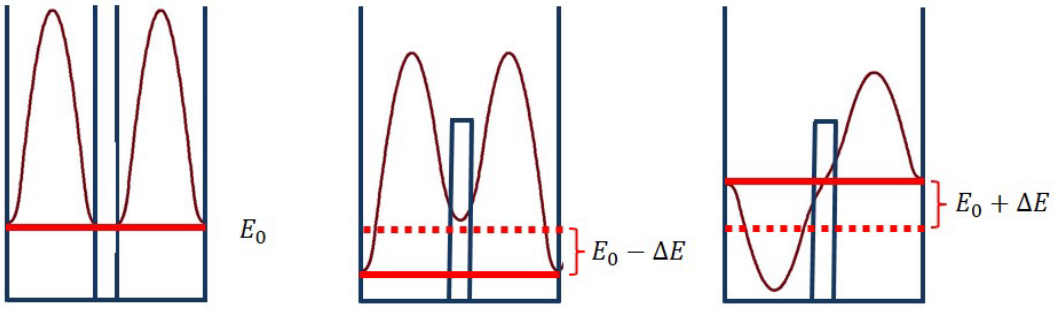

Figure 2.1 Coupling of Two Equivalent Potential Wells. Energy splitting as a result of allowing particles to cross the barrier between two separate equivalent wells.

Following the reasoning for the particles in two coupled wells, one can make an expectation as to what will happen when subsequently adding up to an infinite number of coupled wells. Beginning with N degenerate states of N individual wells and allow coupling between all neighboring wells, there will still be N states, but the states will have different energies subject to the linear combinations of the original single well states. Moving to a large number of cells, the change in a state's energy attained by adding or subtracting a single node in a linear combination will be minute. Therefore, the states will become tightly spaced in energy. With large numbers of tightly spaced energy levels, the jumps in energy between these states will be so small that an electron can move continuously within this range. This range of continuous energy levels is what is called an energy band. In between energy bands are energy gaps, or bandgaps. These gaps arise from the space between discrete energy levels in the original single well states. A pictorial description of the process of the states developing into energy bands is provided in **Figure 2.2**.

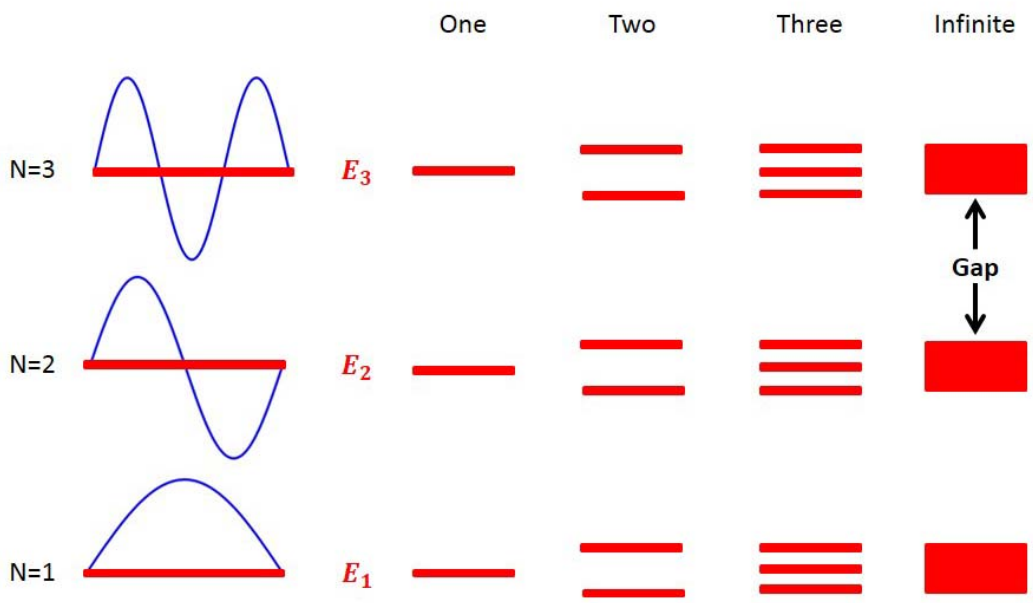

Figure 2.2 Energy Splitting and Separation with Additional Coupled Wells. As more wells are coupled, an equivalent number of states arise which are closer in energy. With numerous wells, the coupled energy states become so close that they are considered to be continuous energy bands. The gaps between bands arise from the original gaps between the individual well states.

For the physical description of electronic band formation, one typically starts with the Kronig-Penney model in solid state physics. The Kronig-Penney model is an exactly solvable model to an infinite periodic series of wells. This construction applies to a string of similar atoms along a one dimensional lattice each sharing electrons and have equidistant spacing between the nuclei. The wavefunction solution for this case has the following form.

$$\psi_n(x) = \begin{cases} Ae^{iK_1 x} + Be^{-iK_1 x}, 0 < x < a \\ Ce^{K_2 x} + De^{-K_2 x}, a < x < b \end{cases} \tag{2.4}$$

In this case n is referring to the well number, not the eigenstate. Since all cells are alike, there is no reason for the wavefunction of a state to have a larger magnitude in one well than any of the others. From this it is sensible to assume the solution is the same in every well, except perhaps an overall phase factor. This phase factor will in general be a function of the well position, but constant within any particular well. Additionally, the phase shift from one well to the next should be equal, as there is no manner to tell any two adjacent wells from another pair. Therefore the phase factor is set to $e^{-ik(a+b)}$, where $a + b$ is the cell position and k is an unknown. This implies the condition $\psi_{n+1} = \psi_n e^{-ik(a+b)}$.

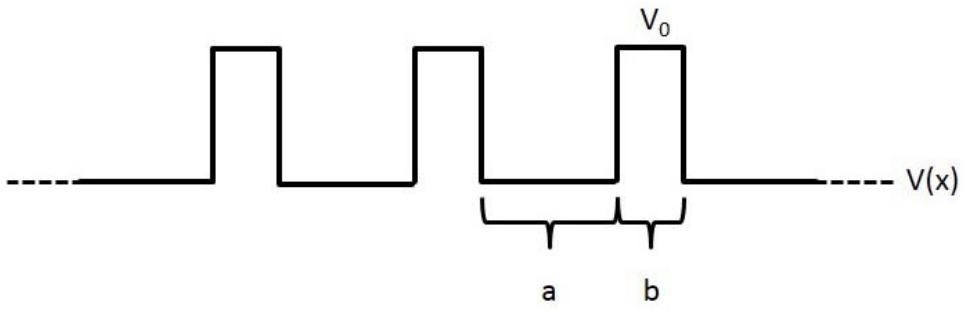

Figure 2.3 Periodic Potential of the Kronig-Penney Model. Diagram showing the potential energy of the Kronig-Penney model. Here a is the lattice spacing, b is the well width, and V_0 is the barrier potential.

After imposing the appropriate continuity boundary conditions and setting the overall amplitude of the equation to one, all the unknown constants can be solved by a determinant equation. With the definitions that $E = \hbar^2 K_1^2 / 2m$ and in the barrier region $V_0 - E = \hbar^2 K_2^2 / 2m$, solving the determinant one is left with the following relation.

$$\frac{\left(K_1^2 - K_2^2\right)}{2K_1^2K_2^2}\sinh\left(K_2b\right)\sin\left(K_1a\right) + \cosh\left(K_2b\right)\cos\left(K_1a\right) = \cos\left(k\left(a+b\right)\right) \qquad (2.5)$$

To simplify matters, consider the barriers to be step function potentials where the potential approaches infinity and the barrier width approaches zero. This is not a bad simplifying assumption considering an atom is mostly empty space where the nucleus (tiny but practically impassable barrier) occupies so little space with the electron's path by far taking the majority of the atomic volume. Applying these conditions to the equation results in the following relation.

$$\frac{K_2^2b}{2K_1^2}\sin\left(K_1a\right) + \cos\left(K_1a\right) = \cos\left(ka\right) \qquad (2.6)$$

For any given *k*, one can solve this equation numerically for the energy. Since the equation depends only on $\cos(ka)$ for *k*, the solutions of $ka = 2\pi n$ will be indistinguishable from the solutions at *ka*. Thus only the solutions for a range of *k* such that *ka* varies by 2π are needed. In other words, for each *k* there are many solutions for the energy.

Figure 2.4 shows an *E* versus *k* diagram for the Kronig-Penney model for *ka* from $-\pi/a$ to π/a. In this diagram two general features stand out. The first is that there are gaps in the energy which occur when the following condition is met.

$$\left|\frac{K_2^2 b}{2K_1^2}\sin\left(K_1 a\right)+\cos\left(K_1 a\right)\right|>1. \qquad (2.7)$$

In other words, for some values of the energy there is no corresponding k value. These gaps appear at values of k that are multiples of π/a. Due to having no solution within these gaps, the particle is forbidden access to such a state. A second feature is that the first derivative of E with respect to k vanishes at these points. The range $-\pi < ka < \pi$ is called the first Brillouin zone of a periodic structure. This is fairly simple for the one dimensional model and gets more complicated moving to three dimensional structures with varying atomic spacings. Despite such complexities, the general features remain consistent among the simplified model to band structure calculations for real periodic materials.

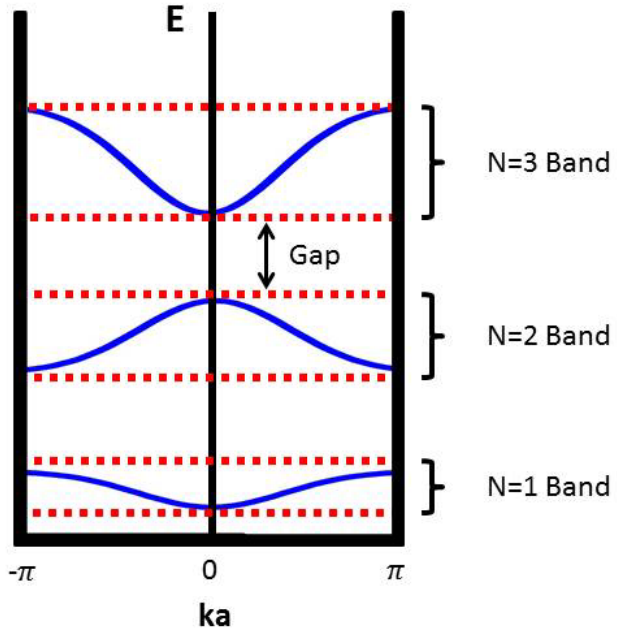

Figure 2.4 First Brillouin Zone of the Kronig-Penney Model. Band diagram showing the first Brillouin zone of the Kronig-Penney model.

2.1.2 Differences between Metal, Semiconductor, and Insulator.

Materials can be placed in one of three broad electrical property classifications consisting of conductors, semiconductors, or insulators, depending on their conductivity at room temperature. The difference between these classifications arises from the magnitude of the bandgap energy, or the energy required moving from the valence band to the conduction band. In molecular terms this is equivalent to moving from the highest occupied molecular orbital (HOMO) to the lowest unoccupied molecular orbital (LUMO). However in crystals, as described previously, the electrons are delocalized over many atoms going from discrete energy states to continuous bands. Due to the electron delocalization, the HOMO energy levels from the atoms form the valence band, and the LUMO energy levels form the conduction band as shown in **Figure 2.6**. The energy difference separating these bands is called the bandgap. As shown in the Kronig-Penney model, since there is no solution for the energy within these gap regions, the electron is forbidden to access such a state. If an electron is excited at an energy above the bandgap, through absorbing thermal or electromagnetic energy, the electron enters an antibonding orbital (conduction band) and freely moves within the solid upon applying an electric field. For a metal, the energy separation between the valence and conduction bands is zero or smaller than the thermal energy (kT = 0.026 eV), and thus conduction ensues readily with applying an electric field. For insulators, the energy gap is large (> 3 eV), such that negligible conduction occurs under standard conditions. Between these two extremes are semiconductors which have energy gaps that are small enough to allow room temperature conduction, but large enough that the magnitude of conduction can be

largely controlled by a host of useful intrinsic and extrinsic factors, such as doping, the presence of a magnetic field, material strain, or incident light.

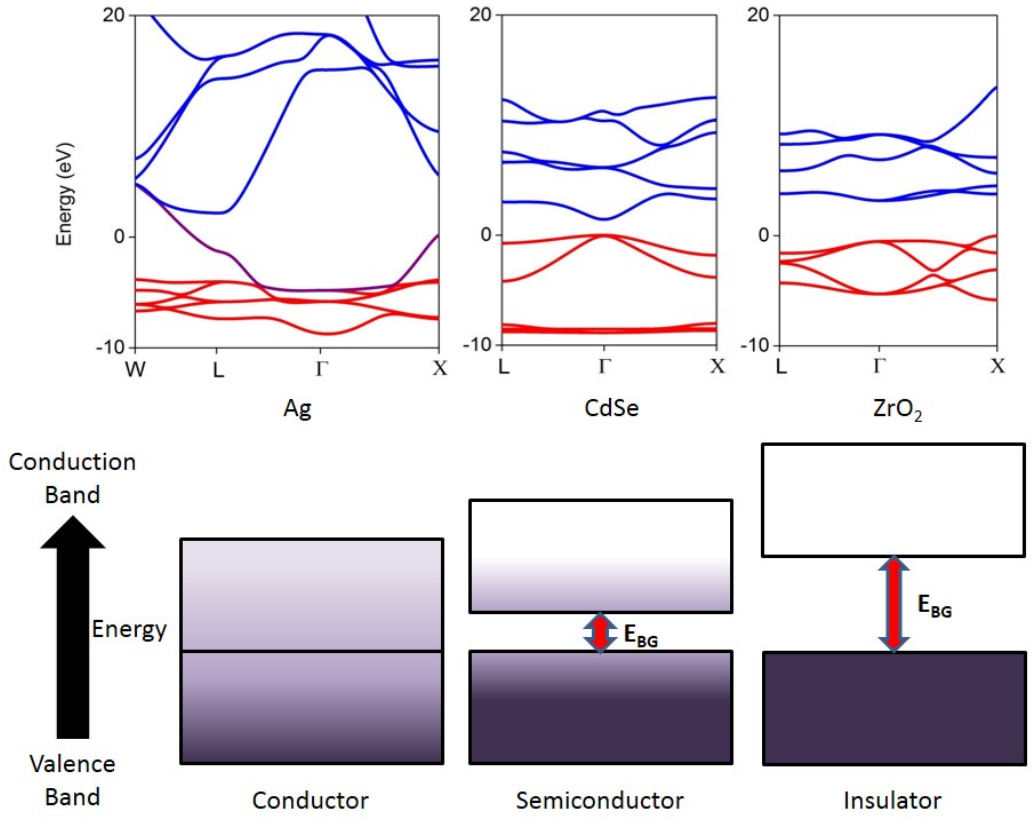

Figure 2.5 Band Structures for a Metal, Semiconductor, and Insulator. The top row shows the calculated band diagrams for silver (conductor), zinc blende CdSe (semiconductor), and cubic zirconia (insulator) using the GGA-PBE method within the code of CASTEP.[65] The red bands are the valence bands whereas the blue bands are the conduction bands. Due to silver being a good conductor, it has a band connecting these regions which is colored in purple. The bottom row shows a simplified band diagram depicting the occupation of the energy levels by electrons denoted by purple shading, and E_{BG} is the energy separation between the valence band maximum and the conduction band minimum.

2.1.3 Electrical and Optical Transitions

Semiconductor materials have adsorption edges which span from the near infrared to the ultraviolet regions of the electromagnetic spectrum. The adsorption edge appears due to optical transitions across the band gap of the material. The physical process where electrons are excited from a lower energy band to a higher one through absorption of a photon is called interband absorption. **Figure 2.7** shows a simplified band diagram for the interband absorption where the electron is excited across the band gap of a semiconductor from the valence band to the conduction band.

From the law of conservation of energy, in the absorption process it can be seen that $E_f = E_i + hv$, where E_i is the initial energy of the electron in the valence band, E_f is the final energy of the electron in the conduction band, and *hv* is the energy of the photon which was absorbed in the transition. As shown earlier, there is a continuous range of energy states within the bands, therefore interband absorption transitions will be allowed throughout a continuous range of frequencies of photons. The range of frequencies that are permitted in the absorption process will be determined by the lower and upper limits of the bands.

As seen from the simplified band diagram in **Figure 2.7**, there is a minimum energy at which adsorption of a photon can happen. In other words, the absorption displays a threshold behavior in that interband transitions are not permitted unless the photon energy exceeds that of the bandgap energy. Allowed absorption transitions hence

provide a continuous spectrum from the low energy threshold at the band gap to an upper value set by the high energy limits of the conduction bands. This is in contrast to that of single atoms where the absorption spectrum comprises of discrete energy lines.

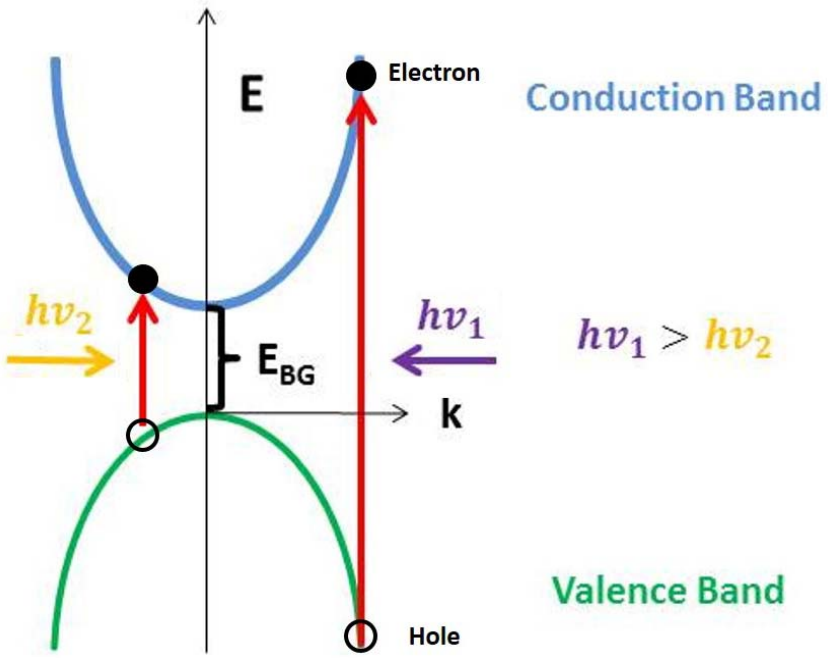

Figure 2.6 The Interband Absorption Process. Once a photon is above the band gap energy threshold of the material, it can be absorbed through the excitation of an electron from the valence band to the conduction band. When the electron is promoted to the conduction band, an unoccupied state is left in the valence band called a hole.

The excitation of the electron leaves the initial state at energy E_i in the lower band unoccupied. This is equivalent to the creation of a hole in the initial band. The interband absorption process therefore creates a hole in the initial state and an electron in the final state. The combination of the excited electron and its concomitant hole is referred to as the electron-hole pair or exciton. An exciton after its creation then has the

ability to radiatively recombine (releasing a photon) in a process called interband luminescence.

Interband luminescence arises in a semiconductor when an electron that has been excited into the conduction band drops back to the valence band via the emission of a photon. This concurrently decreases the number of electrons in the conduction band and holes in the valence band by one. Interband luminescence thus corresponds to the annihilation of an exciton. This process falls into the broader term of fluorescence which applies beyond that of semiconductor exciton recombination. However, the term fluorescence is more often used for light emission of semiconductors and QDs in the literature.

In a typical experiment where one is photoexciting a semiconductor material for fluorescence, one does so using excitation energies greater than the band gap. **Figure 2.7** depicts excitation energies which exceed the band gap which pushes electrons high up in the conduction band. The electrons don't linger in these excited states since they can lose energy swiftly by emitting phonons (quanta of lattice vibrations). The electron losing energy through phonon emission is indicated by the cascade of transitions within the bands shown by curved arrows in the **Figure 2.8**. Each step in the transition relates to a phonon with correct energy and momentum to satisfy conservation laws. The electron-phonon coupling in most solids is very strong and these scattering events take place on time scales as short as a tenth of a picosecond. These events occur much more rapidly than the lifetimes of photon emission (fluorescence) which are in the nanoseconds range,

therefore the electrons (holes) relax to the bottom (top) of the conduction (valence) band long before they radiatively recombine with holes (electrons) in the valence (conduction) band.

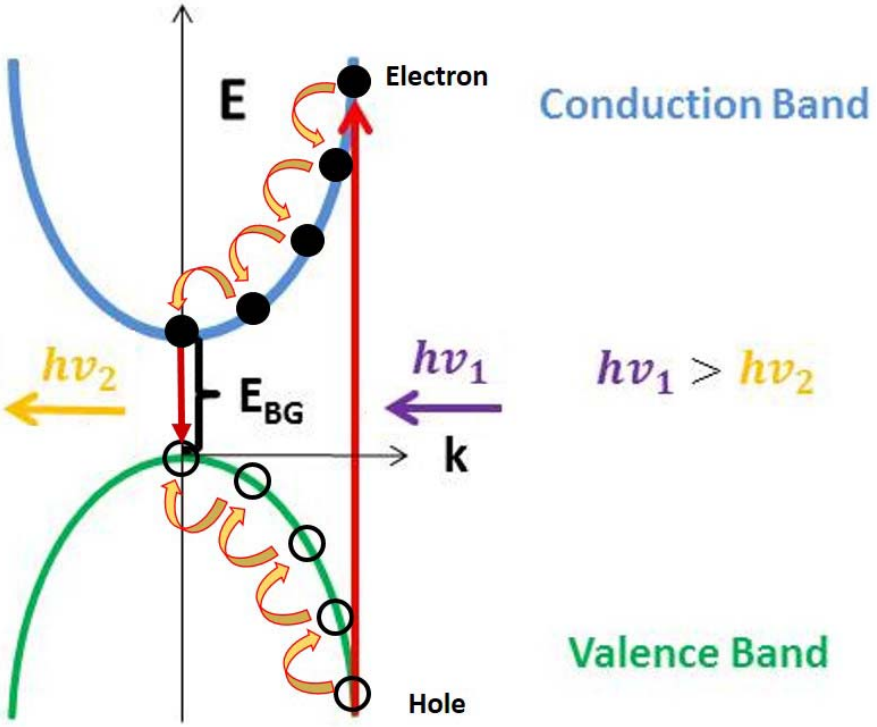

Figure 2.7 The Photoluminescence Process. First light is absorbed at an energy exceeding the band gap of the material. Then the electron and hole relax to the conduction band minimum and valence band maximum through phonon emission respectively. At this point they may radiatively recombine emitting a photon of energy equivalent to the bandgap energy.

Once the electrons and holes have relaxed to the conduction band minimum or the valence band maximum respectively, they must wait at these limits until a photon is emitted or recombine nonradiatively. This leaves enough time to form thermal distributions in the emission spectra (shown as Gaussian peaks instead of delta functions). These distributions will depend on the occupancy factors which are calculated by Fermi Dirac statistics whose treatment is found in most solid state physics books.

2.1.4 Effective Mass

The effective mass of an electron or hole describes the observed mass of the particle in motion within a crystal field. The effective mass can be calculated from the quantum mechanical definition of kinetic energy (E) of a particle of mass m:

$$E = \frac{\hbar^2 k^2}{2m}. \tag{2.8}$$

Since the dispersion relationship between E and k is known from the calculated band structure, one can then calculate the mass of the electron for each value of E and k. The band edges of most semiconductors can be satisfactorily approximated as a parabolic function such that the effective mass is constant:

$$\frac{1}{m^*} = \frac{1}{\hbar^2}\frac{d^2E}{dk^2}. \tag{2.9}$$

Consequently close to the band edges, the electron and hole behave as particles of fixed mass, m_e^* and m_h^*, which are typically written as fractions of the mass of a free electron.

This relation shows the effective mass of a carrier in a semiconductor is inversely proportional to the curvature of the energy band (more curvature lighter masses). This approximation is suitable for describing the properties of semiconductors only when carriers have low kinetic energies, roughly less than half of an electron volt

for II-VI semiconductors. For most semiconductors, the curvature of the valence band is less than the conduction band meaning that the hole is heavier than the electron. As a result, due to electrons having greater mobility than holes, electrons are often preferred as the primary charge carriers in devices. In addition, the wave vector is dependent on the path within the lattice, therefore the effective mass is an anisotropic property which even materials with high crystalline symmetry show anisotropy in charge mobility.

2.1.5 Excitons

Within a semiconductor, the electron and hole generated through excitation are attracted to one another through Coulombic forces. Analogous to a hydrogen atom consisting of a single proton and electron, this pair of particles is called the exciton whose size and binding strength are characteristic of the crystal field in which it is dispersed. The binding energy is determined by the following equation

$$E = \frac{\hbar^2}{2\mu a_B} \ , \tag{2.10}$$

where μ is the reduced mass of the optical electron and hole masses, $\hbar$ is Planks constant divided by 2π, and a_B is the Bohr exciton radius . The exciton size is determined by the Bohr exciton radius, which is described as

$$a_B = \frac{4\pi\hbar^2\varepsilon_0\varepsilon_r}{\mu e^2} . \tag{2.11}$$

Here ε_0 and ε_r are the permittivity of vacuum and relative permittivity of the material respectively, and e is the fundamental unit of charge for the electron. As can be seen from the equations, the exciton binding energy and the size are determined solely by the effective masses of the charge carriers and the dielectric constant of the material. The exciton is smaller and more strongly bound when the effective masses are greater and the crystalline matrix has less ability to screen charges (smaller dielectric constant).

2.1.6 Direct and Indirect Bandgaps

The band gap types of semiconductors generally fall in one of two categories, those that have direct or indirect band gaps. The type which a semiconductor in question falls into can be determined through inspection of the material's band diagram. For direct band gap semiconductors, the conduction band minimum and the valence band maximum both are located at the Brillouin zone center where $k = 0$. Semiconductors which have an indirect band gap, on the other hand, have the conduction band minimum (or valence band maximum) at a location other than $k = 0$. Distinguishing the band gap type difference strikes its importance when one examines the optical properties of the materials. The conservation of momentum dictates that the electron wave vector has minimal change during the adsorption of a photon. Due to this negligible difference in the electron wave vector, the promotion (demotion) of an electron from the valence (conduction) band to the conduction (valence) band through the adsorption (emission) of a photon is indicated by straight arrows. As can be seen from the band diagram for the

indirect band gap material, for an electron to transition from the conduction band minimum to the valence band maximum necessitates a significant change in the electron wave vector values. Thus this process may not proceed through the emission of a photon alone. In fact this transition requires a phonon, or a lattice vibration, which in effect leaves the radiative emission less efficient than a direct band gap semiconductor.

To gain understanding of the conservation of momentum requiring the absorption/emission of photons to have little wave vector changes (straight arrows in band diagrams), one can simply compare the magnitudes of the wave vectors of the electrons and photons. The wave vector for a photon is $k = 2\pi/\lambda$, where λ is the wavelength of light. Photons which have wavelengths in the visible range therefore will have k values on the order of 10^7 m^{-1}. The wave vectors of electrons, though, are much larger. The electron wave vector is related to the size of the Brillouin zone, which is equal to π/a, where a is the unit cell dimension. Since a unit cell length is on the order of angstroms, therefore the electron wave vector on the order of 10^{10} m^{-1}, hence the photon wave vector is much smaller than the size of the Brillouin zone. Consequently the photon momentum is trivial in comparison to the electron momentum and the initial and final wave vectors are practically equivalent ($k_f \sim k_i$). Due to the momentum of the photon being negligible compared to the momentum of the electron, the electron and hole that recombine must have the same k vector akin to that in the adsorption process. The emission will take place near $k = 0$, and hence emit a photon having the energy of the bandgap. Thus no matter what energy excites the electron and holes in the first place, emitted photon energies will be close to that of the bandgap.

Figure 2.8 illustrates the processes that occur during emission in an indirect gap material. The requirement for the emission of both a photon and a phonon for an indirect semiconductor to fluoresce makes the process inefficient. This inefficiency in effect creates a longer radiative lifetime (have to wait for both processes to occur). From the luminescence efficiency (φ) equation

$$\varphi = \frac{1}{1 + \tau_R / \tau_{NR}} , \tag{2.12}$$

where τ_R and τ_{NR} are the radiative and nonradiative event lifetimes, it can be seen that increases in radiative lifetimes will generally result in less luminescence efficiency if nonradiative pathways are kept constant. This decreased luminescence efficiency of indirect band gap semiconductors translates to being poor emitters. Thus their uses in light emitting devices is limited.

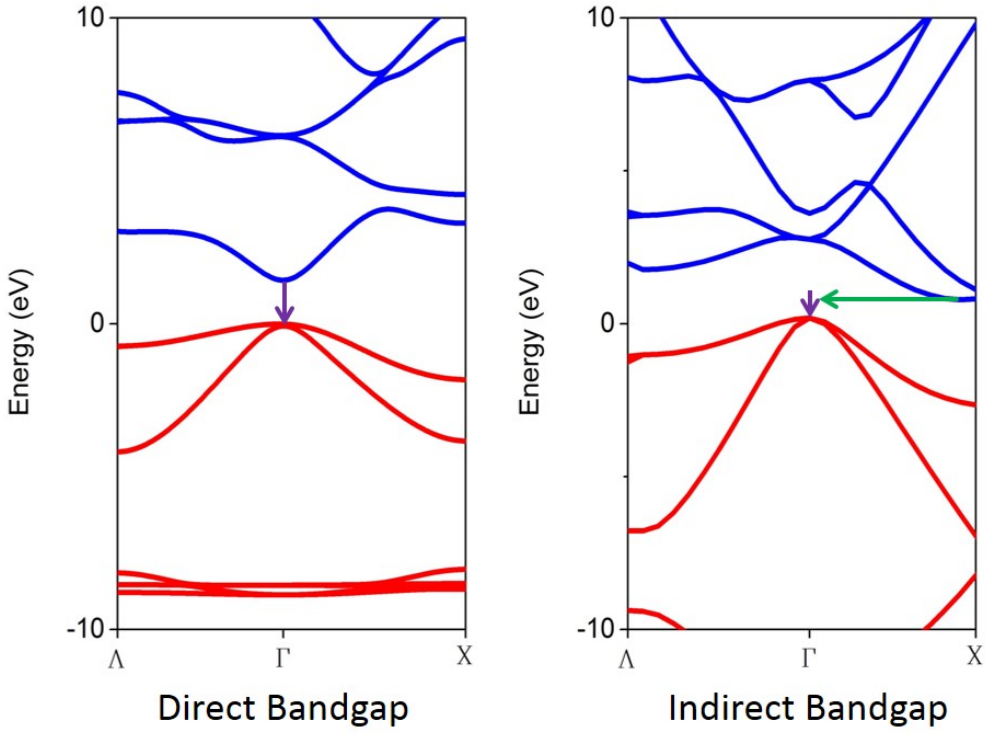

Figure 2.8 Direct and Indirect Band Gap Semiconductors. Band diagrams of a direct band gap semiconductor (CdSe) and an indirect bandgap semiconductor (Si) which were calculated using the GGA-PBE functional in the code of CASTEP.[65] Radiative transitions are indicated by the straight purple arrows, whereas the phonon emission in the indirect bandgap material is indicated by the horizontal green arrow.

2.1.7 Selection Rules in Semiconductor Electronic Transitions

The II-VI semiconductor materials, which most quantum dots studied are composed of, have bonds which are made from two valence electrons of the group II element (2 s electrons) and six of the group VI (2 s and 4 p electrons) element. This leaves each bonded atom with four valence electrons in the solid. Bonding of these electrons is favored and forms solids with crystal structures typically of zinc blende or wurtzite which are closely related to that of diamond. By the groupings of the bonding and antibonding s and p orbitals amongst multiple II-VI pairs leads to the generation of

valence and conduction bands in the solid. From the bonding diagram in **Figure 2.9** one can see that the top of the valence band is a composition of p bonding orbitals, while the bottom of the conduction band is composed of the s antibonding orbitals. Optical transitions in these materials are therefore from p like to s like states which are allowed by the selection rules for dipoles.

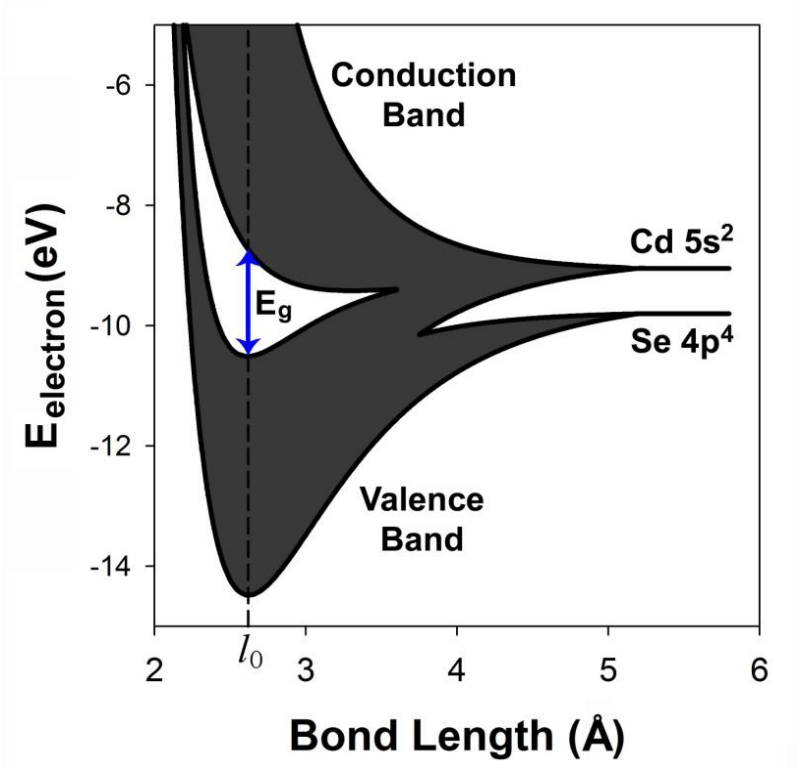

Figure 2.9 Molecular Orbital Bonding Diagram for CdSe. [Image from Smith Thesis 2008] The right side of the diagram represents the valence electron energy levels of individual cadmium 5s and selenium 4p atomic states. Upon bringing the atoms closer together in a lattice (moving left in the diagram), the valence electrons interact, causing the degenerate energy levels of the electrons to split and form energy bands. The material's bandgap energy (E_g) is shown as the energy difference at the equilibrium bond length (l_0).

An illustration of the selection rules for dipole transitions between the valence and conduction bands is as follows: First one starts with Fermi's golden rule which gives

the transition rate between the energy levels of the initial and final states in terms of the matrix element M_{if}.

$$W_{i\to f} = \frac{2\pi}{\hbar}\left|M_{if}\right|^2 \delta\left(E_f - E_i - h\nu\right) \tag{2.13}$$

Adsorbing a photon at the bandgap energy gives the matrix element of

$$M_{if} = \left\langle f \left| e\vec{r} \bullet \vec{E} \right| i \right\rangle \tag{2.14}$$

in Dirac notation. Since $\vec{r}$ is an odd function, the final and initial wavefunctions must have differing parities. In other words, considering an electron in a one electron and one nuclei system and focusing on the angular quantum number l, the change in l must be +1 or -1. The angular momentum rule can be otherwise realized since a photon carries one unit of angular momentum, so the total angular momentum of the atom must change by one unit in the transition for conservation. Thus a transition of a p ($l = 1$) to an s ($l = 0$) state, from the valence to conduction band respectively, satisfy these criteria.

Transitions which adhere to these selection rules are deemed allowed transitions, while those which do not are forbidden. Allowed transitions will have high rates, due to the larger matrix element value, and therefore will have short radiative lifetimes usually in the nanosecond range. The more often used term for these transitions is fluorescence. Alternatively there can be magnetic dipole or electric quadrupole transitions that permit forbidden transitions to occur as opposed to the allowed dipole transitions in

fluorescence. Since these are higher order processes, they have smaller matrix elements and hence have longer radiative lifetimes which are on the order of microseconds or greater. These transitions are more popularly called phosphorescence. Phosphorescence causes delayed emission in which the atoms radiate a considerable time after excitation. This contrasts with fluorescence where emission is rapid in that it radiates in nanoseconds after excitation. Since quantum dots emit through fluorescence, only this process will be further mentioned.

The optical transitions of a typical direct band gap semiconductor are dipole allowed and have large matrix elements as shown previously. This implies that the radiative lifetime for the process will be short on the order of nanoseconds. Indirect band gap materials also have dipole allowed transitions, but due to the band edges not occurring at the same wave vector, the matrix element is smaller and longer fluorescent lifetimes (slower rates) are exhibited compared to direct band gap materials. Longer lifetimes have more susceptibility to nonradiative pathways leading to lower emission efficiencies.

2.1.8 Band Offsets

The relative energy levels of the valence band and conduction band edges between different semiconductors are known as band offsets. These offsets are important parameters for designing heterojunctions between semiconductors for electronic device development in addition to QD luminescence properties which will be

discussed later in the chapter. Values of the offsets are particularly challenging to determine experimentally, varying extensively between experimental techniques and sample preparations, and therefore theoretical approximations have become necessary for reliable numbers. **Figure 2.10** shows the relative band alignments for a variety of widely used semiconductor materials which were calculated from first principles.[66]

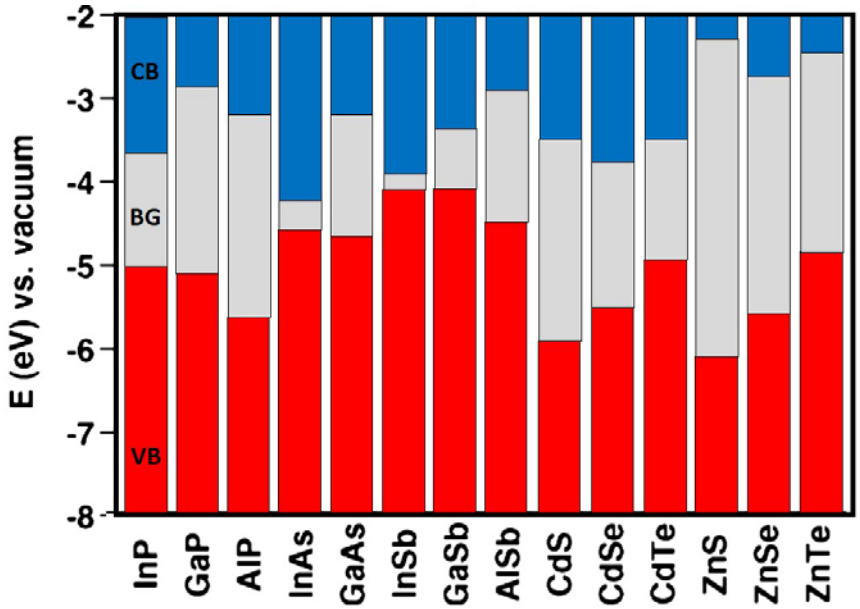

Figure 2.10 Energies of the Band Edges of Various Semiconductor Materials.[67]

2.2 Nanocrystal Physics

The optical properties of solids are not typically found to alter with a change in its size. For example, a red sapphire on the macroscopic level will maintain its red color throughout a gem cutting process. Imagine the astonishment if the gem cutter found that red sapphires turned blue after whittling larger stones to smaller ones for jewelry pieces.

At the nanoscale, however, the color of a material will depend on its size. This is especially true for quantum dots where if a crystallite which gave red fluorescence was lessened in size can change its fluorescent wavelength to blue.

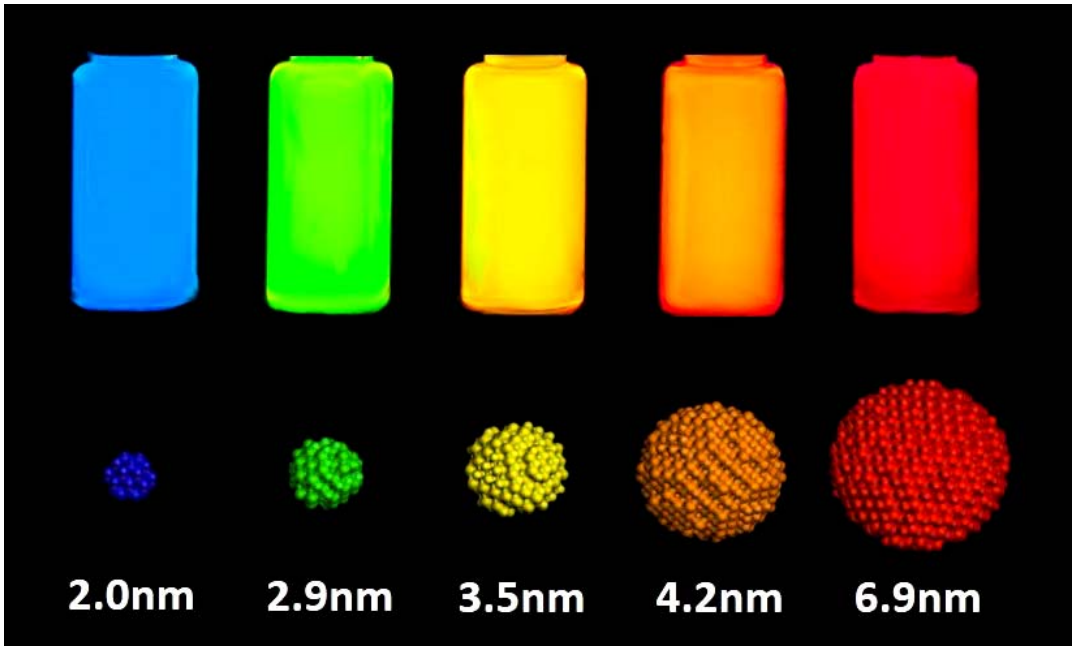

Figure 2.11 Size Series of CdSe QDs. Different color fluorescent emission from CdSe crystals of different sizes. As crystals get smaller, the fluorescent wavelength is shortened.

This size dependence of the optical properties in small sized crystallites is a consequence of the quantum confinement effect.[68] The Heisenberg uncertainty principle states that if a particle is confined to a region of the x axis of length Δx, an introduction to the uncertainty in its momentum will be given by $\Delta p_x \sim h/\Delta x$. Considering a free particle which is not bound by any external potentials and having a mass m, confining the particle along the x axis gives it additional kinetic energy of magnitude $E \sim h^2/m\Delta x^2$. This confinement energy can be observed if it is comparable to or exceeds the kinetic

energy of the thermal motion of the object being inspected. This condition may be written as $E \sim h^2/m\Delta x^2 > k_B T$, which indicates quantum size effects will be important if

$$\Delta x < \sqrt{h^2 / mk_B T} \quad . \tag{2.15}$$

This inequality gives a general idea on the order of magnitude in which the particle's size must be under for quantum confinement effects to be present. Using the electron effective mass for the semiconductor yields the size range on the order of nanometers. Beyond this length scale the confinement effects will seemingly vanish and the material's optical properties will be mirrored to that of its bulk phase.

2.2.1 Brus Model of Quantum Dots

The most apparent indication of quantum confinement in semiconductor nanocrystals is the shift in the optical absorption and emission spectra with size. As described previously, an absorption of a photon having greater energy than the bandgap moves an electron from the valence band to the conduction band, leaving a hole behind in the valence band. The subsequent exciton turns out to be an exceptional applicable example of the particle in a box model in quantum mechanics. The first basic model for the size dependent optical behavior of this system was developed by L. E. Brus.[69,70] The Brus model for quantum dots makes three general approximations of the system: First is that the quantum dots are considered as perfect spheres. Second is that there are no point charges other than the ones associated with the exciton. Lastly, the potential outside of

the nanocrystal is infinite, thus the charge carriers of the exciton are not permitted to move outside the surface of the crystallite.

In composing the model one first starts with a single free point charge within the quantum dot. The Schrodinger equation for this case is

$$\frac{-\hbar^2}{2m}\nabla^2\psi + V(r)\psi = E\psi \quad ; \qquad V(r) = \begin{cases} 0, r < R \\ \infty, r \geq R \end{cases} \tag{2.16}$$

where m is the effective mass of the point charge, R is the radius of the quantum dot, and r is the distance from the center of the nanocrystal. The wavefunction solutions and the corresponding eigenvalue energies to this Schrödinger equation are the following:

$$\psi_n(r) = \frac{\sin\left(\frac{n\pi r}{R}\right)}{\sqrt{2\pi R r}} \tag{2.17}$$

$$E_n = \frac{n^2\pi^2\hbar^2}{2mR^2} \tag{2.18}$$

Equation 2.18 shows the particle in a box behavior seen in the energy changes with absorption/emission with size for QDs. Since the energy and the size are inversely proportional, the absorption/emission energy will increase as the size of the quantum dot decreases. However, formation of an exciton in a quantum dot contains two charges, the

electron and the hole. In the case of an electron–hole pair, the Hamiltonian to be applied to the Schrodinger equation becomes

$$H = -\frac{\hbar^2}{2m_e}\nabla_e^2 - \frac{\hbar^2}{2m_h}\nabla_h^2 + V(\bar{S}_e, \bar{S}_h) \tag{2.19}$$

where $\bar{S}_e$ and $\bar{S}_h$ are the positions of the electron and hole, respectively, within the nanoparticle. The Laplacians having subscripts of e and h mean that they only operate on the electron and hole respectively. The potential energy in this case $V(\bar{S}_e, \bar{S}_h)$ comprises of two parts, the electrostatic and polarization energies, and is still assumed infinite for r > R. For r < R the first part is the electrostatic (Coulomb) attraction between the negatively charged electron and the positively charged hole.

$$V_C(\bar{S}_e, \bar{S}_h) = -\frac{e^2}{4\pi\varepsilon_r\varepsilon_0\left|\bar{S}_e - \bar{S}_h\right|} \tag{2.20}$$

The next element of the potential energy is the polarization energy. Here a point charge inside the particle polarizes the crystal. This polarization affects the energy of the second charge. The polarization potential is given by the following

$$V_P(\bar{S}_e, \bar{S}_h) = \frac{e^2}{2}\sum_{j=1}^{\infty}\alpha_j \frac{S_e^{2j} + S_h^{2j}}{R^{2j+1}} \tag{2.21}$$

where the polarization coefficients are

$$\alpha_j = \frac{(\varepsilon - 1)(\mathrm{j}+1)}{4\pi\varepsilon_r\varepsilon_0(\varepsilon j + j + 1)} \quad ; \quad \varepsilon = \frac{\varepsilon_r}{\varepsilon_{out}} \tag{2.22}$$

and ε_{out} is the dielectric constant of the medium or solvent encapsulating the QD. After combining equations 2.19-2.21, the Hamiltonian for the electron–hole system in a QD is

$$H = -\frac{\hbar^2}{2m_e}\nabla_e^2 - \frac{\hbar^2}{2m_h}\nabla_h^2 - \frac{e^2}{4\pi\varepsilon_r\varepsilon_0\left|\overline{\mathrm{S}}_e - \overline{\mathrm{S}}_h\right|} + \frac{e^2}{2}\sum_{j=1}^{\infty}\alpha_j\frac{S_e^{2j} + S_h^{2j}}{R^{2j+1}} \tag{2.23}$$

From equation 2.23 it can be seen that as *R* approaches infinity, the polarization term $V_P(\overline{\mathrm{S}}_e, \overline{\mathrm{S}}_h)$ goes to zero. At this point the Hamiltonian becomes the hydrogen-like Hamiltonian of the bulk material. In order to evaluate the lowest energy level of the electron-hole system, one is required to determine the coupled wavefunction $\Psi(\overline{\mathrm{S}}_e, \overline{\mathrm{S}}_h)$ for the system. An analytical approximation for the lowest energy solution is achievable here. First the coupled wavefunction is approximated as a function of the lowest energy wavefunctions of the non-interacting electron and hole within the QD, $\psi_1(\overline{\mathrm{S}}_e)$ and $\psi_1(\overline{\mathrm{S}}_h)$ as in equation 2.17. As a first-order approximation we can use the non-interacting wavefunction:

$$\Psi(\overline{\mathrm{S}}_e, \overline{\mathrm{S}}_h) = \psi_1(\overline{\mathrm{S}}_e)\psi_1(\overline{\mathrm{S}}_h) \tag{2.24}$$

Inserting this wavefunction into the Hamiltonian in equation 2.23, and solving the Schrödinger equation, the calculated internal energy of the exciton (QD bandgap) is

$$E_{ex} = \frac{\hbar^2 \pi^2}{2R^2}\left(\frac{1}{m_e} + \frac{1}{m_h}\right) - \frac{1.8e^2}{4\pi\varepsilon_r\varepsilon_0 R} + \frac{e^2}{2}\overline{\sum_{j=1}^{\infty}\alpha_j\left(\frac{S}{R}\right)^{2j}} \tag{2.25}$$

The first term in the equation is the non-interacting particle in the box kinetic energy. The second term is the energy from the Coulombic attraction between the electron and the hole. Here $\left|\overline{\mathrm{S}_e - \mathrm{S}_h}\right| = R/1.8$ is the average distance between the charge carriers. The third term denotes the energy from the polarization. Here as the charge carriers are confined to the same space, the S_e and S_h terms in the polarization potential in equation 2.25 are collapsed into a single position term. The bar over this term denotes the average over the wave function $\Psi\left(\overline{S}\right)$.

$$E_P = \frac{e^2}{2}\overline{\sum_{j=1}^{\infty}\alpha_j\left(\frac{S}{R}\right)^{2j}} = \frac{e^2(\varepsilon-1)}{2\pi R^2\varepsilon_r\varepsilon_0}\int_0^R \sin\left(\frac{\pi r}{R}\right)^2 \sum_{j=1}^{\infty}\frac{j+1}{(\varepsilon+1)j+1}\left(\frac{r}{R}\right)^{2j} dr \tag{2.26}$$

As the polarization energy is small compared to the kinetic and Coulomb energies, not much error is introduced into the total energy by omitting this term. Alternatively, since $(r/R)^{2j}$ rapidly approaches zero as j moves towards infinity, the sum in the polarization energy may be truncated to a few leading terms for a slightly better approximation than completely omitting altogether.

In equation 2.26, the greatest energy term, particularly at small R, is the first term which is the kinetic energy. The form of this energy is merely the addition of the energies of two non-interacting particles (electron and hole) in one box. Thus the size dependence of the first absorption and emission energies of the QD can be associated with the particle in a box model.

The energy needed to create the lowest-energy exciton in a QD is:

$$E_{QD} = E_{BG} + E_{ex} \tag{2.20}$$

where E_{QD} is the transition energy, and E_{BG} is the bulk bandgap energy of the semiconductor material. **Figure 2.12** compares the transition energy calculated using Brus's model with experimental results. Although the theoretical energies match experimental results closely for large sizes of QDs, they differ considerably from experimental values at small sizes. It may be possible to obtain better quantitative agreement by including the shape and crystal structure effects on the band structure, but this would involve too much complexity for a simple analytical expression. However, Brus's model calculates energies that are reasonably close to experimental values for larger QDs and provides an understanding of the behavior of lowest-energy excitons using elementary quantum mechanical principles.

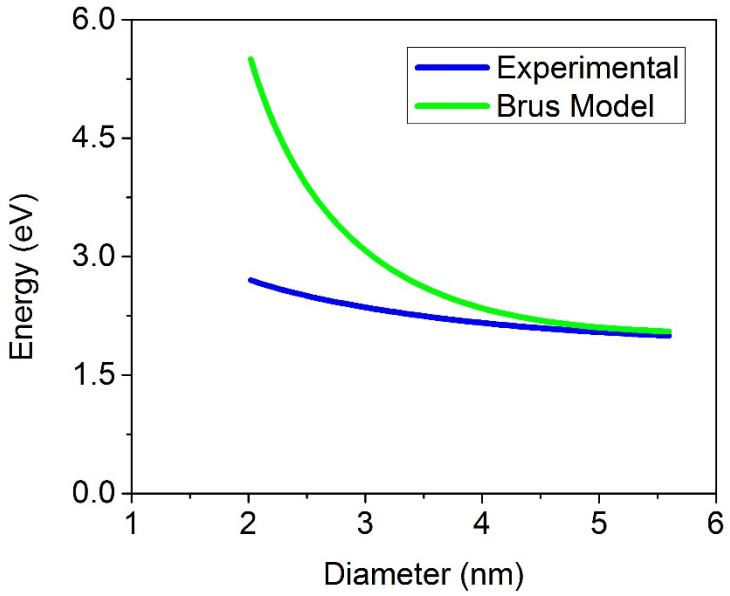

Figure 2.12 Comparison of Adsorption Energies of CdSe QDs Obtained Through the Brus Model and Experiment. Comparison of the experimental and calculated transition energies in CdSe QDs. Note that at small crystal sizes the Brus model diverges rapidly from experimentally observed values.

2.2.2 Electronic Structure of Quantum Dots

To understand the size-dependent electronic structure of quantum dots one can go back to the description of atomic and molecular orbitals provided earlier in the chapter. The bulk semiconductor material is characterized by a bandgap between a continuum of energy states known as the valence band and conduction band. The molecular orbitals in the valence band are the bonding p orbitals for the II-VI semiconductors. Each contains a pair of valence electrons forming a covalent bond. Therefore this band is filled with electrons. The conduction band, however, consists of unoccupied antibonding s orbitals. In both bands, the orbitals are concentrated within the center, thinning out towards the edges as shown in **Figure 2.13**.

When shrinking the crystal size of a semiconductor material by progressively removing atoms from its surface, the atomic orbital contributions to both energy bands are removed as well. Once the crystal has been diminished to a size comparable to the Bohr radius, two phenomena happen. First, the bands lose their continuity of energy states and individual orbitals are shown. Next, orbital removal occurs from the band edges, where the orbital population was scarce to begin with, which leads to widening the bandgap. Additional elimination of atoms from the crystal leads to enhancement of quantization of the energy levels from bands along with increases in the bandgap. Thus quantum dots have an energy structure in between that of the bulk material and a molecule.

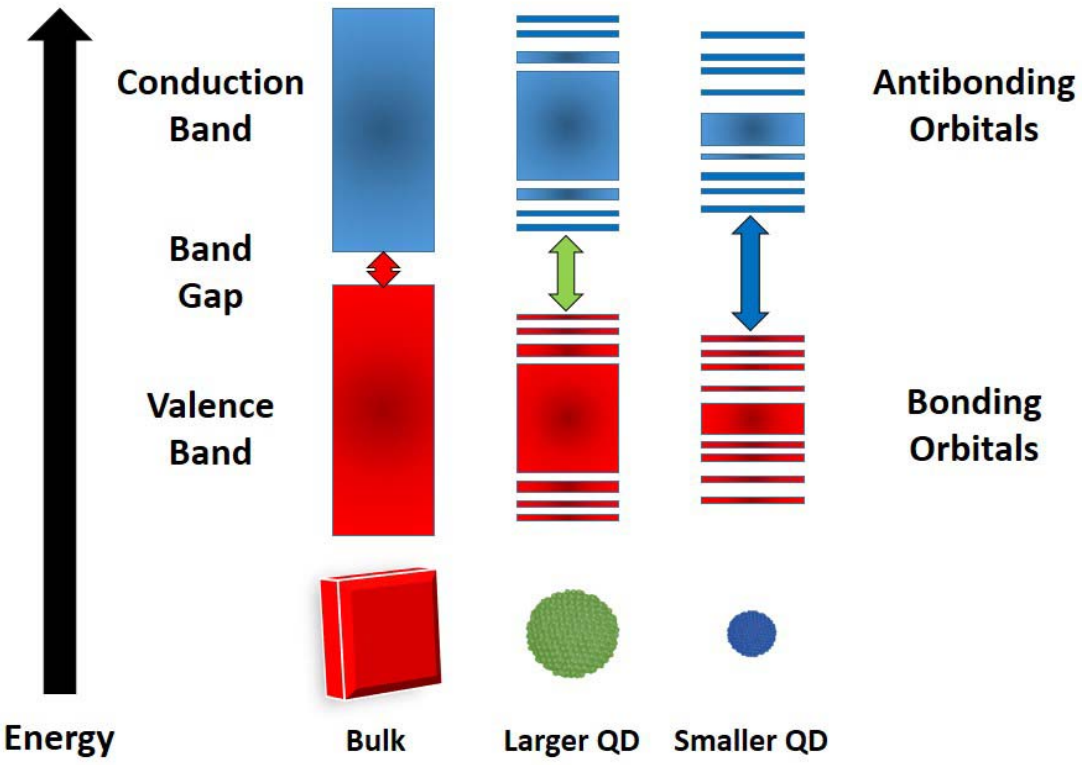

Figure 2.13 Energy Structure Changes of QDs Compared to its Bulk Phase. Evolution of the energy structure moving from the bulk phase to smaller quantum dot particles.

2.3 Chemical Synthesis of Quantum Dots

Semiconductor quantum dots (QDs) have been synthesized through an assortment of physical and chemical methods. Means of physical methods for producing QDs include molecular beam epitaxy and metal organic chemical vapor deposition approaches.[71,72] Chemical routes typically consist of particle growth in glasses,[73,74] or colloidal synthesis methods.[63,75] Since the particles involved in this thesis are all colloidal, the emphasis of the synthesis methods will be focused on this area. Colloidal QDs contain an inorganic semiconductor core which is encompassed by a layer of organic ligands. This

organic layer affords electronic and chemical passivation of surface dangling bonds, thwarts uncontrolled growth and aggregation of the particles, and permits QDs to be chemically modified with its solubility and reactivity influenced by the character of the surface ligands. This section focuses on effective synthesis methods determined by high crystallinity, suitable surface passivation, solubility in nonpolar or polar solvents, and maintaining size monodispersity.

2.3.1 Nucleation and Growth

A majority of preparations that yield high quality and monodisperse QDs involve pyrolysis of metal-organic precursors at high temperatures in coordinating solvents. Originally understood in terms of LaMer and Dinegar's studies of colloidal nucleation and growth,[76] these synthesis routes involve a temporally discrete nucleation period followed by a relatively quick growth period from solution-phase monomers and finally slower growth by Ostwald ripening when the monomers are depleted. Nucleation is attained by rapid injection of a precursor into hot coordinating solvents, causing thermal decomposition of the reagents creating a supersaturation of monomers that is depleted in part through particle generation. Growth subsequently ensues by transfer of monomer from solution to the QD nuclei. Monomer concentrations are below the critical concentration for nucleation during the growth phase, thus these species only add to existing particles rather than form new nuclei.[77] Once monomer concentrations are depleted, growth can further progress through Ostwald ripening. Ostwald ripening is where growth of larger particles proceeds through sacrificial

dissolution of smaller particles leaving fewer particles in the system.[77] More precise descriptions than traditional LaMer and Dinegar growth of the molecular level mechanism of precursor evolution in nanoparticle growth have been shown for II-VI[78] and IV-VI[79] QDs. It has also been suggested that the traditional model is not valid for hot injection synthesis methods due to nucleation, growth, and Ostwald ripening could occur almost simultaneously. Furthermore, the presence of strongly coordinating ligands can modify nucleation and growth stages which confound the simple construal of reaction events.[80] A modification of the Ostwald ripening process has also been observed in certain QD syntheses wherein the particle concentration decreases substantially during the growth process due to rapid dissolution of smaller particles which aids in narrowing the size distribution for the larger ones. This process has been termed self-focusing[81-83] which is quite different than the expected size distribution widening of typical Ostwald ripening.

Alternatively, supersaturation and nucleation can be activated by slowly heating up the reaction mixture. In this case reagents are mixed at low temperatures and gradually brought to a temperature at which precursor reaction and decomposition occur quickly enough to result in supersaturation.[84] Supersaturation is again relieved by particle nucleation (as in the hot injection method), after which the temperature is controlled to avoid further nucleation events by allowing monomer addition to existing nuclei to occur more rapidly than new monomer formation. Thus QD synthesis does not necessitate an instantaneous nucleation event, but in most cases it is necessary for narrow size dispersions.[77]

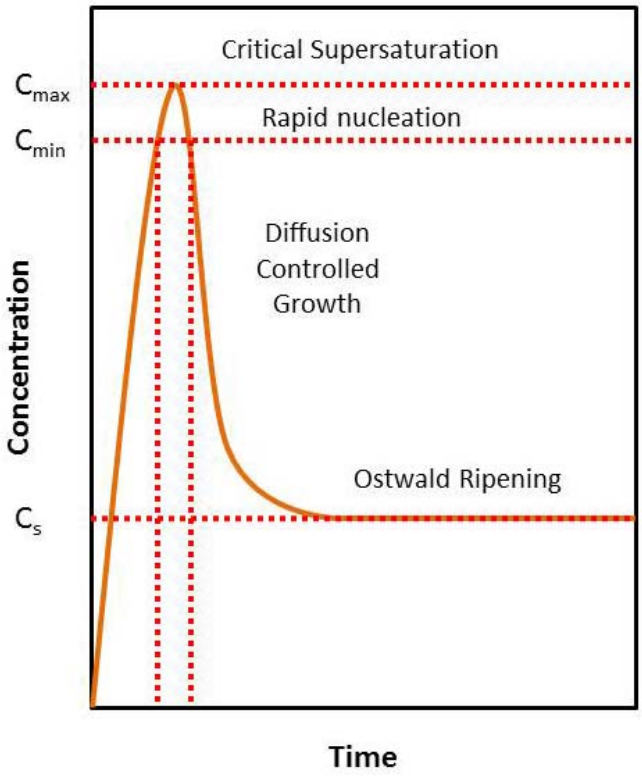

Figure 2.14 LaMer Model Diagram of Crystal Nucleation and Growth. Plot of the LaMer model[76] for the generation and growth of nanocrystals. C_{max} is the maximum supersaturation of the monomers in solution, C_{min} is the minimum concentration of monomers for nucleation of particles, and C_s is the solubility concentration of the monomers in solution.

2.3.2 Controlling Particle Size and Monodispersity

A QD sample's size and size dispersion can be manipulated during the growth phase of the reaction, as well as after initial core synthesis. In general, nucleation and growth temperatures display opposing characteristics. Lower nucleation temperatures provide lower monomer concentrations yielding fewer larger sized nuclei, whereas higher

growth temperatures will develop larger particles due to the rate of monomer addition to existing particles is increased. Also, higher temperatures facilitate Ostwald ripening. The reagent concentration can impact both the nucleation and the growth process, and its effect is reliant on the ligand/reagent concentration ratios and the binding strength of the ligands to the monomer species. Higher reagent concentrations lead to the formation of fewer larger nuclei and subsequently larger particles with all else being equal. Likewise, low ligand/reagent ratios produce larger particles. Weak binding ligands promote the growth of larger particles, but if the binding is too weak, agglomeration of particles into insoluble aggregates will result.[77] Ligand monomer interactions can affect growth processes, as well. Ligands which have strong binding to the monomer species may prevent high monomer concentrations that are necessary for fast growth,[85] or they may support reductive elimination of the metal species.[86]

The steric bulk of the coordinating ligands can influence the rate of growth following nucleation. For instance, bulky surfactants with relatively high steric hindrance to approaching monomers will decrease growth rates by lessening diffusion rates to the particle surface.[77] Ligands used in QD syntheses typically consist of alkylphosphines, alkylphosphine oxides, alkylphosphates, alkylphosphites, alkylphosphonic acids, alkylamines, alkylthiols, and fatty acids of various alkyl chain lengths and degrees of branching. **Figure 2.15** shows the structure of some of these ligands commonly used in the synthesis of semiconductor nanocrystals. These ligands coordinate by the polar head group to the surface of the QD while the hydrophobic tail is out in the solvent. This interaction allows solubility in commonly used nonpolar solvents

and deters aggregation by shielding the attractive van der Waals forces between QD cores. The interaction of the ligands and monomers to the QD surface is dynamic and can adsorp or desorp to or from the crystallite surface. The ability of constituents to reversibly attach and detach to and from the QD surface allows crystallite annealing while avoiding aggregation which is an essential condition for attaining highly crystalline particles.

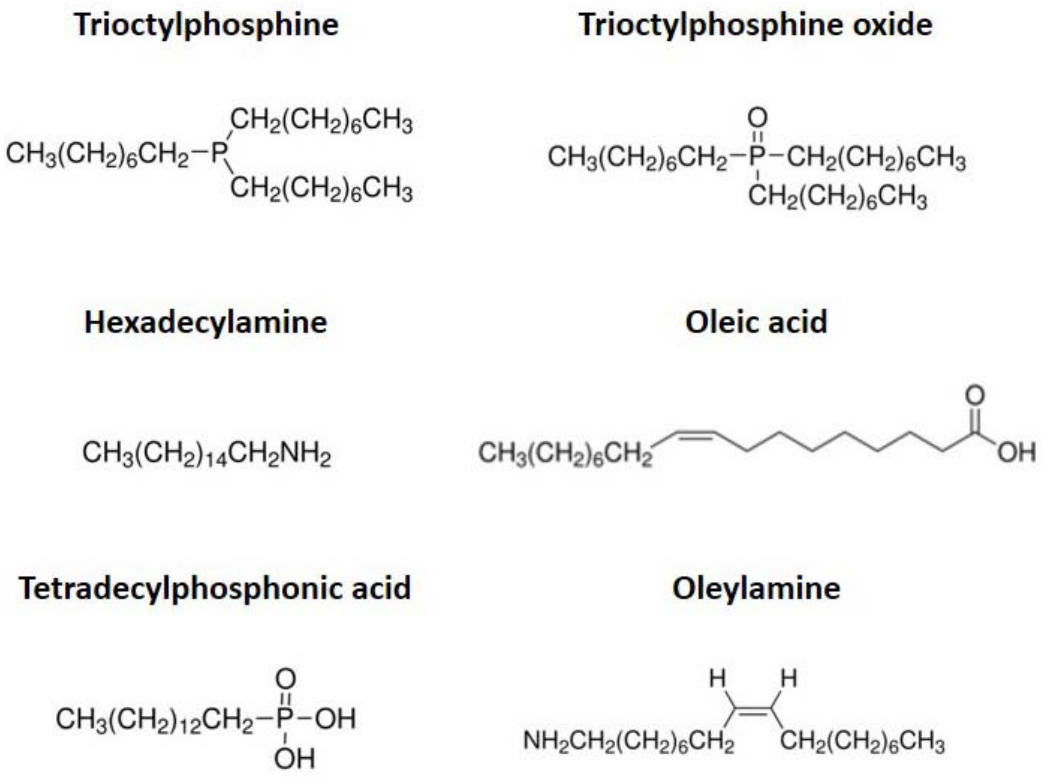

Figure 2.15 Common Ligands Employed in Quantum Dot Synthesis.

The two phases of growth, the rapid first phase and Ostwald ripening, vary in their influence on QD size dispersity. During the first stage of growth, size distributions

remain fairly narrow and can even become more focused than the initial nuclei distribution, whereas with Ostwald ripening the distribution tends to defocus as smaller particles begin shrinking by losing monomers to the growth of the larger particles.[87] The benchmark synthesis for CdS, CdSe, and CdTe QDs,[63] which greatly enhanced the total quality of the nanoparticles generated until that point, relied on Ostwald ripening to obtain a size series of II-VI QDs. Size dispersions of 10–15 % were obtained for the larger sized particles which was later narrowed by size selective precipitation. This iterative and labor intensive process separates larger from smaller QDs and can generate dispersions of ≤ 5 %.

Synthesis routes for II-VI QDs have also been established that avoid the Ostwald ripening growth phase. These methods preserve the phase of relatively fast growth by adding additional monomers to the reaction solution after nucleation, thereby preventing monomer depletion and Ostwald growth. The additional monomers introduced into the growth phase are added at a rate to keep growth of existing particles, but not so much as to surpass the nucleation threshold for new particles. The distribution of particles narrow as monomer preferentially adds to smaller particles with a higher surface energy rather than to larger ones.[87] On the other hand, growth can be stopped during the fast-growth stage, by removing the heat source and rapidly cooling the mixture, keeping size distributions which are relatively close to the initial nuclei. Since nucleation size can be manipulated by changing precursor concentration or reaction injection temperature, a range of sizes (though smaller than monomer addition focusing due to limited time in the growth phase) with narrow distributions may be obtained.

2.3.3 CdSe the Classical Example of QD Systems

Of the various materials of which QDs are composed of, CdSe is deemed a "model" system due to the ease of its production and has been the focus of the abundant elementary research into the electronic and optical properties of QDs. High quality CdSe QDs can be consistently synthesized from pyrolysis of an assortment of cadmium precursors, including dimethylcadmium[63] and several cadmium salts (e.g., CdO and $Cd(CH_3CO_2)_2$),[88] combined with a selenium precursor of Se powder dissolved in trioctylphosphine (TOP) or tributylphosphine (TBP). The first high quality CdSe particle synthesis methods contained the combination of technical grade trioctylphosphine oxide (TOPO) and TOP, where the TOPO performance was batch specific due to the rather arbitrary existence of adventitious impurities.[63] Later researchers discovered the adventitious impurities were phosphonic acids, which were then combined with pure TOPO to mimic the synthesis outcomes with "good" batches of the tech grade TOPO.[89] The phosphonic acid precursor can be substituted with various fatty acids to coordinate cadmium, such as palmitic and oleic acid, where shorter alkyl chain lengths produce quicker particle growth. Fatty acids are generally well suited for the growth of larger QDs, compared to using phosphonic acids, as growth proceeds more quickly.[88] For example, the cadmium precursor is usually dissolved in the fatty acid at modest temperatures, converting the Cd compound into a cadmium carboxylate. Alkyl amines are also useful in the CdSe growth media as they increase the activity of the fatty acids while coordinating to the particle surface.[88] Ligands which are poorly suited

for CdSe synthesis include those that have the anion of a strong acid and thiol-based systems.[88] If ligands bind too strongly to cadmium cations, the nucleation of particles will be inhibited. One of the most effective synthesis methods of CdSe QDs, in terms of resulting quantum yields (QYs) and monodispersity, uses a combination of multiple different ligands including stearic acid, TOPO, hexadecylamine (HDA), TBP, and dioctylamine (DOA).[90]

2.3.4 Optimizing Nanocrystal Core Quantum Yields

QDs which exhibit high QYs tend to have a well passivized surface. The QY of a sample can diminish as a result of many "dangling" bonds at the particle surface which act as traps for charge carriers. Recombination of trapped carriers leads to a distinctive deep trap emission band on the higher wavelength (low energy) side of the band edge photoluminescence (PL) peak. Band edge emission is linked with recombination of carriers in the interior quantized states. Coordinating ligands help passivate the dangling bonds of the surface which enhances the relative intensity of band edge PL to the deep trap emission. Using a combination of passivating ligands in the reaction mixture for CdSe particles has been able to generate QDs having QYs as high as 85 %.[90] These unusually high QYs are equivalent to some of the greatest accomplished by passivation through growth of an inorganic epitaxial layer. Such high luminescent efficiencies are attributed to the presence of primary amine ligands, as well as to the usage of excess selenium in the reaction mixture (Cd:Se of 1:10). Higher selenium to cadmium ratios alone increase the quantum yields compared to an equimolar reaction mixture (40 – 50 % compared to 5 –

15 %) which is likely due to the differences in reactivity of the precursors. Through knowledge of the relative precursor reactivities, improved crystalline growth and enhanced PL QYs can be achieved by accordingly adjusting the reagent ratios.[90] Moreover, to attain high QYs, reactions should be limited to time spans not much beyond 30 min. PL efficiencies tend to rise, reach a maximum, then decline as growth progresses.. QD samples that are extracted at the QY maximum, otherwise known as the "bright point", tend to have emission color of orange-red (~ 600 nm). However, through controlling precursor type, concentration ratios, solvent type, the nucleation and growth temperatures, and the growth period, high QY QDs emitting with > 30 % efficiency from colors of green to the far red can be routinely prepared.[90] Lastly, the vital effect of the primary amine ligands may result from their ability to pack more efficiently on the QD surfaces compared to trialkylphosphines such as TOP or TOPO.[91] Unfortunately though, the amine CdSe QD binding is not as stable as other more strongly binding ligands.[92] Therefore, growth solutions prepared using primary amines are highly luminescent at first, but purification and washing of the sample can dramatically reduce the QY back to comparable levels of samples synthesized with more strongly binding agents.

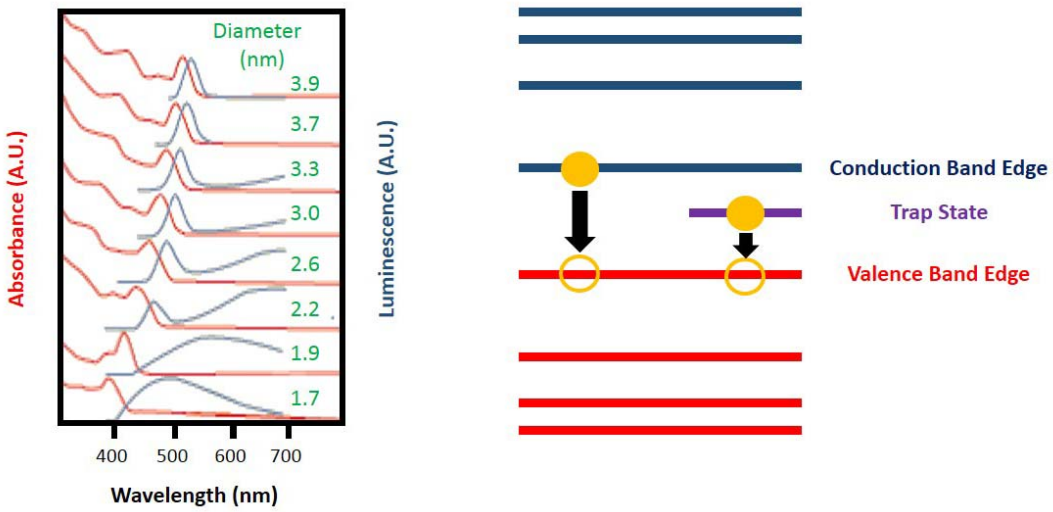

Figure 2.16 Band Edge Absorption and Emission of Band Edge and Deep Trap Emission from a Size Series of CdSe QDs. Absorption and emission spectra from a size series of CdSe quantum dots of the band edge and deep trap emission.[93] Since smaller crystal have more surface to volume, more dangling bonds are present (harder to passivate through organic ligands) which present intermediate energy states between the band edges. Emission of these states show as long tails extending to the red end of the spectrum.

2.3.5 Core/Shell Quantum Dots

Encompassing CdSe QD cores with epitaxial layers of either ZnS,[94,95] ZnSe,[96] or CdS[92] has become a standard technique in QD synthesis and normally delivers nearly an order of magnitude enhancement in QY compared to the solely organic capped starting QD cores. Recently synthesis methods of inorganic shell growth have yielded nanocrystals with QY approaching unity.[97-99] The heightened QY from inorganic shell layers is attributed to passifying dangling bonds on the nanocrystal core surface as well as from increased confinement of electrons and holes to the particle core, thereby preventing a carrier surface trap interaction. The latter effect comes about when the conduction and valence band offset of the shell material is higher and lower respectively than that of the core material, as is

the case for CdSe/ZnS , CdSe/ZnSe, and CdSe/CdS core/shell particles. The luminescence spectra of the QD sample can indicate whether effective passivation of surface traps has been accomplished. In poorly passivated QDs, deep trap emission shows as a broad tail in the higher wavelength region of the narrower band edge PL peak. The broad deep trap emission will vanish following successful shell growth while the band edge PL peak increases in intensity.

Several measures of producing type-I core/shell QDs share many synthetic characteristics. First, optimal outcomes are attained if initial particle size distributions are narrow, as some size-distribution broadening may transpire during shell growth. Much information about the shell growth process can be monitored by continually sampling the reaction mixture and observing its adsorption spectra. If the band offsets between the core and the shell materials is sufficiently larger than the confinement energy of the respective carriers, then substantial red-shifting of the absorption band edge should not occur, as the carrier wavefunctions remain limited to the core. Substantial redshifts observed during the growth of large offset shells indicates growth of the cores during shell preparation, most likely as a result of Ostwald ripening in the early stages of shell growth. A minor broadening of absorption features is normal and results from slight broadening of the particle size dispersion. Alloying of the shell elements into the core would also be apparent in the absorption spectra. In this case the band edge would shift to some intermediate energy between the band energies of the core and shell (a blue shift for type I).

During the shell growth, there is a competition among heterogeneous (material is deposited on the existing QD cores) and homogeneous (material nucleates into new additional particles) nucleation of the shell material. Through using comparatively low precursor concentrations and reaction temperatures new particle formation can be avoided. Low precursor concentrations prevent reaching supersaturation required for the homogeneous nucleation threshold and therefore promotes shell growth by heterogeneous nucleation. For example, diethylzinc and bis-(trimethylsilyl) sulfide for ZnS shell growth are added drop-wise to avert accumulation and supersaturation of unreacted monomers in the growth solution. Additionally, moderately low reaction temperatures avoids Ostwald ripening growth of the starting core particles.[92,95] ZnS can grow as a crystalline shell at temperatures as low as 140°C,[95] and CdS shells have been effectively synthesized at 100°C,[92] which are more than sufficiently low enough to prevent homogeneous nucleation and Ostwald ripening. An additional option for avoiding homogeneous nucleation of the shell material is to include organic ligands which have a relatively high affinity for the shell metal. Introducing a strong binding agent to the growth solution tends to result in more controlled shell growth. For example, more controlled growth of CdSe on InAs cores is achieved if TOPO is replaced with TOP, where TOP (softer Lewis base) coordinates with higher affinity than TOPO (harder Lewis base) with cadmium (softer Lewis acid).[100]

Successful deposition of epitaxial layers in QD systems is even possible where large lattice mismatches exist between core and shell. The most frequently studied core/shell system of CdSe/ZnS can be successfully synthesized despite a rather large

(12%) lattice mismatch. Such large lattice mismatches cannot be endured in bulk flat systems where strain induced defects would dominate at the heterojunction. It is likely that the highly curved surface and reduced facet lengths of nanocrystals relax the structural requirements for epitaxy. Two types of epitaxial growth manifest in the large lattice mismatched CdSe/ZnS QD system: coherent (strain tolerated) for 1-2 monolayers of ZnS, and incoherent (dislocation formation) for greater than 2 monolayers.[95] With multiple layers of high lattice mismatched material, the strain can no longer be sustained without the formation of dislocations. These dislocation defects within the core/shell boundary create nonradiative recombination sites which lead to diminished QYs compared to coherently epitaxial thinner shells or using a more lattice matched shell material as can be seen in **Figure 2.17** below.

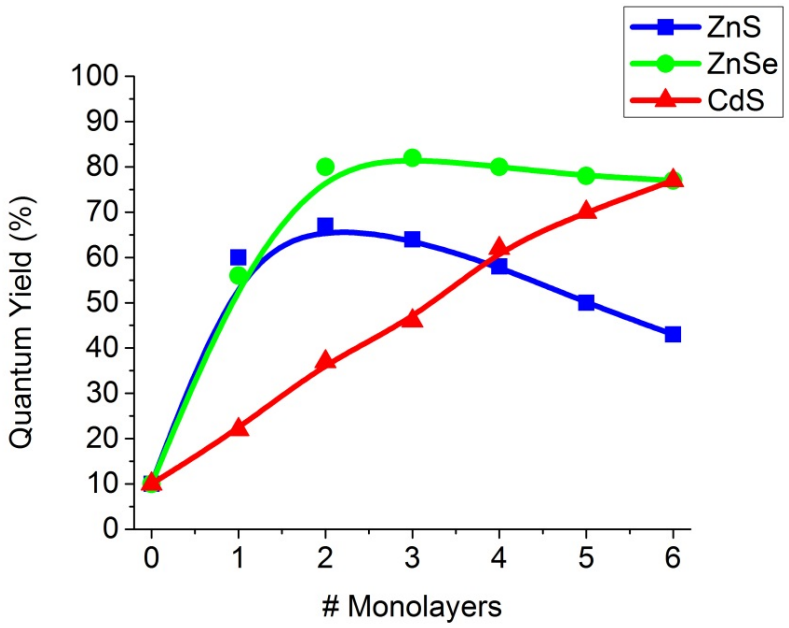

Figure 2.17 Changes in Quantum Yield for CdSe Cores with Varying Monolayer Thickness of Wider Band Gap Shells. Plot of the quantum yield with additional monolayers of shell material around 2.6 nm CdSe cores.

Exact lattice matching between the core and the shell can be achieved through the precise chemistry of the shell precursors. An example of lattice matching is using a zinc-cadmium alloy which successfully produced (InP)ZnCdSe nanoparticles having virtually no lattice mismatch amongst the core and the shell.[101] High resolution TEM verified the epitaxial relationship between the layers, and coherent growth was observed with shell thicknesses reaching 5 nm. The alloyed shell layer effectively protected the InP QDs from oxidation, of which InP is more susceptible compared to other common QD core materials.

Core/shell growth methods have been further advanced to permit more precise control over the number of monolayer additions. A procedure established initially for the deposition of thin films onto solid substrates, successive ion layer adsorption and reaction (SILAR), has been adapted for QD shell growth.[102] Through this method, homogenous nucleation of shell materials is averted and elevated shell growth temperatures can be endured due to the cationic and anionic shell precursors not coexisting in the growth solution. Each subsequent layer of ions is introduced only after the previous layer has been completely deposited on the QD core. This technique has allowed deposition of thick shells, comprising of several shell monolayers, without loss of the sample's size monodispersity and exhibiting great crystallinity. Initially demonstrated for CdSe/CdS QDs with shells up to five monolayers thick,[102] the tactic also has been applied to multishell step-alloyed structures,[44,103] as well as to "giant" shell systems exceeding ten monolayers..[44] The multishell step-alloyed structure of CdS/$Zn_{0.5}Cd_{0.5}$S/ZnS on CdSe cores provides the ability of tuning the lattice parameters and the band offsets in the

radial direction. The resultant particles are highly crystalline, uniform in shape, and electronically well passivated.[103]

2.3.6 Type I and Type II Quantum Dots

Type-I core/shell NQDs discussed previously have a shell material of a larger band gap than the core. Also, the conduction and the valence band edges of the core are located within the energy gap of the shell. In this case the electron and hole experience a confinement potential that will localize both of the carriers within the core, thereby reducing their interactions with surface trap sites which results in increased QYs. Instead, core/shell structures can be tailored such that the lowest energy states for the electron are in the shell and hole in the core or vice versa. The energy gradient present at the heterojunction will spatially separate electrons and holes between the core and the shell. This spatially indirect energy gap is set by the band offsets in the conduction band edge of one semiconductor and the valence band edge of the other semiconductor. These structures that exhibit this spatially indirect band gap are referred to as type-II QDs. Synthesis of type-II QDs include arrangements of materials such as CdTe/CdSe,[104,105] CdSe/ZnTe,[104] CdTe/CdS,[106] ZnSe/CdSe,[107] and CdS/ZnSe.[108] The ZnSe/CdSe QDs are more accurately labeled quasi-type-II particles, as they only deliver partial spatial separation between electrons and holes. Quasi type-II structures can also be generated from a type-I alignment with multiple monolayers shell addition of a material where one of the band offsets has a low energy barrier. This situation can

arise slightly in CdSe/ZnSe but much more profoundly in CdSe/CdS QDs as shown in **Figure 2.19**.

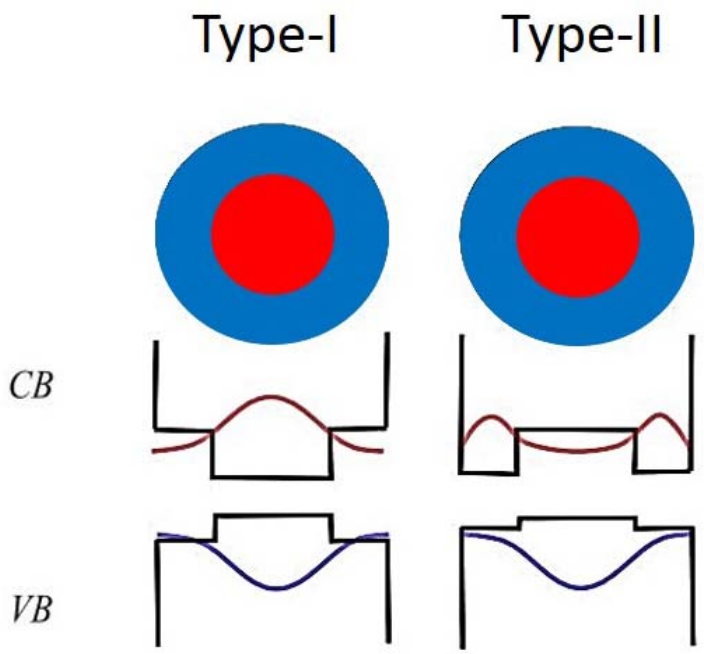

Figure 2.18 Band Alignment of Type-I and Type-II QDs. Diagram illustrating the difference between type-I and type-II core/shell quantum dots. In type-I, the offsets are arranged so that that there is high overlap between the electron and hole wavefunctions within the core. In type-II however, the offsets are arranged so that the carriers are mainly located in different regions of the structure having less spatial overlap.

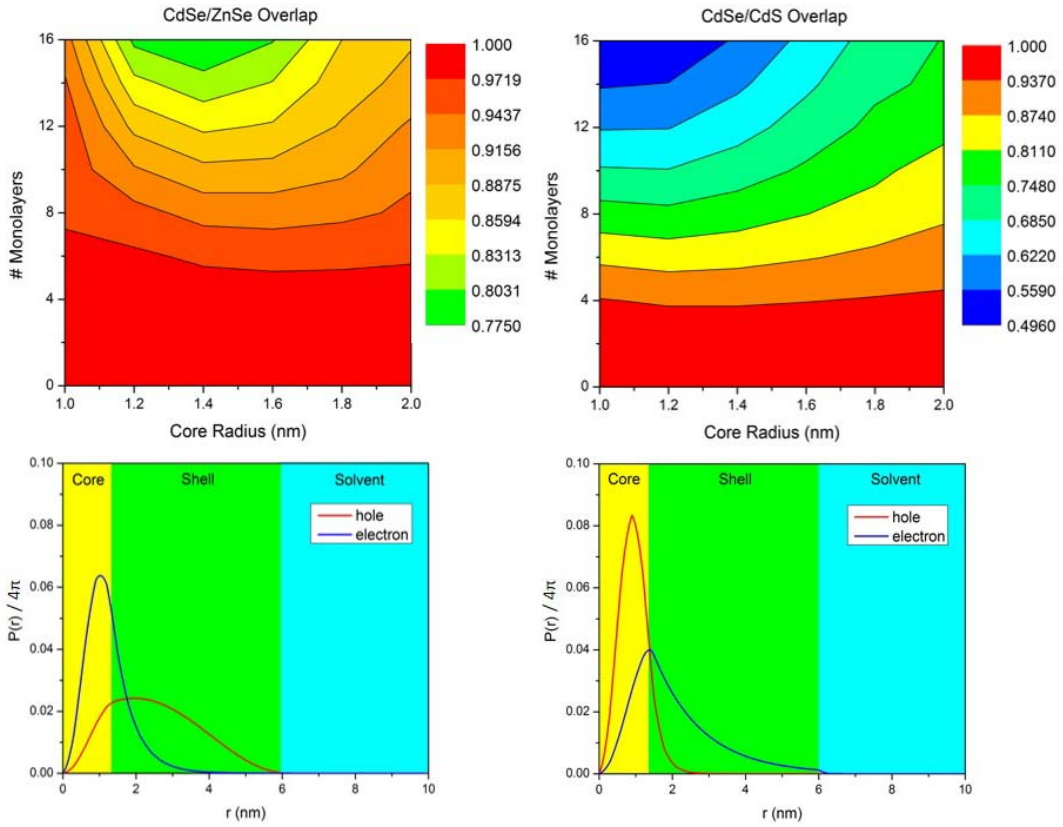

Figure 2.19 Overlap between the Electron and Hole Wavefunctions in CdSe/ZnSe and CdSe/CdS core/shell QDs. Contour plots of the overlap integral values of the carrier wavefunctions (above) and plot showing the probability of the carrier wavefunctions (below) in the radial direction of a CdSe core of 1.4 nm radius and 16 monolayers of ZnSe and CdS. As one of the carriers is able to delocalize throughout the nanocrystal volume while the other is confined to the core, this lessens the spatial overlap of the functions resulting in the quasi type-II behavior.

2.4 Quantum Dots in Biological Applications

Interest in QD research was originally initiated towards understanding of their unique optical and spectroscopic properties, but has later been strengthened by several technological developments based on exploiting some of those properties[109-112]. Applications in optical-electrical devices[112-117] and photovoltaic cells[118,119] have also been supplemented by a high potential for use in biology.[12,64,120-124] Immunoassays,

cellular tagging, and tissue imaging by means of fluorescence labeling of biomolecules is a frequented technique in biotechnology which traditionally utilized organic fluorophores and fluorescent proteins.[125-127] All organic fluorophores and fluorescent proteins, however, have intrinsic limitations which lessen their effective use to develop targeted bioapplications which include: narrow absorption spectra for excitation, broad fluorescent emission spectra, and are easily susceptible to chemical degradation and photobleaching resulting in loss of the fluorescent signal.[123,124,128] QDs in contrast offer a number of exceptional properties which can offer substantial advantages in certain bioanalytical and imaging applications.[120,121,123,124] Depending on the composition, QDs can fluoresce light over a broad spectrum of wavelengths from the ultraviolet (UV) to the infrared (IR).[25,91,129,130] Additionally, the broad absorption spectrum ranging from the UV to the particle's band edge enables the possibility to simultaneously excite multiple different color QDs with a single excitation source. Therefore QDs are certainly apt for multiplexing applications. It has been established through several research groups that QDs conjugated with biomolecular targeting agents can be used in a variety of applications such as molecular detection, imaging, and diagnostics. Nevertheless, effective integration of QDs in biotechnology will unavoidably demand a thorough understanding of these hybrid systems.

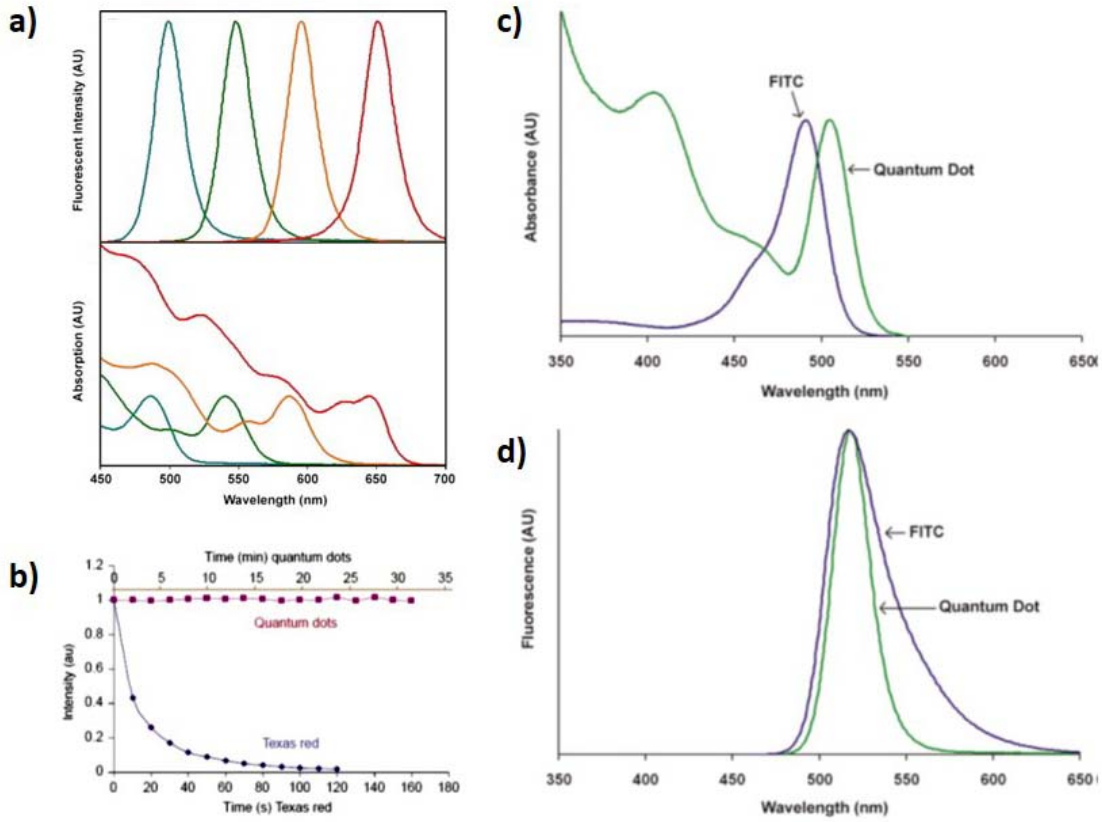

Figure 2.20 Comparison of Optical Properties of QDs to Organic Dyes. [figures from Smith et al.[131]] a) Fluorescence and adsorption spectra from a size series of CdSe quantum dots. Note that due to the broad absorption envelopes, simultaneous excitation of all the samples is possible with a single wavelength. b) Comparison of the fluorescent intensity of quantum dots compared to the organic dye Texas red over time (from Smith et al.[131]). As can be seen, the quantum dots have exceptional resistance to photobleaching not exhibited by organic dyes. Absorption and emission spectra side by side for a QD and FITC (c and d respectively). Here it can be seen that since organic dyes like FITC have a narrow absorption envelope, one is limited in the wavelengths to which can excite fluorescence, whereas with the quantum dot a much broader range is accepted. Also, the fluorescent emission peak from a QD is more narrow and symmetric than the dye.

2.4.1 Organic to Aqueous Solvent Transfer Method

Probably the utmost simplistic and obvious method for water soluble QDs is to perform the synthesis in an aqueous environment, of which methods have been

developed for CdTe particles.[132,133] Despite this simplicity, the most highly luminescent QDs which find use in biological studies have almost completely been prepared using high temperature solution routes in organic solvents. Due to being nonpolar as-synthesized, high quality QDs require phase transfer or water solubilization techniques in order to move on towards biological applications. Numerous solubilization methods have been advanced since the first reports on utilizing colloidal QDs as biological labels.[12,64] These methods can principally be divided into two main classes being cap exchange and polymer encapsulation.[124]

Cap exchange comprises of substituting the native organic stabilizing ligands with bifunctional ligands typically having a thiol anchoring group at one end and hydrophilic functions at the other end consisting of one or a combination of carboxyls, amines, amino acids, and/or polyethylene glycol (PEG) to increase affinity towards aqueous solutions. The ligand exchange proceeds through thermodynamically preferred binding and mass action kinetics. Examples of such ligands include mercaptoacetic acid,[64] mercaptoundecanoic acid,[134] dihydrolipoic acid (DHLA)[135] and DHLA-PEG conjugate ligands which can be carboxyl and amine-terminated,[136] along with polymers that have a combination of thiol and amine anchoring groups.[137]

The polymer encapsulation method consists of the as made (hydrophobic ligand capped) QDs encompassed within block-copolymer shells, phospholipid micelles, or amphiphilic polymers.[138-144] The polymers used usually contain hydrophobic carbon chains (that interdigitate with hydrophobic QD surface ligands) and a hydrophilic block

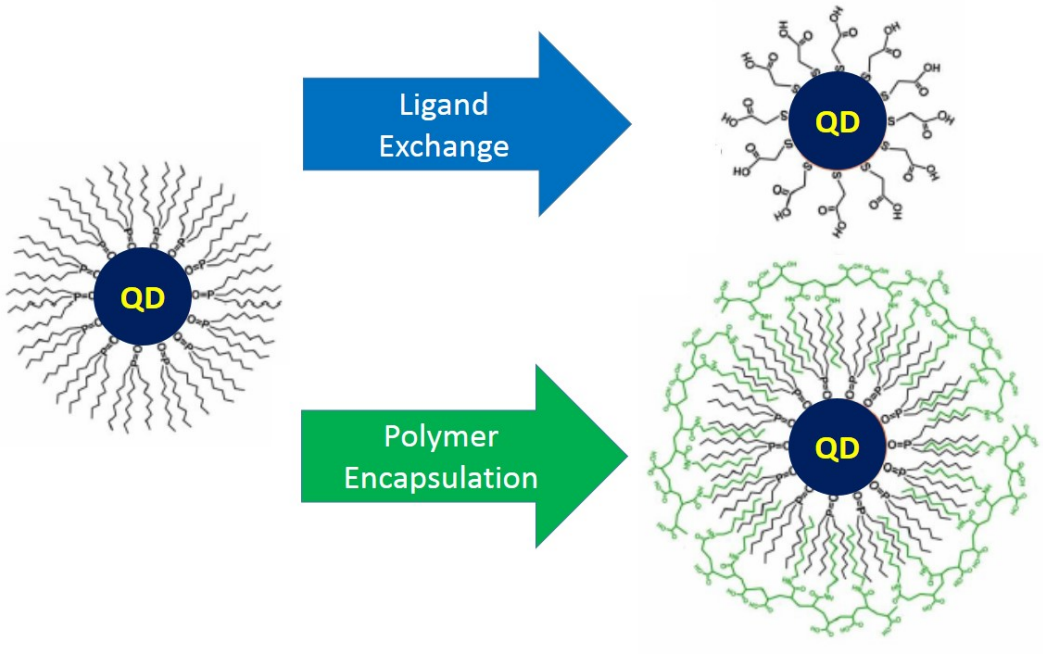

Figure 2.21 The Two Main Strategies for Aqueous Transfer of Organic Soluble QDs. One is ligand exchange depicted by replacement of trioctylphosphine oxide by mercaptoacetic acid. The other is polymer encapsulation depicted by a coating of octylamine modified polyacrylic acid which interdigitates into the alkyl branches of the trioctylphosphine oxide.

that extends into the aqueous solution imparting water solubility. In all solubilization strategies, hydrophilicity of the resultant particles is enabled by the presence of charged groups (carboxylic acids and amines) or PEG chains. Since these methods display bilayers of ligands encapsulating the particle, these tend to result in larger hydrodynamic diameters compared to the cap exchange methods.

Each of these two classes of solubilization has advantages and disadvantages. The ligand exchange tactic is simple and can be flexible in light of the recent advances of reproducible synthesis of modular ligands. It also enables smaller final particle sizes. The

disadvantage, however, is that the commonly employed thiol anchoring groups tend to decreased quantum yields compared to the native organic (carboxylates, phophonates, amines, and phosphines) stabilized nanocrystals. Polymer encapsulation is able to produce resultant particles with higher quantum yields, possibly due to keeping the native organic ligands adhered to the QD surface, though in some cases replacement of the native ligands with the block-copolymer was suggested.[140] Disadvantages are that this method tends to produce larger final sized particles and also limits control over the number of encapsulating chains draped around a QD, hence absence of information on the number of reactive groups is available for further functionalization. The choice of strategy is determined from the most benefit and least drawback in the intended application at hand.[124] The main guiding factors are high QYs, long term stability, and ease to conjugate bioactive moieties.

2.4.2 Bioconjugation Strategies

Approaches for conjugating hydrophilic QDs to biological targeting agents can in essence be divided into three groups: (1) The popular EDC (1-ethyl-3-(3-dimethylaminopropyl) carbodiimide) coupling of carboxylic acid terminal groups presented on the QD surface to amines on target proteins and peptides or vice versa.[136,139] (2) Metal affinity driven self-assembly using either thiolated peptides or polyhistidine affixed tracts which is versatile and has a reasonably low dissociation constant ($1/K_D$ ~ 0.5 – 50 nM).[145] (3) Avidin–biotin binding, which often involves the use of an avidin (or streptavidin) bridge between two biotinylated biomolecules (proteins, peptides) with

very strong binding having $1/K_D \sim 10^{-15}$ molar.[126] Each method for conjugation has its own particular advantages but also a few limitations, as with that presented for water solubilization approaches. For instance, EDC condensation reactions for QDs solubilized with thiol-alkyl-carboxylate ligands often yields intermediate aggregates due to poor particle stability in neutral and acidic buffers.[124] However, introducing a PEG chain between the thiol anchoring group and carboxylate groups, EDC coupling to QDs is highly effective.[136] The previous limitation may also be lifted by using QDs coated with functional peptides, where solubility is then determined by the peptide ligands.[146] EDC has also been applied to QDs encapsulated with polymeric shells bearing carboxyl groups.[139] On the other hand, this method can produce large conjugates with reduced control over the number of biomolecules per QD bioconjugate, which is a problem for biotinylation conjugation as well. Self-assembly of proteins/peptides onto the QD using metal-histidine-driven interactions can reduce aggregation and permit more control over the valence. However, it still necessitates that the receptor be engineered with the chosen His tag beforehand. Moreover, a recent study has shown that execution of this conjugation approach also requires that the His region be extended laterally for direct connection with the nanocrystal surface.[145]

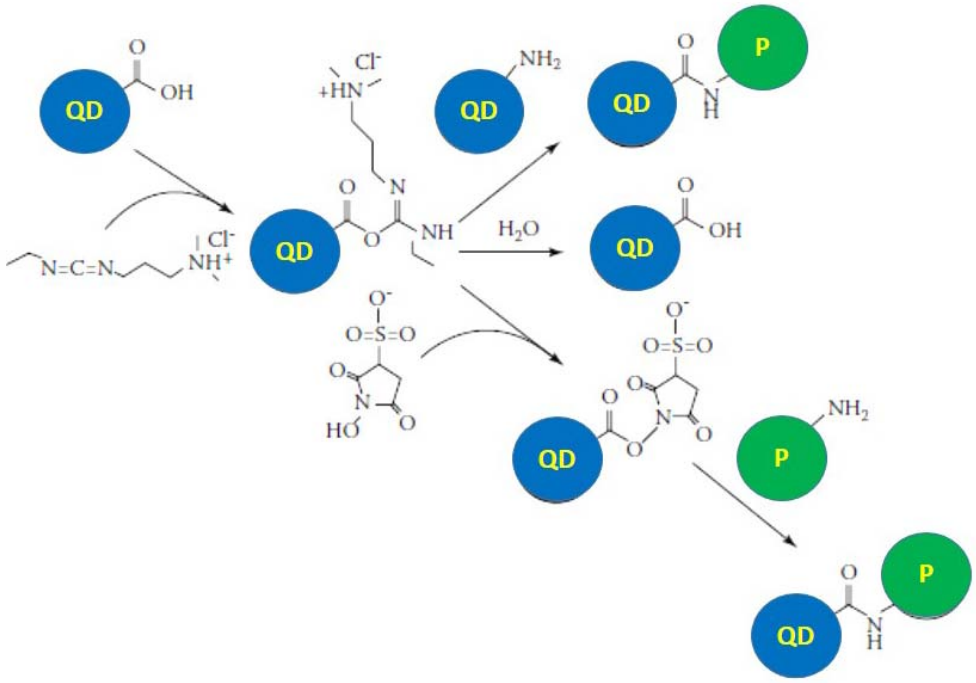

Figure 2.22 Using EDC Coupling for Biofunctionalizing a QD. [Adapted from Klimov[147]] Mechanism for the commonly employed EDC coupling technique to conjugate a quantum dot (blue circle) to a biomolecule (green circle).

2.4.3 Quantum Dots in Cellular and Tissue Imaging

The advantages provided by luminescent QDs, such as resistance to photobleaching, multiplexed imaging capacity, and high one and two photon absorption cross sections, have spawned remarkable interest for their use in cellular and *in vivo* imaging.[11,128,148-161] These properties can permit biomolecule tracking and deep tissue imaging over extended periods of time along with reduced autofluorescence. QDs, by exhibiting great resistance to photobleaching and chemical degradation, allow fluorescent tracking of cellular growth and division. This long term tracking also offers insights into whether or not nanoparticles obstruct key natural cellular processes.

For example, Dubertret et al.[138] microinjected phospholipid encapsulated QDs into a sole Xenopus embryonic cell and used fluorescence to monitor its division and development for several days. This study illustrated that the QDs were limited to the offspring of the injected cell and their existence did not cause any observable negative effects on growth and division of the cells.[138] Voura et al.[156] labeled different melanoma tumor cell lines each with a distinct QD color through cationic lipofectamine encapsulation, executed a tail vein injection of the cells into mice, then tracked the QD fluorescence by multiphoton fluorescence microscopy as the cells extravasated into lung tissues. No variance between labeled and unlabeled cells was observed in the study. Both studies indicate that QDs, either injected or uptaken, did not interfere with natural cellular processes which may be attributed to a well capped particle.

Due to QDs having very large two photon adsorption cross sections , which are about three orders of magnitude higher than those of regular dyes, deep tissue imaging and sensing is enabled with reduced background since far red and near-infrared (NIR) irradiations are used.[157] Larson et al.,[157] with CdSe/ZnS QDs, were able to visualize vasculature hundreds of microns deep within the skin of living mice. In comparison to fluorescein isothiocyanate (FITC)-dextran at its solubility limit, QDs allowed imaging at superior depths while using less excitation power. Specifically, using five times as much excitation power was only able to obtain blood flow measurements at half the depth permitted with QDs.[157]

An alternative to two-photon fluorescence imaging, which involves high powered pulsed laser excitation source, deep tissue imaging can use NIR fluorescence from QDs that have emission within the tissue transparency window (650-950nm). NIR emitting QDs could thus enable deep tissue imaging in animals with increased depth and reduced background. Kim et al.[158] have developed NIR QDs which permitted real time mapping of sentinel lymph nodes as deep as 1cm in animals during surgery.

2.4.4 Quantum Dot Toxicity Issues

Toxicity is possibly the greatest pressing issue which QD probes have faced since they were introduced to biological applications. The concern over toxicity arises predominantly from the heavy metals to which QD cores are composed of such as Cd. This perceived heavy metal toxicity has to some extent stifled the eagerness for widespread application of QDs in biology despite the great potential. Such issues need to be addressed if these probes are to find a broader use, especially for in vivo applications. Several studies proposed the cytotoxic effects connected with QDs may be mediated by leakage of metallic ions into the surroundings, which is believed to interfere with tissue and cell functions. Such potentially toxic effects can be reduced by coating the heavy metal containing core with other less toxic metals (e.g. Zn) and adding a protective hydrophilic coating such as PEG.[128,138-140,142,156] Another unsolved issue which remains is the clearance of the QDs from the body in live animal studies. Even though initial studies have shown that QDs can be quickly cleared from the blood circulation through urinary excretion, they can possibly accumulate in various organs (e.g., liver, bone

marrow, and spleen) depending on the particle size and coating[158,159]). Despite the unresolved long term toxicity issues associated with quantum dots, they are however quite suitable for single molecule tracking experiments of cellular components where experimental durations are short so toxicity issues altering cellular functions are minimized.

2.4.5 Quantum Dots in Single Molecule Tracking of Cellular Components

QDs by having a large Stokes shift, bright signals, and their resistance to photobleaching makes them great candidates as probes for single molecule imaging of cellular components. The large Stokes shift enables high signal to noise ratios which are required for precise localization of the probe to the nanometer scale. Most dyes, though some quite bright, have much overlap between their absorption and emission spectra. This limits the amount of fluorescent photons that can be collected by the detector in an imaging experiment where excitation filtering will block part of the molecule's emission spectrum. In addition, the photostability of QDs provides the ability for long term tracking. These three qualities of QDs make them superior to organic fluorophores for single molecule tracking, and such have been used in multiple single molecule tracking experiments of cellular membrane dynamics and intracellular trafficking.

Taking advantage of the great luminescent properties of QDs, Dahan et al. reported the first use of QD single particle tracking to explore endogenous glycine receptors (GlyR)

of rat spinal cord neurons.[11] In this study the authors were able to describe multiple GlyR diffusion domains in relation to the cellular localization, which were previously unresolvable by conventional ensemble methods. Since then, several reports have emerged aimed at addressing the specific biological functions of membrane protein subpopulations.

In the studies of membrane protein tracking, notable efforts utilizing QDs were made concerning the studies of the cholesterol and ganglioside GM1-enriched membrane microdomains.[162] Pinaud et al. created a glycosyl-phosphatidyl-inositol anchored avidin QD conjugate probe (AvGPI-QD) to investigate the connection between the diffusion of individual AvGPI-QD and the locality of GM1-rich microdomains in transfected HeLa cells.[51] Single AvGPI-QDs were discovered to show dynamic partitioning in and out of GM1-rich microdomains which were dependent on cholesterol concentrations. In another study, Chang et al. used a single QD tagged cholera toxin B subunit (CTxB) to study the diffusion dynamics and membrane compartmentalization of the GM1-rich microdomains for neuronal RN46A cells..[163] Their tracking measurements discovered that the single QD complexes undergo slower confined lateral diffusion within small domains near 200 nm in size.

Single QD tracking has also been successful in tracking endosomes and endocytosis of cells. Single particle tracking methods are a great benefit in this area compared to ensemble measurements as endosomal trafficking and endocytosis are known to be very heterogeneous in space and time. For example, axonal carriage of nerve growth factor (NGF), which aids in the growth and differentiation of neurons, is recognized to be

critical for neural cell survival. Though, tracking endosomes is quite challenging due to technical difficulties of imaging the processes in real time. Cui et al. were able to overcome such difficulties in which real time movement of NGF transport was tracked utilizing QDs in live rat dorsal root ganglion (DRG) neurons.[164] In this study, NGF−QD conjugates were permitted to bind and form complexes with NGF receptors and subsequently were internalized within early endosomes. Remarkably, endosomes containing NGF−QD were discovered to display "stop-and-go" retrograde transport toward the neuronal cell body with an average speed of 1.31 μm/s.

Despite the successes of single QD tracking of cellular components, one obstacle to still overcome is blinking where there can be prolonged periods of off states during the fluorescent intermittency of the probe. On one hand, this blinking property is commonly used as a measure for ascertaining single QDs opposed to aggregates are being imaged.[11,51,163-166] On the other hand, it raises concerns about the discontinuous trajectories obtained from single QD tracking due to repetitive prolonged disappearances of the probe location from the nonradiative events.[28] There have been a few reports on the synthesis of nonblinking QDs based on a thick shell method,[44,167]creating a parabolic gradient alloy core,[45] or solely using silicon for the core material,[55] and only two studies known to date have shown nonblinking QDs in single particle tracking experiments.[54,55] Such complete blinking suppression eliminates the ability to identify single probes from aggregates, due to aggregates appearing as a nonblinking entity. Therefore, a highly suppressed blinking probe, but still has little blinking, would be more favorable with off state periods just long enough to record the event while tracking to get the optical signature to confirm a single

probe. In addition, the giant shell and the silicon nonblinking probes applied to single molecule tracking experiments have been limited to CdSe/CdS and Si materials respectively. The gradient core dots present a more generalizable method which can extend to other materials, therefore expanding the emission wavelength possibilities, but these have yet to be demonstrated in a single molecule tracking study and their synthesis method is hard to reproduce.

CHAPTER 3

THEORY AND SYNTHESIS OF BLINKING SUPPRESSED QUANTUM DOTS

Fluorescence intermittency, or more commonly called blinking, refers to the stochastic interchanging of fluorescence emission intensity from a single molecule or quantum dot between radiative (on/bright) and nonradiative (off/dark) states despite being under continuous excitation. The intensity fluctuations between these emissive and nonemissive periods plotted over time often resembles the function of a random telegraph signal.[168] This binary on/off switching of the fluorescent signal, akin to having one's eyes continually being opened and shut, brings forth the term of blinking. Blinking seems an ever-present single molecule fluorescence phenomenon,[169] although scientific attention to the blinking behavior of colloidal quantum dots has spanned a tad less than two decades. Study in this area has largely ensued for two reasons. First, the unique and robust optical properties of QDs over conventional organic fluorophores[170] allow the examination of blinking in a wide variety of experimental conditions and with an unparalleled dynamic range in photon statistics.[171] Thus, QDs are model fluorescent entities in which to investigate the fundamental physics of blinking processes. Second, blinking is a great hurdle which restricts the usage of QDs in several applications. Specifically, applications that necessitate single photons on demand, such as single-biomolecule tracking[11] or single-photon sources for quantum optics are severely limited by blinking.[172] Other applications which can suffer through the loss mechanisms which are involved in blinking are QD based photovoltaics and broadly tunable QD lasers.[173]

Accordingly, there is a pronounced incentive to comprehend and possibly control the blinking in QD fluorescent emission.

3.1 Introduction to Quantum Dot Blinking

Numerous researchers have embarked on attaining a thorough understanding of the principal mechanisms resulting in QD blinking since fluorescence intermittency was first reported in CdSe QDs in 1996.[34,174] One of the main troubles has been developing physically relevant models that elucidate the on/off state statistics that are experimentally detected in single QD fluorescent traces. In these traces one discovers that the probability distributions of the on and off times, $P(\tau_{on})$ and $P(\tau_{off})$ respectively, generally fit nicely to a power law of the form $P(\tau) \propto \tau^{-m}$ over 4 orders of magnitude in time with *m* having values near 1.5 for both on and off times (shown in **Figure 3.1**).[175,176] This outcome is quite different compared to an exponential distribution, indicating a highly dynamic process rather than one obeying a more simplistic first order kinetic mechanism. Additionally, this power law behavior is typically unaffected from changes in the chemical composition of the QD, the size and shape of the QD, the temperature, the excitation power, and the excitation frequency.[176-178] This seemingly invariable blinking behavior to a multitude of experimental parameters has inspired the search for a universal mechanism to explain QD blinking.[27] Initial models considered the nonradiative state arising from a charged QD core which resulted from a photoionization process.[168,179] Each excitation event has a slight probability of creating multiple excitons within a single QD which can lead to nonradiative relaxation

pathways, specifically through Auger annihilation processes. Auger recombination refers to the phenomena where the annihilation energy of the electron-hole exciton pair does not end in photoluminescence, but rather is absorbed by the extra carrier where it may be expelled from the core into the continuum or another energy state. The three fermion process can occur for both a positive trion (2 holes and 1 electron) and a negative trion (two electrons and 1 hole) pathway. Such processes have the ability to transfer charge carriers to trap states on the surface of the QD. Then, upon absorption of a succeeding photon, the excited state of the QD would now be a trion containing an electron-hole pair and the remaining charge carrier which was not trapped on the surface of the nanocrystal. These pathways have greater efficiency in QDs than their bulk counterparts due to lifting the conservation of momentum since crystal momentum (k) is not a good quantum number for confined nanocrystals. In likeness to the enhanced Auger rates observed for biexcitons ($k_{Auger} \sim 10^{11} s^{-1}$),[180] a trion was hypothesized to be nonradiative owing to such increased Auger rates. These rates can easily compete with radiative rates ($k_{Rad} \sim 10^{8} s^{-1}$) leading to off states. The on state would return once the trapped charge returned to the NC core thereby eliminating the trion.

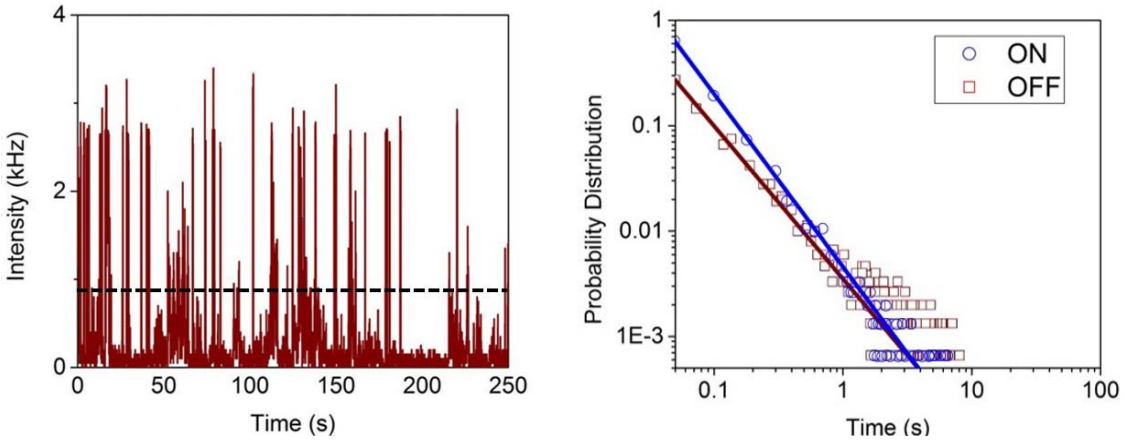

Figure 3.1 Dynamic Intensity Trace and Probability Distributions of On and Off States of Single Conventional Core/Shell QDs. Dynamic intensity trace of a single conventional core/shell QD (CdSe//ZnS) along with the sample's on and off probability distributions. The dotted line on the dynamic trace indicates the demarcation between an on and off state. It should be noted, however, that occasional grey states can appear which are at intensity values above the background but below the average intensity of the on states. The slopes of the off and on distributions (*m*) are 1.45±0.05 and 1.64±0.07 respectively.

Even though a simple Auger ionization model delivers a convincing physical description of blinking, it also has a number of problems. First, a model constructed only on Auger ionization is qualitatively inconsistent with the power law statistics of the on times.[171] The fundamental reason is that though electrons expelled to different trap states may happen with dissimilar rate constants, the total rate constant would be given by the sum of individual rate constants. In this case the overall decay of the on state could be described with a single rate constant which would erroneously predict exponential distributions.

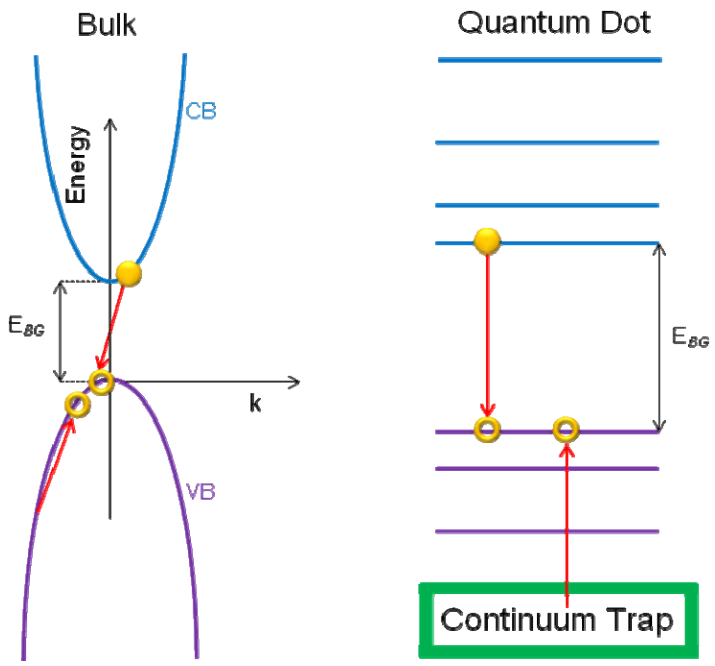

Figure 1.2 Auger Recombination Process in a Bulk Semiconductor and a QD. Depiction of Auger recombination of a positive trion of a direct bandgap semiconductor in the bulk and a quantum dot. Note the relaxation of the crystal momentum (k) conservation in the quantum dot due to the discrete energy levels instead of bands.

Second, observations of the Auger recombination rate of a negative trion (two electrons and one hole) of CdSe/CdS NCs show it is only about 2 times greater than the radiative rate of the neutral excitonic species.[181] This long trion lifetime indicates that the off state does not come from a negative trion. Whether or not the positive trion (two holes and one electron) also exhibits a comparable Auger rate, remains to be seen. Finally, it has been shown that the existence of a simple binary on or off levels is not entirely accurate, where QD blinking can have many "grey" states representing numerous intensity levels between on and off.[182] Nonetheless, these results have important implications for any charging-based theoretical model of NC blinking.

An alternative theoretical method to comprehend QD blinking uses diffusion based models. It is notable that molecular diffusion is a physical processes which results in power law behavior where the root-mean-square displacement is given by $\left\langle x^2 \right\rangle^{1/2} = \left(Dt\right)^{1/2}$, with D being the diffusion constant and t time. Diffusion-based blinking models have been developed in a couple different systems. In one situation, an electron is ejected from the QD core which then diffuses in the surrounding medium.[183] In another, diffusion of trap state energy levels and consequent spectral diffusion of QD core energy levels leads to the power law distributions.[176,184] The main idea of this model is that swift electron transfer occurs amid the QD core excited state and a trap state at or near the particle surface when the energies are resonant. The diffusion of the trap and excited state energies end with the probability of an electron remaining in the QD core proportional to $t^{-1/2}$. The probability density, which is the derivative of the probability to remain in the core, is proportional to $t^{-3/2}$. Thus the diffusion model predicts a power law exponent close to that experimentally observed for the on and off probability distributions. Finally, a complete analysis of the electron transfer mechanism in the Marcus theory framework focuses on large changes in the nonradiative electron relaxation rate as the main source of blinking.[185,186] This model circumvents the requirement to invoke a long lived electron trap state, though deep trapping of a hole is needed. Experimental observations have shown deviations from power law behavior on millisecond time scales and fluorescence lifetime measurements of QD ensembles,[187,188] which support such diffusion based models.

3.2 General Methods of Blinking Suppression

A simple description of fluorescent intermittency of single QDs is large fluctuations in the quantum yield over time. Therefore there are two general ways to mitigate blinking: increase the radiative rate and/or decrease the nonradiative rate. Early reports of suppressed blinking of single QDs have utilized both tactics. For example, CdSe cores near rough metal surfaces can display increases in emission intensities, decreases in fluorescence lifetimes, and subsequently reduced blinking.[189,190] These effects are a result of plasmon enhanced fluorescence which result in increases in QD radiative and absorption rates. Alternative blinking suppression methods have been dedicated towards modifying the QD itself as opposed to its environment. One method is to eliminate traps and the other is to weaken the fundamental nonradiative processes through band gap engineering.

3.2.1 Eliminating Surface Traps

The first successful method in suppression of QD blinking was accomplished through chemical treatment of the surface of the QD via the solvation medium.[42] Here, commercially available CdSe/ZnS core/shell QDs were tethered by a polymer to glass surfaces where blinking was virtually stopped by flushing aqueous solutions of beta-mercaptoethanol (BME) over the particles. When the BME was washed out with a Tris-HCl and NaCl buffer solution, the original blinking behavior returned. Through the study of the blinking suppression properties of BME and other substances known to be

antioxidants, the authors identified two characteristics of successful blinking suppression chemicals. Effective reagents have a thiol moiety and were sterically "small" as larger thiolated reducing agent molecules such as glutathione were observed to be ineffective. From these observations it was proposed that the mechanism by which small thiolated reagents suppress blinking is through a trap filling model. In this model, the off state of the QD is presumed to arise from a positive trion formation due to an electron being expelled from the CdSe core which becomes trapped at the surface of the ZnS shell. When small thiolated reagents are present in the solvating medium, their small molecular size permits them to diffuse and pack closely within the QDs polymer layer which then decreases trap states at the ZnS surface as thiols are mild reducing agents (donates electrons to trap). Having small thiolated molecules donating electrons to surface trap states reduces the number of traps accessible to the electrons ejected from the QD core, thus the charge trapping pathway of blinking would be suppressed.

Another approach in eliminating surface traps is to grow a thick shell around the QD core, otherwise known as "giant" shell structures. Whereas a conventional core/shell QD typically will have 2-5 monolayers (less than 2nm thickness) of shell material, giant shell QDs are produced with over 20 monolayers of shell material (>5nm thickness). Such structures have been synthesized using the CdSe/CdS core/shell system and have been observed to have great blinking suppression.[44,167] Here the great distance from the center of the QD to its surface will leave surface trap states inaccessible to electrons and holes which are confined within the core (low wavefunction probability reaching the surface). The fraction of nonblinking QDs was accordingly observed to increase with

increasing CdS shell thickness,[40] signifying that blinking is being diminished through insulating the electron and hole within the core of the particle from the surface of the shell.

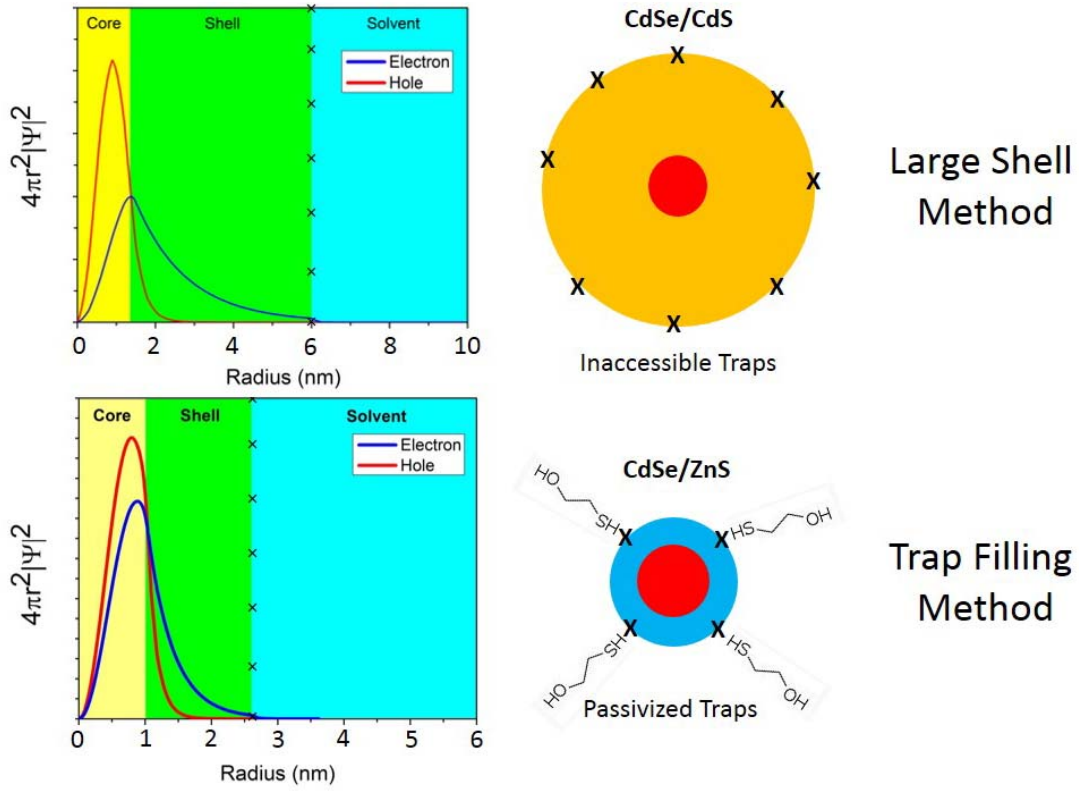

Figure 3.3 Comparison of the Giant Shell and Trap Filling Method for QD Blinking Suppression. Plots of the wavefunctions for the electron and hole for the CdSe/CdS giant shell and CdS/ZnS structures show for the large shell structure the carrier has low probability of reaching the surface, whereas with the traditional core shell particle of CdSe/ZnS the electron is a bit more likely to reach surface traps. By passivating all the traps which reside on the surface, the electron within the CdSe/ZnS structure has no trap to access.

3.2.2 Eliminating Internal Traps

From the method of the giant shell QDs, one would question whether other shell materials than CdS could be deposited on CdSe to a thickness which curbs the charge carriers from reaching the surface. However, when depositing multiple monolayers of an inorganic shell material with a different lattice constant than the QD core, defects such as loop dislocations may develop from the accumulated strain at the interface. These defects act as carrier traps deactivating luminescent recombination. Maintaining high quantum yields throughout the shell deposition process requires that the nanocrystals are free from defects.[191] Such deep interface traps from dislocations exhibit themselves as favored Auger recombination sites leading to nonradiative energy losses.[192]

Nevertheless, there can be a considerable amount of strain relief when using compositional grading to generate thick epitaxial layers opposed to depositing the pure lattice mismatched material directly upon the substrate.[193] Earlier work in semiconductor epitaxial substrate growth has shown linear compositionally graded alloys relieve interfacial strain and prevent dislocation formation at the epitaxial-substrate interface where they are most likely to nucleate.[194] Indeed it has been demonstrated that pure ZnS monolayers on CdSe cores had no effect on the blinking,[195] but compositionally graded steps from CdSe to a pure ZnS outer layer had lowered the fluorescent intermittency.[196]

For the evaluation of the thickness of shell material that can be applied upon a QD substrate before defects begin to form, one can apply the theory developed by Matthews[197] for layers of single composition and an analogous calculation by Fitzgerald[198] for compositionally graded layers following a linear function. The critical shell thickness is determined to be the point beyond which creation of a dislocation loop is more energetically favored than coherent (defect free) growth of the shell. This point can be calculated by equating the energy of the elastically strained state to the energy of the incoherent state, with the latter comprised from energy from both the defect and the residual elastic energy from strain. From the analysis of Matthews the critical thickness for a single compositional layer is determined to be:

$$h_C = \frac{b\left(1-\frac{v}{4}\right)}{\pi f\left(1+v\right)}\left(\ln\left(\frac{h_C}{b}\right)+1\right) \tag{3.1}$$

From the analysis of Fitzgerald the critical thickness for a linear graded compositional layer is determined to be:

$$h_C^2 = \frac{3}{4}\frac{b\left(1-\frac{v}{4}\right)}{\pi f\left(1+v^2\right)}\left(\ln\left(\frac{h_C}{b}\right)+1\right)\frac{\Delta h}{\varepsilon} \tag{3.2}$$

Here it is being considered the shell has a continuous linear graded profile from pure substrate at $h = 0$ to pure surface material at $h = \Delta h$. 60^0 dislocation formations have been assumed to be created once beyond the critical thickness and b is the Burgess

vector of type ½ *a* <110>. The Poisson ratio *v* is considered to be the harmonic mean of pure core and pure shell materials, *f* is the mismatch between the two pure materials, and ε is the strain between pure core and shell materials. The Poisson ratios and lattice constants used in the calculations of this work are $v_{CdSe} = 0.409$, $v_{ZnSe} = 0.372$, $v_{ZnS} = 0.388$, $v_{CdS} = 0.412$, $a_{CdSe} = 0.605$nm, $a_{ZnSe} = 0.567$ nm, $a_{ZnS} = 0.541$ nm, and $a_{CdS} = 0.583$nm.[199]

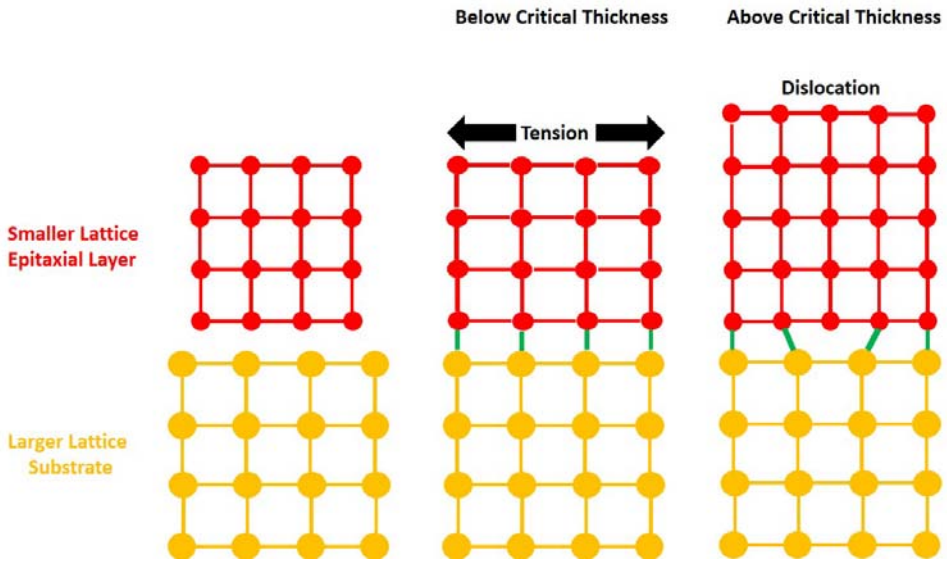

Figure 3.4 Epitaxial Growth upon a Substrate Using Lattice Mismatched Materials. When depositing multiple monolayers of a material upon a larger lattice constant substrate, there is a critical thickness that beyond which dislocations nucleate in order to relax the strain within the crystal lattice.

The critical thicknesses for pure shell CdS and ZnS on CdSe are determined to be 9.3nm and 1.8nm respectively. It is likely that the shell required to keep carriers' from reaching the nanocrystal surface for ZnS extends beyond the critical thickness for defect free epitaxy whereas with CdS, being better lattice matched with the CdSe core, the required thickness is possible to develop coherently. Indeed, it has been observed

that multiple monolayers of ZnS on CdSe cores leads to observable incoherent growth in subsequent shells,[95] while even for the largest of the giant QDs[44] the shell is less than the 9nm critical thickness for the CdSe/CdS system. The great difference in the critical thickness between ZnS and CdS shells upon CdSe can be realized from the difference in their lattice mismatches (10.6% and 3.9% respectively), where greater mismatches will lead to greater strains at the heterojunction. ZnSe on the other hand has a mismatch between these (6.3%),and has been reported that multiple monolayers lower photoluminescence[200] indicating possible interfacial defect formation. A pure ZnSe shell has a critical thickness of 4.4nm which can limit the ability to create a thick protective shell like the CdS system, but linearly grading the shell over this distance from pure CdSe to pure ZnSe however is determined to have a critical thickness almost 4 times this amount being 18.3nm. The shell being linearly graded allows the strain to be distributed throughout the nanocrystal and possibly enabling the shell layer to extend to thicknesses required to limit carrier probabilities to the surface without creating new internal defect traps. For visualization, **Figure 3.5** shows CdSe/ZnS compared to CdSe/$Cd_{1-x}Zn_xSe$. Here, CdSe/ZnS with multiple shells is developing interface dislocations from strain before it is able to keep the electron probability low at the surface whereas the CdSe/$Cd_{1-x}Zn_xSe$ structure distributes the strain throughout the crystal and therefore has no internal defects when developing a shell thick enough to keep the carriers from reaching the surface. Therefore grading the shells on CdSe cores can extend research on blinking suppressed QDs beyond that of mainly CdSe/CdS structures.

It should be noted that previous experimental results on core/shell particles with multiple epitaxial layers reveal that greater strain can be accepted in small nanocrystals than their bulk counterparts.[201] Small nanocrystals possess a high surface area to volume ratio and large curvature which permits the stress from a lattice-mismatched epitaxial shell to be spread over a greater fraction of the constituent atoms. Therefore, it is assumed that the values obtained from these considerations should be conservative. However, if shell growth is not uniform around the crystals, the calculated amount of material for coherent epitaxy may result in dislocations as some areas may have exceeded the critical thickness.

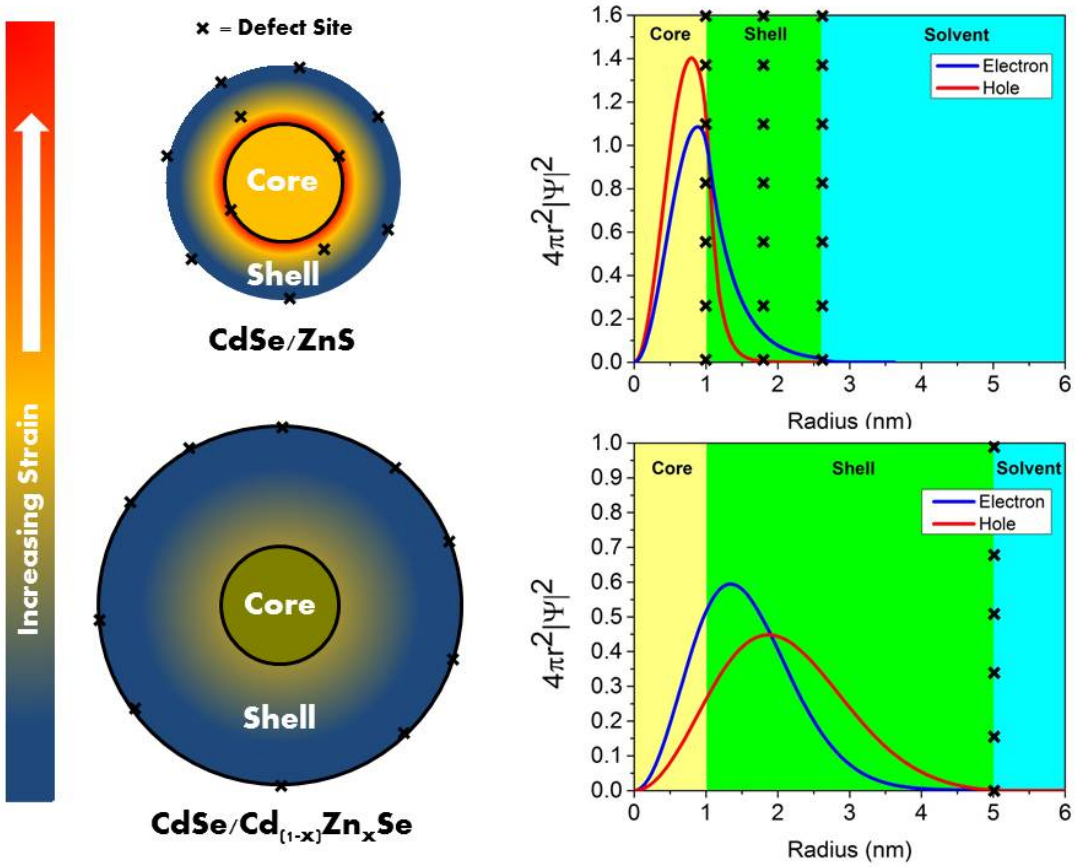

Figure 3.5 Strain Effects on Carrier Access to Trap Sites. Comparison of CdSe/ZnS and CdSe/$Cd_{(1-x)}Zn_xSe$ core/shell particles in terms of strain and possible defect location with respect to the exciton carrier probabilities.

3.2.3 Band Gap Engineering

While counterintuitive to the charge trapping models of QD blinking, an alternative approach to suppress blinking would be to alter the fundamental physical properties in such a manner that the QD will remain on even if a trion is formed. Having considered the origin of the enhanced Auger processes in QDs, Cragg and Efros published a theoretical report suggesting an approach to achieve blinking suppression based on band gap engineering of the core/shell material interface.[40] In conventional

core/shell QDs, the heterojunction between the core and shell materials is abrupt, thus the confining potentials for the electron and hole are abrupt and step-like. At these abrupt potential steps, charge carriers can obtain ample momentum to contribute to an Auger excitation process.[40] For QDs with a smooth potential (no discontinuities), however, are expected to have slower Auger rates as electrons and holes at the conduction and valence band minima (k = 0) are lacking the crystal momentum to promote a third charge carrier to an excited state. In depth calculations support this expectation, predicting that the nonradiative Auger recombination rate of QDs with a smooth potential could be lowered several orders of magnitude relative to traditional abrupt potential core/shell particles.[40]

Currently there are no systematic experimental studies linking the smoothness of the QD confinement potential to the observed Auger rate nor to blinking behavior. Yet, reports have yielded outcomes consistent with this prediction. One example is $Cd_{1-x}Zn_xSe$/ZnSe gradient core/shell structures which showed complete absence of blinking.[45] The authors claim that blinking was suppressed up to hours of continuous excitation without the need of chemical treatments of the nanoparticle surface. In this study, suppression of the Auger effect was proposed to be due to a smooth confinement potential resembling a parabola originating from a $Cd_{1-x}Zn_xSe$/ZnSe alloy structure, where x smoothly changes from 0 at the center to 1 at the surface of the QD. Direct proof for the gradient of the core composition was not obtained, and the indication for the gradient composition came from theoretical models of the confinement potential.[45] The properties of these $Cd_{1-x}Zn_xSe$/ZnSe QDs remains questioned, and other hypotheses

for the absence of blinking have been suggested, including a surface-trapped hole (negative trion) or through chemically reactive organic molecules interacting with the QD surface.[202] Additionally, giant shelled CdSe/CdS QDs which showed Auger rate suppression by several orders of magnitude were partially explained by a softening of the confinement potential, although no direct evidence of the compositional structure was reported.[203] However, these reports of nonblinking QDs have produced a general methodology to blinking suppression through smooth potential architectures.

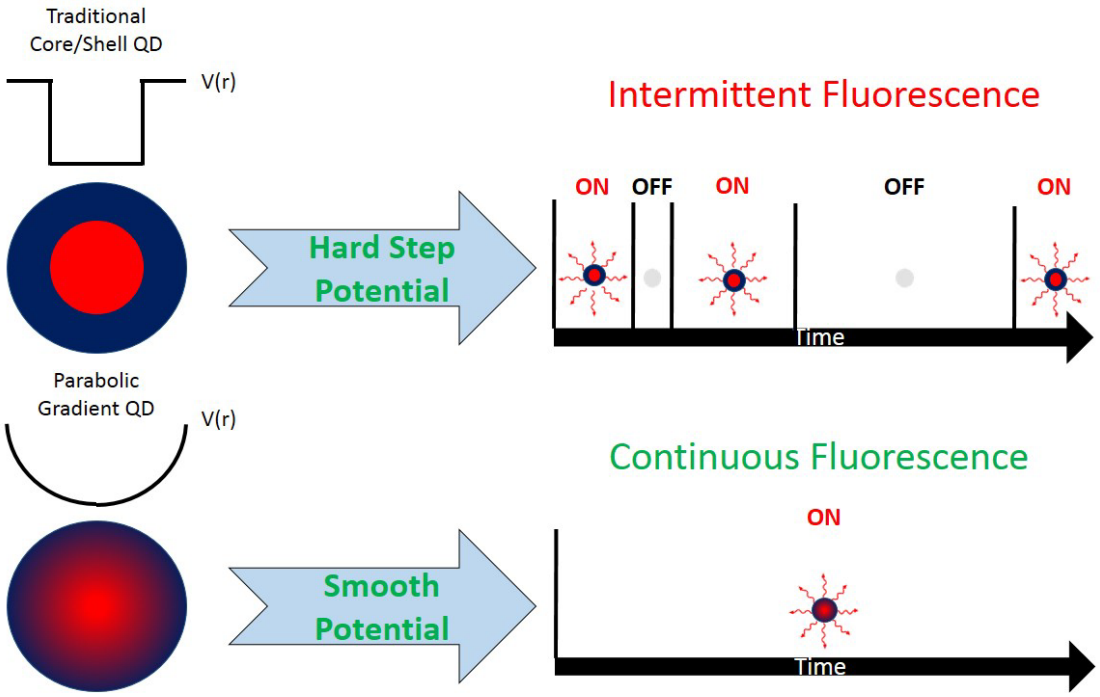

Figure 3.6 Complete Blinking Elimination Through Parabolic QD Potentials. Traditional core/shell QDs may have abrupt potential jumps at the heterojunction leading to intermittent fluorescence from enhanced nonradiative trion pathways due to discontinuities in the potential. Parabolic graded QDs on the other hand are supposedly continuously fluorescent due to carriers not being able to gain enough crystal momentum to promote a third charge carrier to an excited state for such nonradiative trion processes.

The report from Cragg and Efros[40] not only indicated smoothness of potential lowering Auger rates, but also that delocalizing the carriers throughout the nanocrystal volume will as well. From calculating the Auger lifetime using Fermi's Golden Rule (Equation 2.13), following the methodology of Cragg and Efros,[40] one gets the proportionality for the Auger lifetime

$$W_{i\to f} = \frac{1}{\tau_A} \propto \left|\psi\left(k_f\right)\right|^2 . \tag{3.3}$$

In words, the Auger lifetime is inversely proportional to the absolute square of the Fourier component of the carrier wavefunction. To picture this Auger rate proportionality, consider wavefunction solutions of Gaussian curves of the form

$$\psi(x) = Ae^{-\frac{x^2}{4\alpha}} . \tag{3.4}$$

Using this form yields a straightforward result (simple Fourier transform) of the Auger rate proportionality

$$\frac{1}{\tau_A} \propto e^{-2\alpha k_f^2} . \tag{3.5}$$

The proportionality indicates that as a carrier becomes more spread throughout the nanocrystal's volume (an increase in variance in terms of a normal distribution in x space), the Auger timescale will increase leading to a reduction in its rate (a decrease in variance in k space). Delocalization will occur for the electron (hole) carrier if the

conduction (valence) band offsets at the heterojunction are not large. Large off sets will prevent the wavefunction being able to leak out of the core. If the electron wavefunction is delocalized over the QD volume, the negative trion Auger pathway is suppressed and similarly if the hole is delocalized the positive trion pathway will be suppressed.

To investigate a shell material preferred in Auger rate reduction of CdSe cores, wavefunction solutions of the electron and hole carriers were obtained by solving the Schrodinger equation in the effective mass approximation for nanocrystals of varying core diameters and shell thickness. In these calculations, finite solvent barriers wells were used to reduce the error which occurs for small crystals using infinite potentials as presented with the Brus model in Chapter 2.[204] Though, the solvent barriers are quite large and allow very little wavefunction leakage beyond the surface of the nanocrystal. Therefore to spread the carrier wavefunction, the shell needs small offsets in which the carriers can tunnel. As can be seen in **Figure 2.7**, the calculations show that among the popular type-I shell material choices for CdSe cores, where the shell's conduction (valence) band is higher (lower) than the core, ZnSe will be the most effective in delocalizing both carriers. The electron can be delocalized effectively with moderate band offsets due to light effective masses, but for the hole with larger effective masses, small off sets are needed for the wavefunction to span the particle volume. CdS having a small electron offset but a substantial hole offset will delocalize the electron but keep the hole confined. This leads to the development of quasi type-II behavior for multiple shells in these systems. ZnS on the other hand has substantial offsets for both carriers and therefore will keep them confined within the core upon additional layers.

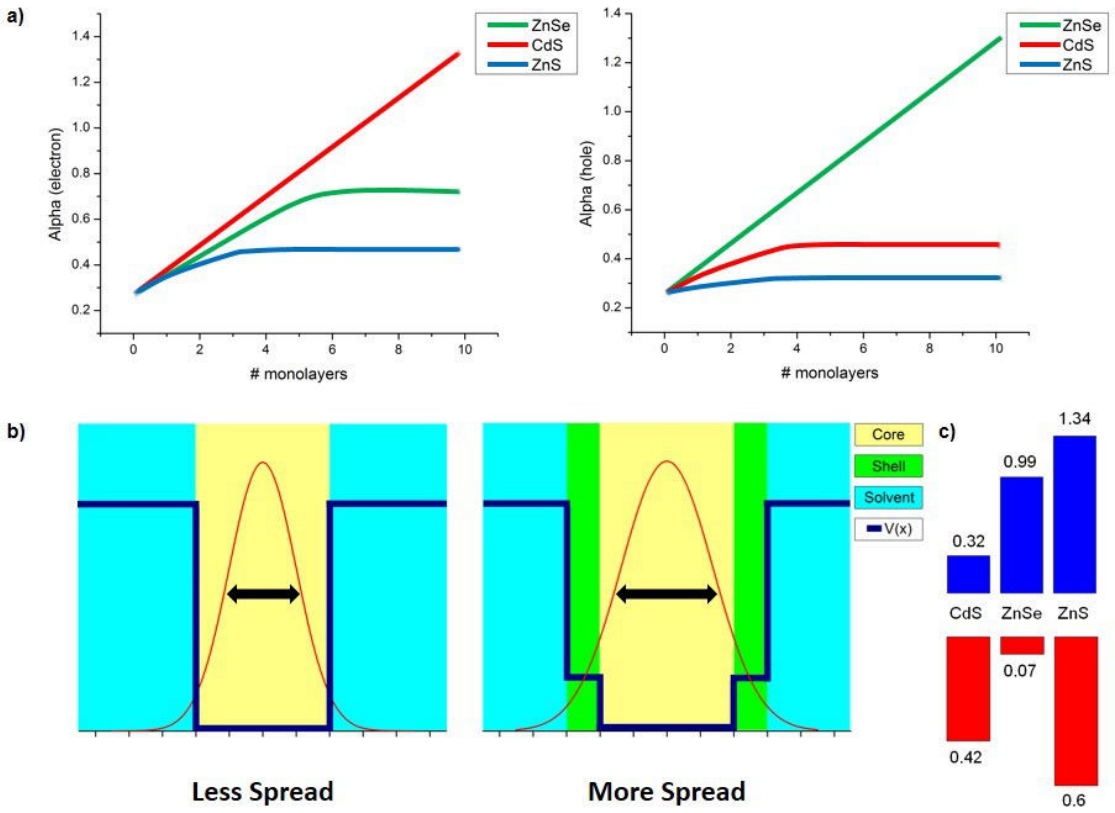

Figure 3.7 Band Offsets Determine Degree of Wavefunctions Spreading. a) Plots of the alpha (α) parameter vs. monolayers of shell material of both carrier wavefunctions for a 3nm diameter CdSe core. **b)** Plots showing the increase of accessible volume to the wavefunction when a small band offset shell is added around the core. **c)** Values in eV of the valence (red) and conduction (blue) band offsets of shell materials used in a to CdSe.

Another successful method for Auger suppression relies on the use of type-II or quasi-type-II core/shell QDs,[173,203,205-208] though the origin of the suppression in these structures has yet to be elucidated. On the one hand, there is a decrease in the electron–hole overlap as one carrier is confined towards the core while the other is more in the shell. Since Auger processes are of Coulomb nature the electron-hole localization evidently contributes,[205] and structures where the overlap is small typically do not exhibit complete Auger suppression.[167,209] On the other hand, there are likely interface

effects which contribute to the Auger process as well. Experiments in CdSe/CdS QDs show that charge carrier overlap alone cannot describe the observed Auger lifetimes, and interfacial alloying (smoothing the confinement potential) may provide a significant contribution in the Auger rate reduction.[209] However, type-II (and quasi type-II) structures have longer lifetimes and generally have lower quantum yields than type-I QDs. It would be more desired to increase the Auger lifetime while maintaining short radiative lifetimes to increase luminescent efficiency. By looking at the luminescence efficiency equation (Equation 2.12) it can be seen that longer radiative lifetimes may lead to less fluorescence.

3.3 CdSe/$Cd_{1-x}Zn_xSe$/ZnSe Linear Graded Alloy Shell System

The CdSe/$Cd_{1-x}Zn_xSe$/ZnSe linear step graded alloy shell system, whereby x increases by 0.1 per monolayer to pure ZnSe, was picked to synthesize and study on account of the following desired properties described in the previous sections: being able to spread both carrier wavefunctions throughout the entire volume of the nanocrystal, maintaining a high overlap of carrier wavefunctions, minimizing the strain throughout the particle, and diminishing the escape probability of the carriers from the nanocrystal. In addition, a synthesis procedure where only one of the elements is changing is a more facile approach than grading ZnS where each layer would have to change the ratios of both the cations and anions.

3.3.1 CdSe Core Synthesis

Due to the anticipation for adding multiple monolayers of shell material, small starting cores are desired in order to achieve final QDs of reasonable sizes. Synthesis of small CdSe cores (~2nm) employed a modified approach of the hot injection of a trialkylphosphine-selenium solution into a cadmium organic acid complex dissolved in the non-coordinating solvent octadecene (ODE),[210] whereby the cadmium is complexed to a phosphonic acid and a long chain alkylamine is added to the solvent. Using phosphonic acids, such as tetradecylphosphonic acid (TDPA), to coordinate cadmium enables smaller diameter particles to be obtained resulting from slower growth rates even at temperatures exceeding 295^0C.[211] Addition of long chained alkylamines, such as hexadecylamine (HDA) or oleylamine, to the solvent before the chalcogenide solution injection prepares higher quality particles by having high packing densities to eliminate surface traps and builds a diffusion barrier for complexes during crystal growth, thus adding another measure in keeping nanocrystals small and spherical.[212,213]

Specifically, CdSe cores were synthesized by the following procedure: 0.6 mmol of CdO and 1.4 mmol of TDPA were added to a 250 mL flask with 25 mL of ODE. The mixture was heated to 120^0 C under vacuum for 2 hours to remove water and oxygen. After purging 3 times with argon, the mixture was heated to 320^0 C under inert gas until the initially brown (color of CdO insoluble) solution became clear indicating that the cadmium has complexed with the phosphonic acid. The mixture was then cooled to room temperature and 6 grams of ODA were added. Again, the solution was heated to 120^0 C

for 2 hours under vacuum, and then purged three times with argon. In a separate 100 mL flask, a 7.5 mL solution of 0.4 M of TOP-Se in TOP is previously made by dissolving Se powder in pure TOP. Here Se powder is added to TOP where the flask is then evacuated and put in inert atmosphere in the same manner as the other reaction flask. Once under argon the flask temperature is raised to 160^0 C, where it is left overnight then cooled to room temperature. The temperature in the cadmium precursor flask is set to 290^0 C when the solution of TOP-Se is swiftly injected. After injection, the flask is immediately removed from the heating mantle and placed under forced air to quickly bring the solution to room temperature which prevents much of the growth phase for the crystallites. Resulting cores are 2.1 nm in diameter and have their first exciton peak at 480 nm and fluoresce at 490 nm. The typical FWHM of the fluorescent peak is 30 nm and HRTEM size dispersion is 0.3 nm or one monolayer equivalent. The quantum yield of the particles is typically low ($\leq$ 10 %) as small crystallites have more surface per volume leading to more trap states for nonradiative recombination.

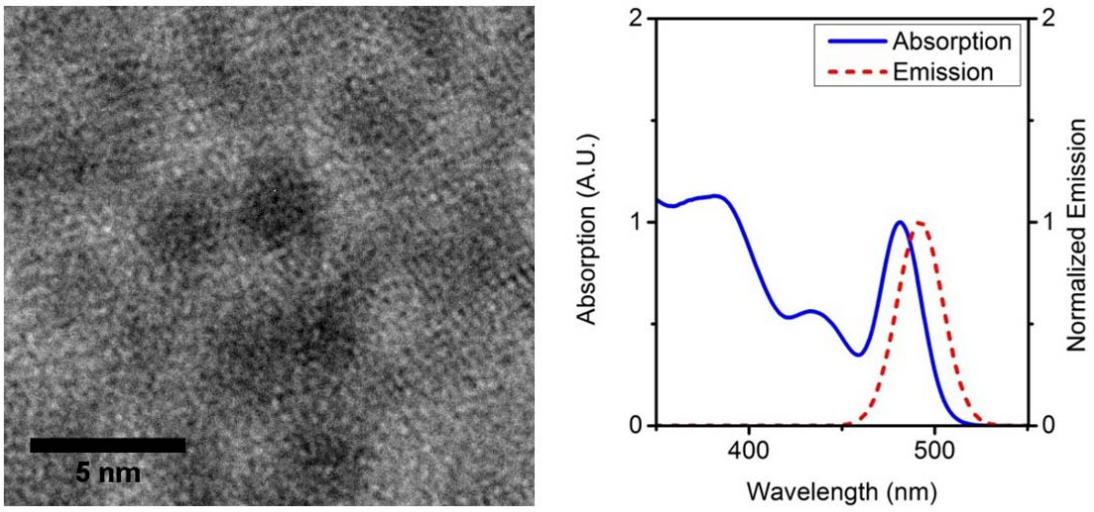

Figure 4.8 TEM and Adsorption/Emission Spectra of Small CdSe QD Cores. Small CdSe cores synthesized through the quick injection method. Average diameter of the particles is 2.1 ± 0.3 nm which is a standard deviation equivalent to one monolayer. The first exciton peak is centered at 480 nm and the emission peak is centered at 490 nm with a FWHM of 30 nm indicating a monodisperse solution.

Particle sizes and concentrations of CdSe QD solutions may be determined through developed empirical relations based on simple absorbance measurements. Particle size can be determined through the first exciton peak in the absorption spectrum through the following empirical equation developed by Peng.[214]

$$D_{CdSe}(nm) = \left(1.6122\times10^{-9}\right)\lambda^4 - \left(2.6575\times10^{-6}\right)\lambda^3 + \left(1.6242\times10^{-3}\right)\lambda^2 - \left(0.4277\right)\lambda + 41.57 \quad (3.6)$$

Using the first exciton (first peak on the longer wavelength side of the absorption spectrum) location of 480 nm yields 2.17 nm for the diameter which is close to that inspected by HRTEM. The molar extinction coefficient is determined from the following empirical equation.[215]

$$\varepsilon_{1s}\left(M^{-1}cm^{-1}\right) = 155507 + 6.67054\times10^{13}\exp\left(-\frac{11752}{\lambda}\right) \quad (3.7)$$

With this equation one can determine the concentration of nanocrystals in solution through the Beer Lambert law.

$$A = \varepsilon_{1s} cl \quad (3.8)$$

Here A is the absorbance, c is the concentration, and *l* is the path length of the cuvette. λ is the location of the first exciton peak and for both equations of 3.6 and 3.7 has units of nanometers. These empirical relations allow a quick and reliable determination of size and concentration of CdSe QD solutions through simple UV-Vis spectra without the need for more laborious methods of matching TEM with ICP-MS data.

3.3.2 Purification of CdSe Core Nanocrystals

Cores prepared by the methods described previously were diluted to a 1:5 ratio of reaction solution in hexanes and centrifuged at 5000 rpm to remove insoluble cadmium precursors. The particles were then precipitated with acetone and washed several times in methanol and hexane extractions. Unreacted cadmium and selenium precursors are soluble in methanol whereas nanocrystals are not. On the final extraction, the QDs were concentrated to 10-50 μM with the addition of excess methanol. These hexane solutions

of nanocrystals were then centrifuged to remove potential aggregates, bubbled with argon to remove oxygen and water, and stored at 4^0 C for one day. During this time a small amount of white precipitate typically formed which was likely unreacted cadmium phosphonates, and was removed via centrifugation prior to shell growth.

3.3.3 Precursor and Ligand Choices for Synthesizing the $Cd_{1-x}Zn_xSe$ Graded Shell

The cationic precursors of dimethylcadmium ($CdMe_2$) and diethylzinc ($ZnEt_2$) are chosen due to the smallness of the starting cores. It is important to have precursors that are reactive enough at lower reaction temperatures as to prevent Ostwald ripening of the cores. Metal-oleates typically require temperatures above 160^0 C to have sufficient reactivity which is beyond the temperature where ripening occurs for CdSe cores having diameters of 2 nm or smaller. The more reactive precursors, compared to the more commonly applied fatty acid complexes, can also better balance the reactivity difference of Zn and Cd precursors allowing more homogeneous shell deposition as zinc-carboxylates have lower reactivity compared to their cadmium counterparts.

Careful considerations had to be made in the choice of the chalcogenide precursor to maintain uniform spherical growth of the particle shell. It was noticed that the traditional route of using phosphines to solvate selenium prevented the ability to deposit multiple monolayers of shell in an isotropic manner. Studies have revealed that phosphines in the growth medium leads to development of hexagonal lattice structures in nucleated cubic phase CdSe crystals[216] which may prevent isotropic growth by having an aspect ratio, whereas cubic lattices do not.. Selenium powder can be

dissolved in ODE to avoid phosphines, though using this as the precursor was avoided due to the possibility of loss of activity for prolonged dissolution times at 200^0 C.[217] Considering limitations of the commonly used selenium precursors, $(TMS)_2Se$, was chosen owing to its high solubility in organic solvents and reactivity.

$(TMS)_2Se$ having high reactivity presents a potential loss of selenium metal to the syringe wall when delivering the solution. To lower the reactivity of the precursor in solution, tetradecene (TDE) is used as the solvent and kept at 4^0 C. TDE is chosen by having a boiling point being beyond the highest growth temperature used and can be cooled to temperatures which prevent substantial decomposition of the reactant during capping without solidifying (-13^0 C mp, 251^0 C bp). The traditional solvent of octadecene has a melting point of 14^0 C, and hence will solidify at 4^0 C. Only small aliquots of the precursor are taken out during the capping procedure in order to prevent sufficient time for raises in solution temperature.

The reaction vessel starts with the CdSe cores solvated in a mixture of dioctylamine (DOA) and ODE. The reasoning behind using DOA is that softer Lewis bases than primary amines tend to avoid the surface phase restructuring of CdSe which can lead to faceting or anisotropic growth when using oleylamine.[218] As subsequent shells are deposited and gaining higher zinc content, the more primary amine will be introduced into the system since the cation precursors are dissolved in oleylamine. The primary amines will eventually dominate over the secondary amine for surface coverage of the crystals through mass action. Primary amines are favored in the later stages of shell growth as they provide a good platform for keeping larger particles

soluble (by staying bound to the particle surface) when surface energy starts decreasing and dative bonding of secondary amines becomes weaker.

With the increasing zinc in the alloyed shell, there is a substantial increase in the enthalpy of phase transformation from cubic zinc blende to hexagonal wurtzite, therefore particles are able to maintain coherent structural and isotropic growth with gradual addition of primary amines. Harder Lewis bases than the primary amines such as trioctylphosphineoxide should be avoided as they bind too strongly to Zn[91] (harder Lewis acid than Cd) which can reduce reaction rates or prevent subsequent shell addition. It is also noted that there are no solubility issues with increasing particle sizes as seen with the multi-shell CdSe/CdS architectures. It is believed that since the giant shell QDs are grown in an anisotropic wurtzite dominant phase,[219] where one end is terminated by a positive (0001) cadmium face and the other by a negative $(000\bar{1})$ sulfur face , therefore a large dipole is formed which causes particle aggregation through electrostatic attraction. The graded step shell particles in this study are dominated by ZnSe content that thermodynamically favors the zinc blende phase which leaves the particles with an overall nonpolar behavior due to having each ionic face balanced by the counter ion both laterally and axially.

3.3.4 CdSe/$Cd_{1-x}Zn_xSe$/ZnSe Synthesis

200 nmol of the purified solution of CdSe QDs was placed in a mixture of 5 mL of ODE and 5 mL of DOA. The solution was then heated to 110^0 C under vacuum for 1 hour and later purged with argon three times to remove water and oxygen. Shell addition for the graded alloy QDs was performed by introducing calculated amounts of

glove box prepared 0.1 M solutions of dimethylcadmium and diethylzinc combinations in oleylamine, and $(TMS)_2Se$ in TDE separately by a syringe pump at a rate of 0.5 mL/hr. A single monolayer was deposited in a day then left to anneal overnight at 60-80^0 C. Since the graded alloy proceeds in increments of x = 0.1 for each monolayer, then an additional 4 monolayers of ZnSe are added, the total reaction time is 14 days. Shell growth temperatures start at 130^0 C and work up to 240^0 C as sequential layers are added to improve the crystallinity of the final products.

Reaction progress is continually monitored by UV-Vis and emission spectra of the particles. As can be seen in **Figure 3.9**, there is decreasing emission energy as subsequent monolayers of shell material are added, while there is an increase in the absorption at shorter wavelengths. This is an indication of the wavefunctions of the carriers gaining more volume (less confined), along with increases in the absorption cross section from the particle enlarging and gaining more ZnSe character. The energy profile with monolayer addition is qualitatively similar to that of what would be expected from theoretical calculations.

The final particles were found to be monodisperse with sizes of 10.1 ± 1.2 nm and have good crystallinity from inspection through high resolution TEM. The fluorescent emission peak center is near 620 nm with a FWHM of 40 nm and the quantum yield is near 50 %. Quantum yields are obtained by using a standard of fluorometric grade Rhodamine 6G (R6G) dye dissolved in methanol for QD solutions in hexanes from the equation below.

$$QY_{QD} = QY_{R6G} \frac{I_{QD}}{I_{R6G}} \frac{A_{R6G}}{A_{QD}} \frac{n_{QD}^2}{n_{R6G}^2} \tag{3.9}$$

Here QY_{R6G} is the quantum yield of the standard R6G in methanol having a value of 0.95. I_{QD} and I_{R6G} are the integrated fluorescent spectra from the QD and R6G samples respectively. The spectral intensities of the data are corrected for the changes in quantum efficiency of the detector at different wavelengths. A_{QD} and A_{R6G} are the absorbances of the solutions at the wavelength of excitation of the sample for the fluorescent spectra. In this case it was 450 nm excitation for the QD sample and 525 nm for R6G. n_{QD}^2 and n_{R6G}^2 are the refractive indices squared for the solutions of the QD (hexane) and R6G (methanol) samples respectively.

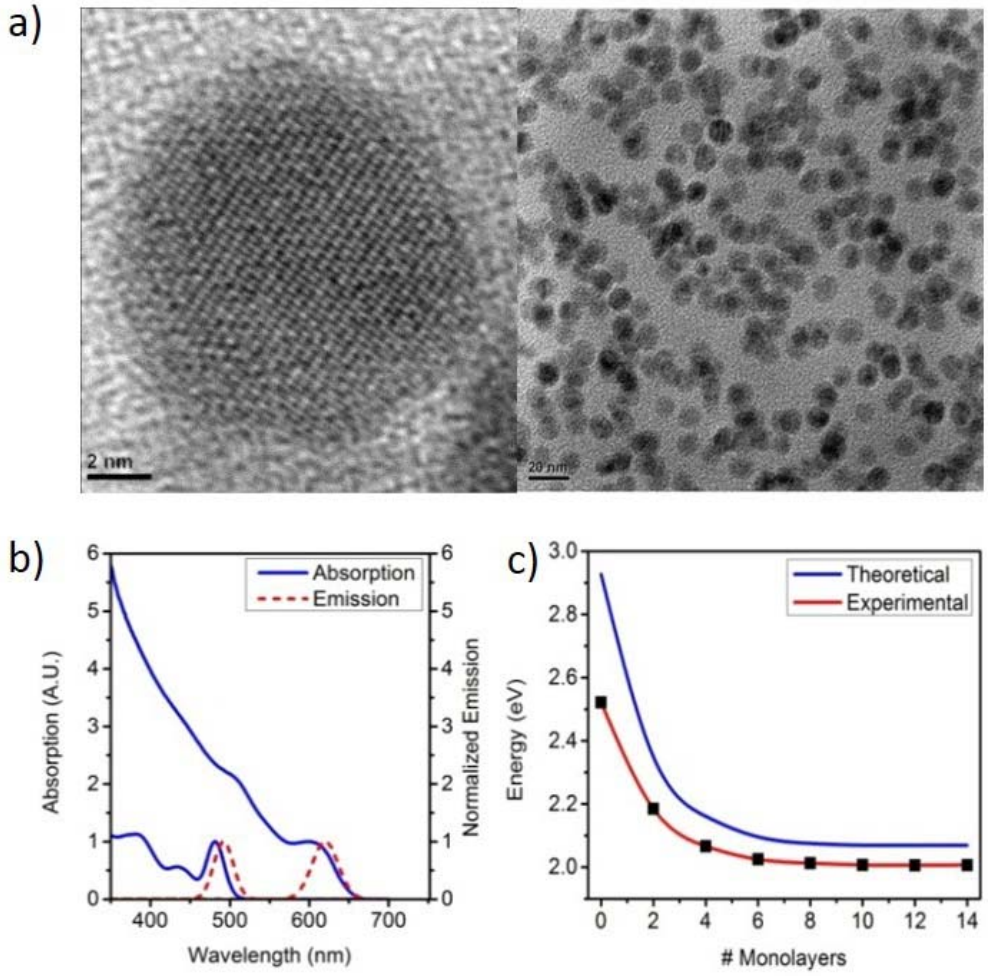

Figure 3.9 HRTEM and Adsorption/Emission Spectra of the Step Graded Alloy Shell QDs. (a) HRTEM images of a single and the ensemble of the final CdSe/ $Cd_{1-x}Zn_xSe$ linear step graded alloy shell QDs. (b) Normalized absorption and emission spectra of the initial cores and the final core/shell particles. (c) Calculated energy curve using the effective mass approximation for a CdSe/ $Cd_{1-x}Zn_xSe$ core shell particle where the core radius is 1nm and the shell is graded in linear steps of x = 0.1 with an additional 4 monolayers of pure ZnSe alongside the observed emission energy of the as-synthesized particles.

3.3.5 Ligand Synthesis and Phase Transfer for Aqueous Solubilization

Due to the interest for eventual application to single molecule biological experiments, the particles must be transferred to an aqueous phase. Three different

ligands were chosen to stabilize the particles. The first strategy consists of using a methoxy terminal 750 molecular weight polyethyleneglycol (PEG) amine linked to thiotic acid by an amide bond[220-222] (TA-750PEG-OCH3), the second method uses poly(ethylene glycol) methyl ether thiol of 5000 molecular weight (SH-5000PEG-OCH3), and the third strategy (aimed at minimizing the hydrodynamic size of the particles for minimal diffusion interference when attached to biomolecules) utilizes a multifunctional multidentate polymer encapsulation.[137]

Thioctic acid conjugated to 750 molecular weight methoxypolyethylene glycol amine followed a similar procedure to that presented by Mei et al[223] where equimolar amounts of each are reacted with DMAP and DCC in methylenechloride. The disulfide bond is then reduced using $NaBH_4$ in a methanol and water solution. Preparation of the multidentate polymer followed the procedure outlined by Smith and Nie.[137] Here polyacrylicacid is functionalized with thiols and amines by adding cysteamine and Fmoc-ethyldiamine through DIC and NHS in DMSO, later deprotecting the amines by piperidine. Poly(ethylene glycol) methyl ether thiol is used without any modifications. For ligand transfer of the TA-750PEG-OCH3 and poly(ethylene glycol) methyl ether thiol, QDs were performed similar to the method of Kang et al[224] where the QD solution and ligands are dissolved in chloroform, stirred under mild heating, then PBS is introduced into the solution. Typical QD concentrations are ~5 μM and polymer concentrations in slight excess of a 1 molar ratio of cations. The transfer method for the multidentate polymer follows the same procedure as the article.[137] Here QDs are first transferred to thioglycerol ligands and solvated in DMSO where a DMSO solvated

polymer is introduced then the solution is heated to 80^0 C for 2 hours. All QDs are then purified by either 30 kDa centrifugal filters (Amicon) or 25 kDa dialysis tubing (Spectra/Por).

After ligand transfer of the quantum dots, all solutions were solvated in water. From the DLS measurements of the particles, hydrodynamic diameters of 14 ± 2.0 nm, 19 ± 3.2 nm, and 22 ± 4.1 nm were observed for the QDs having ligands of the multidentate polymer, TA-750PEG-OCH3, and SH-5000PEG-OCH3 respectively. Surprisingly no observable changes in the quantum yield of the particles were detected regardless of the solvating ligand encapsulating the particles. Decreases in quantum yields are typically observed when surface ligands of QDs are replaced by thiolated ones as described in the previous chapter. This was a promising result as the blinking suppressed giant QDs were observed to have invariance of quantum yields regardless of the ligands present on the surface of the nanocrystal,[44] thus indicating low probability of carriers reaching the particle surface.

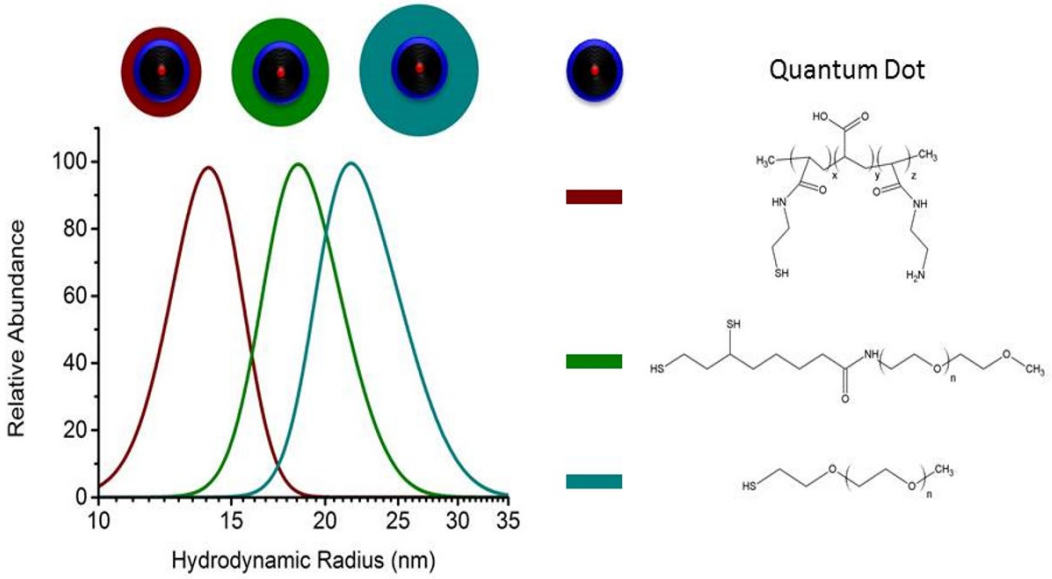

Figure 3.10 DLS of the Step Graded Alloy Shell QDs with Woter Soluble Ligand Coatings. DLS measurements performed on 10 nm CdSe/ $Cd_{(1-x)}Zn_xSe$ QDs made water soluble by a size minimized multidentate polymer (wine), TA-750PEG-OCH3 (olive), and SH-5000PEG-OCH3 (dark cyan) having average hydrodynamic diameters of 14 ± 2.0 nm, 19 ± 3.2 nm, and 22 ± 4.1 nm respectively.

CHAPTER 4

SINGLE MOLECULE FLUORESCENCE SPECTROSCOPY OF QUANTUM DOTS

Single molecule fluorescence spectroscopy is a renowned spectroscopic technique which has been implemented in scientific research for nearly two decades.[225-227] In contrast to traditional ensemble averaged measurements, single molecule methods reveal dynamic and static heterogeneities concealed within ensemble studies. The technique also provides greater insight into the fundamental photophysical processes of the fluorescent species being examined.

Single molecule fluorescence measurements are typically performed with a scanning stage confocal microscope using laser illumination. Here a laser excitation source is focused to a diffraction limited spot (size of half the excitation wavelength) on the sample surface where the resulting fluorescence is collected through the microscope which is then detected by appropriate photon sensors (CCD camera, avalanche photodiode, etc.). If the fluorophores on the sample surface are separated by distances greater than the diffraction limit, only one molecule will be excited at a time. Thus, under these conditions fluorescence is being collected from a lone emitter. Plots of single molecule fluorescence intensity as a function of time (fluorescence intensity trajectories) can then be acquired. When using pulsed lasers combined with time-correlated single photon counting (TCPSC), dynamics on the hundreds of picoseconds to nanoseconds time scale may be obtained.

In this chapter a brief overview of the principle behind TCSPC and experimental set up and conditions will be provided. Then the data obtained from the QDs synthesized with the approach of the previous chapter will be presented.

4.1 The Principle of Time-Correlated Single Photon Counting

Time resolved fluorescence spectroscopy is a powerful analysis tool in studying fluorescent dynamics. Executing it in the time domain necessitates recording the time dependent intensity profile of the fluorescence upon excitation by short pulses of light from a laser. One could try to record the time decay profile of the fluorescence from a single excitation-emission cycle, but there are problems which prevent such a simple measurement. Typical emission from fluorophores lasts only from tenths to tens of nanoseconds. In order to obtain the fluorescence lifetimes along with the decay shape, one must be able to resolve the recorded signal to an extent of the decay being represented by tens of samplings. For example, a lifetime decay of 5 ns needs the transient recorder to sample at 0.5 ns steps.

Sampling at such rapid rates is difficult to accomplish with conventional electronic transient recorders. Furthermore, the signal may consist of just a few photons per excitation-emission cycle and this discrete nature of a weak signal prohibits analog sampling. Even if higher excitation powers are used to gain more fluorescence, there will be limits due to the collection of optical losses, spectral limits of the detector

sensitivity, or photobleaching of the sample. The solution to such recording problems is resolved with time correlated single photon counting. With periodic excitation from a pulsed laser, it is possible to extend the data collection over multiple cycles and one can reconstruct the single cycle decay profile from single photon events collected over many cycles.

Figure 4.1 illustrates how the histogram is formed over multiple cycles and displays an intensity trajectory which is the number of photons counted per integration time. In this example, fluorescence is excited by laser pulses where the time difference between excitation and emission is measured by electronics that act like a stopwatch. If the single photon probability condition is met, there will be no emitted photons at all in many cycles. The existence of a photon or an empty cycle is entirely random and can only be described in terms of probabilities. From the exponential decay present in the histogram of the number of photons detected within each delay time, one can fit a curve to extract the fluorescence lifetime of the sample. On the other hand, one may create an intensity trajectory by choosing a fixed bin time and record the number of photons detected within the interval over a period of several bins.

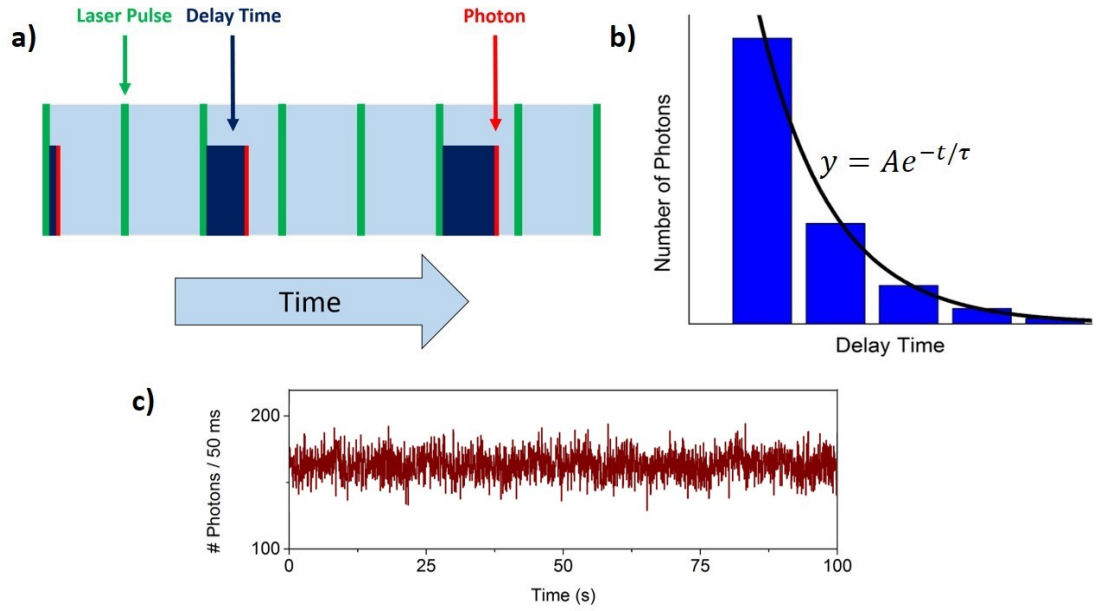

Figure 4.1 Operation and Data Output of a TCSPC Module. **a)** The photon counting module in TCSPC monitors the time interval between excitation from the laser pulse and the detection of an emitted photon from the sample (delay time). The outputs of the TCSPC measurement are the histogram of the delay times **(b)** and the fluorescence intensity trajectory **(c)**. From the histogram of the delay times, the fluorescence lifetime may be obtained from an exponential fit.

4.2 Components of a TCSPC System

Figure 4.2 below displays a block diagram for the major components found in a TCSPC system. Here a brief description of each component will be given.

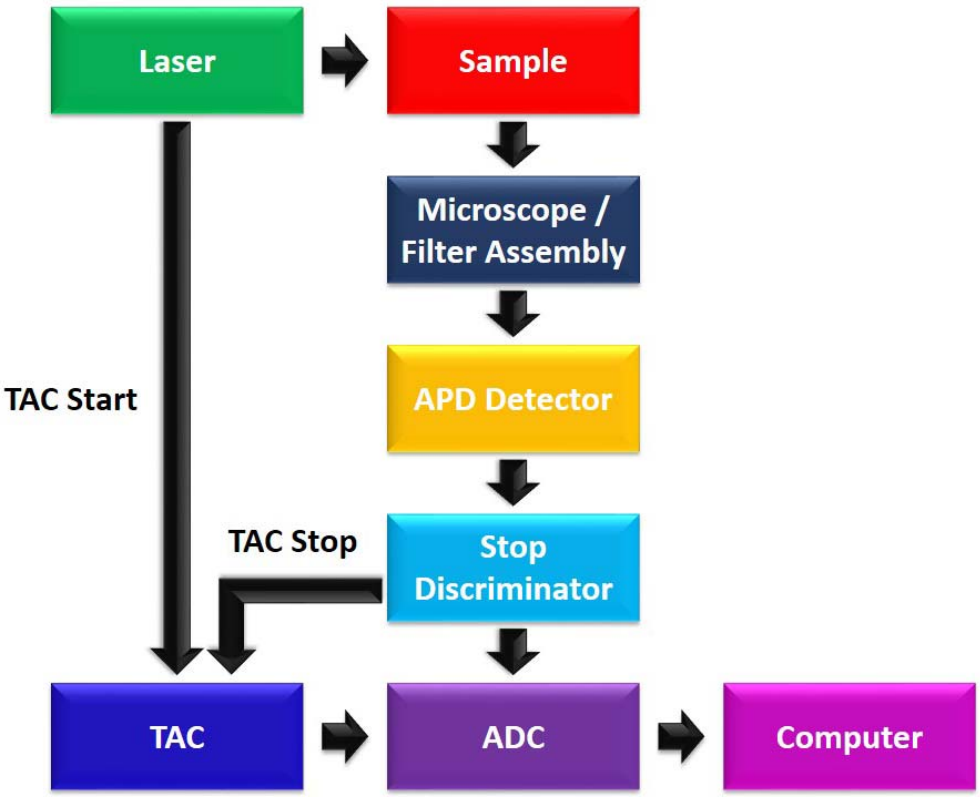

Figure 4.2 Block Diagram of the Components of a TCSPC System.

Laser: The photon source used for the excitation of the fluorescent sample is a pulsed laser. For each pulse, the laser electronics will simultaneously give a 'start' signal to the Time to Amplitude Converter (TAC) which measures the time interval between the excitation pulse and the detected photon before the next excitation pulse.

Detector: Fluorescence from the sample is collected by the microscope and then focused to the detector. In our case the detector used is an Avalanche Photo Diode (APD). APDs may be used for ultra-low light detection of powers less than a picowatt and can be operated as single photon counters in a manner similar to a Geiger counter. In this Geiger mode, the detector can be used for photon counting with precise timing of

the photon arrival. The APD converts these arriving photons into voltage. The output voltage of the APD will include dark noise along with the signal. To filter out this noise the output signal is then sent to the stop discriminator.

Stop Discriminator / Constant Fraction Discriminator (CFD): This unit distinguishes the inputs of the signal from the detector. Here a threshold is set where the noise is cut out by being below this voltage level. This threshold level is determined from the noise level of the APD. There is also a probability that the detector will encounter a signal of more than one photon. This problem can be fixed by setting an upper limit, or maximum allowable voltage. The discriminator will therefore generate a TAC 'stop' signal only if the signal level is above the noise threshold and below the multiple photon limit.

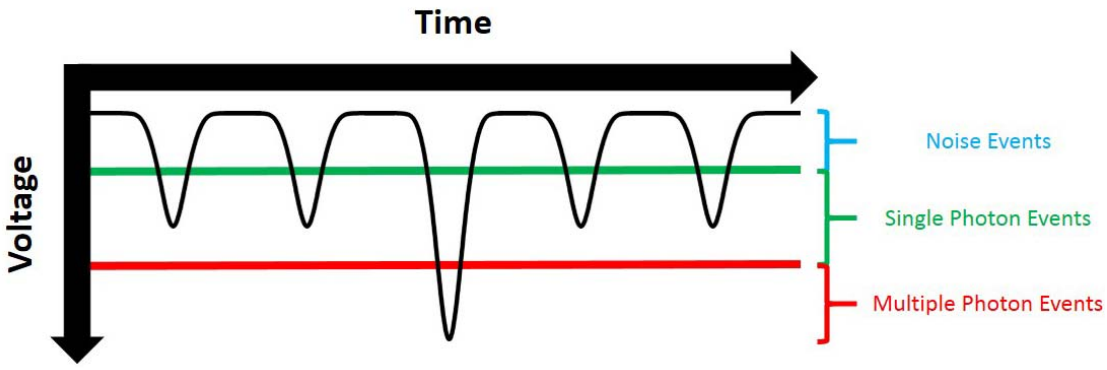

Figure 4.3 Operation of the CFD. The CFD is able to discriminate single photon events from noise and multiphoton events from limits placed on the signal voltage.

Time to Amplitude Converter (TAC): When the TAC obtains the stop signal, it generates an analog output pulse having an amplitude proportional to the time which has elapsed between the 'start' and 'stop' signals.

Analog to Digital Converter (ADC): The ADC measures the amplitude of the pulse from the TAC to decide which of the decay time slots in the histogram of photon counts the particular detected photon is to be recorded in. Repeated excitation and detection cycles develop the delay curve in the histogram as shown in **Figure 4.1**.

4.3 Experimental Set Up for Single Quantum Dot Detection

Single QD detection is performed with a home built system. A diagram showing the layout of the system is presented in **Figure 4.4**. The excitation source is a mode locked Ti:sapphire laser operated between wavelengths of 700-1000 nm at a 82 MHz repetition rate. In order to achieve shorter wavelengths needed for QD absorption, the light is passed through a frequency doubling β-BaB_2O_4 (BBO) crystal to achieve wavelengths of 350-500 nm. The sample dispersed on a microscope slide is placed on a piezo scanning stage where laser illumination is focused to a diffraction-limited spot on the slide through the microscope objective (1.3 NA / 100x oil). A confocal ray path is created from a pinhole in the image plane where only signal from the focal plane is transmitted. Signal from the focal plane is then collected through the same objective and focused to the APD with the photon counting being accomplished by the TSCPC module.

Single QDs on the slide are located through point by point scanning of the laser beam across the sample via the piezo scanner. **Figure 4.5 (a)** shows an example of a

raster scanned fluorescence image of isolated QDs. Each peak in the image indicates a single particle. In addition, single QDs may be verified using an AFM which rests on top of the sample stage and an example scan is presented in **Figure 4.5 (b)**. It should be noted that the lateral dimensions in these images do not correspond to the true lateral dimensions of the QD. The QD sizes are much less than the diffraction limit in the laser raster scans, and for the AFM, convolution between the sample tip and particle widens the observed dimensions. In addition the sample may move with the AFM tip as it is being scanned across the sample.

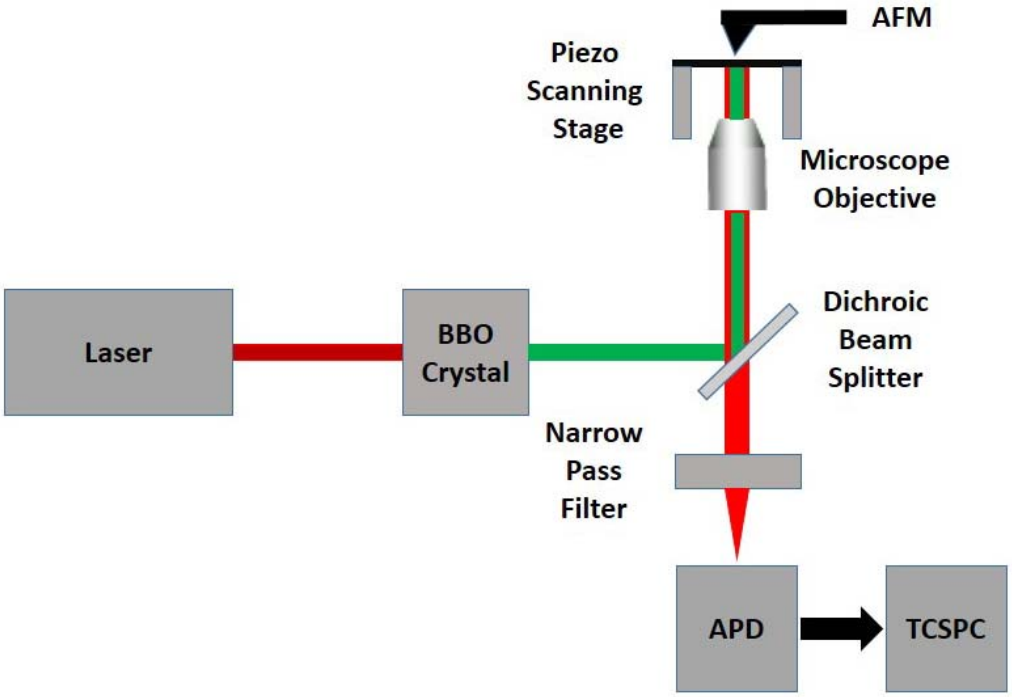

Figure 4.4 Apparatus Schematic for Single QD Fluorescence Measurements. Simplified schematic of the apparatus used for single QD fluorescence detection.

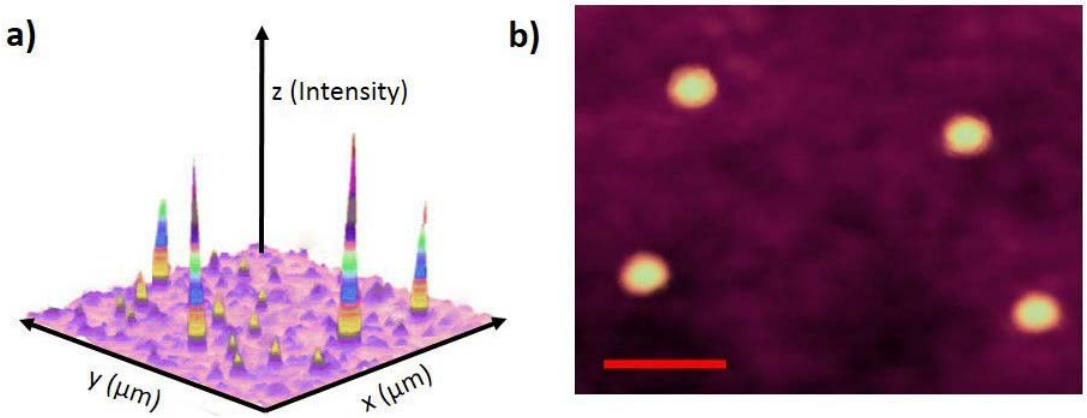

Figure 4.5 Raster Fluorescence and AFM Scans of Single QDs Resting on a Glass Slide. a) Sample of a raster scan of QDs on a microscope slide. **b)** Sample of an AFM scan of QDs on a microscope slide (scale bar 200 nm).

4.4 Gradient Alloy Shell QD Fluorescence Measurements

4.4.1 Sample Preparation

Glass microscope slides were first rinsed with propanol, dried in air, and then swiftly skimmed over a flame to remove any adsorbed organic compounds prior to use. QD solutions diluted to concentrations less than 10 pM were then spin coated onto the slides. Low concentrations are necessary to ensure well separated (beyond diffraction limit) single QDs. For ensemble measurements, such as the bulk fluorescent lifetime, the QD solution was spin coated at concentrations of ~ 100 pM. The diluting solvents were hexane or methanol for QDs which were soluble in organic or aqueous media respectively. Quick drying solvents are chosen for better particle separation in the spin coating process and for less drying time before fluorescent measurements.

4.4.2 Finding and Inspecting a Single QD

The QD coated cover slips are raster scanned to generate a fluorescence map as discussed in the previous section. Once the map is developed, the stage is then moved to the point of maximum fluorescence of the emitter. At this point, the fluorescence trajectory is collected and binned at 50 ms. Typical fluorescence collection times for each QD inspected exceeds 10 minutes to ensure sufficient data for the statistical analysis of blinking. After the fluorescence data has been retrieved, an area spanning 1 μm^2 is scanned with an AFM to rule out if data was obtained from QD clusters instead of single emitters.

4.4.3 Determination of On/Off Thresholds and Probability Densities

The threshold determining on and off states is set by the maximum intensity that is obtained from illuminating the sample in a region with no QDs. As seen in **Figure 4.6** below, the on (off) time is the interval where the signal intensity remains above (below) the threshold. These time periods are then binned on a logarithmic scale ranging from 0.1 to 1000 s. A histogram is then developed with the number of events in the intensity trace that fall into the corresponding on or off time bin. The probability distribution of this histogram is given by the following:

$$P(\tau) = \frac{\sum events\ of\ time\ \tau}{\sum all\ events} \tag{4.1}$$

where τ refers to the duration of the on or off event. As described in the previous chapter, these distributions fit nicely into a power law distribution of the form below.

$$P(\tau) = A\tau^{-m} \tag{4.2}$$

Though the power law behavior seems universal in QD blinking statistics,[177] it should be noted that the fits to the power law distribution are dominated by the short duration events and that deviations may occur at longer times.

4.4.4 Comparison in Blinking Behavior of Cores and Graded Alloy Shell QDs

The 2 nm CdSe starting cores and the cores coated with the 14 monolayer $Cd_{(1-x)}Zn_xSe$ linear gradient shell, whose syntheses were described in **Chapter 3**, were compared in terms of fluorescence intermittency. As can be seen in **Figure 4.6**, there is a drastic change in the on/off durations between the two samples. The 2 nm starting cores without a passivating shell spend most of the illumination time in the off state with few brief on states, whereas when encompassed by the linear gradient alloy shell spend most of the time in the on state with few short off states.

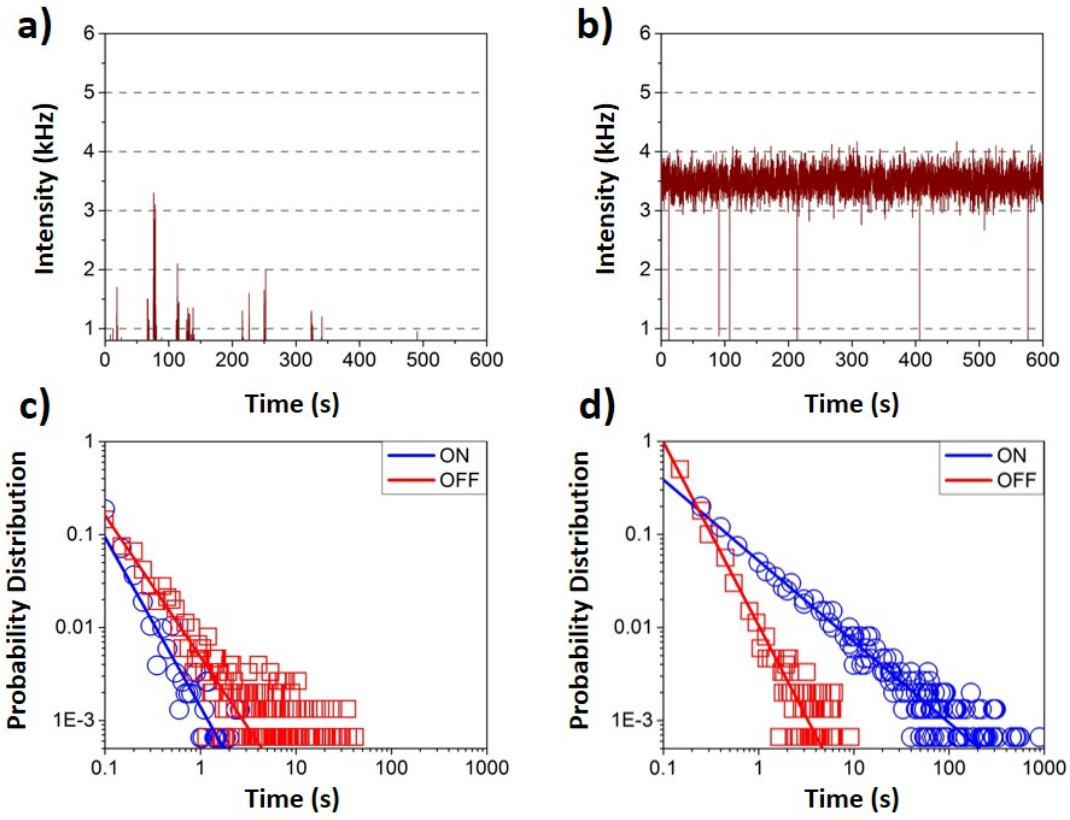

Figure 4.6 Dynamic Fluorescent Traces and On/Off State Probability Distributions for the Small Starting CdSe Cores and the Blinking Suppressed Step Graded Alloy Shell QDs. Dynamic fluorescent traces of a 2 nm CdSe core **(a)** and the 2 nm core with the linear step graded alloy shell QD **(b)** along with the on/off time probability distributions for the cores **(c)** and graded shell particles **(d)**.

The on power parameter for the graded shell particles which produced the best fit was $m_{on} =$ 0.87, while the off parameter m_{off} = 1.97. For the CdSe cores, the on and off probability parameters were m_{on} = 1.83 and m_{off} = 1.52. The smaller parameter values for the on distributions and larger values of the off distributions for the graded shell particles indicate increased probability of on events and decreased probability of off events. Similar changes encountered in power law parameters from the on and off distributions for traditional core and core/shell particles[228] have been observed when blinking suppression is achieved.[49,229] Of 100 particles inspected for the graded alloyed

shell QDs, high fractions of the population exhibited great suppression of blinking, where almost a quarter of the population exhibited > 99 % on times with an ensemble average of 92.6 ± 8.1 %. In addition, the infrequent off times were of short durations typically being less than 200 ms.

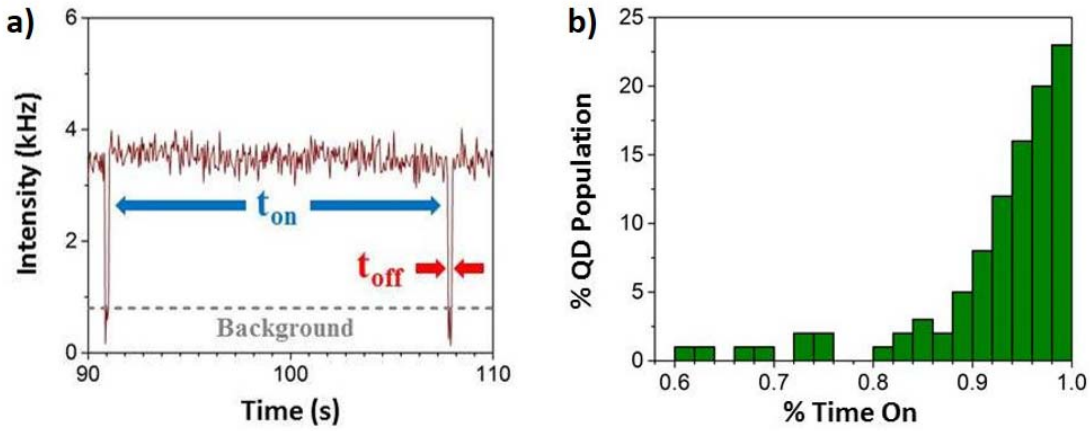

Figure 4.7 Close up of a Dynamic Trace and Distribution of On Time Percentages. **a)** Close up of the intensity trace of the gradient alloy shell QD showing the short duration of the off events and long duration of the on events. **b)** Histogram of the percent on times of 600 s traces of 100 gradient alloy shell particles inspected.

After each 600 s dynamic intensity trace recording, the region was inspected by an AFM to ensure that the data obtained came from a single QD. If particles were found to be dispersed at greater distances than the diffraction limit, the data was accepted. If particles were closer, then the data is rejected. **Figure 4.8** shown below presents an example of such an AFM trace which was performed on a sample of gradient alloy shell QDs with multidentate polymer encapsulation. Though the lateral resolution being poor in the AFM from tip-sample convolution, height resolution is quite high (< 1 nm). The multidentate coated blinking suppressed particles for example show 12 nm height which is near the 14 nm measured by DLS. The loss of a few nm in size can be due to the

drying (polymer collapse) of the particles. The importance is that, under the AFM trace, only a single hump is obtained indicating a single particle. In addition, despite the perceived greater lateral dimensions of the nanoparticles under such AFM traces, the accepted data is still required a separation distance greater than the diffraction limit.

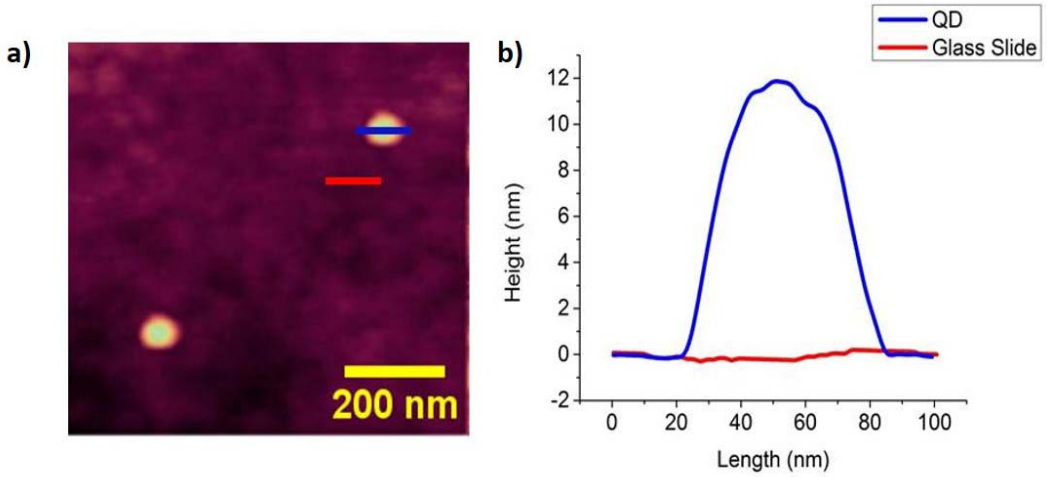

Figure 4.8 AFM Scanning of Single QDs. a) AFM image of a region in which a dynamic intensity trace was recorded. **b)** AFM line scans of a single QD along with the background of the glass slide.

4.4.5 Fluorescent Lifetimes

Fluorescent lifetimes of the graded shell QDs and 2 nm CdSe starting cores with 2 monolayers of ZnS shell material were compared. The CdSe/ZnS particles displaying multiexponential behavior, (34 % 1.8 ns, 56 % 10.2 ns, 10 % 22 ns) the characteristic lifetime (t_C)

$$t_C = \frac{\sum P_i \times t_i^2}{\sum P_i \times t_i} \tag{4.3}$$

was calculated to be 12.6 ns. Similarly, the graded shells with a more monoexponential behavior (11 % 2.1 ns, 89 % 24.3 ns) results in a characteristic lifetime of 24.0 ns which is only a 1.3 % difference from the dominant component. Lifetimes were fit with chi squared values less than 1.2 ($\chi^2 < 1.2$) using the FAST software from Edinburgh Instruments.

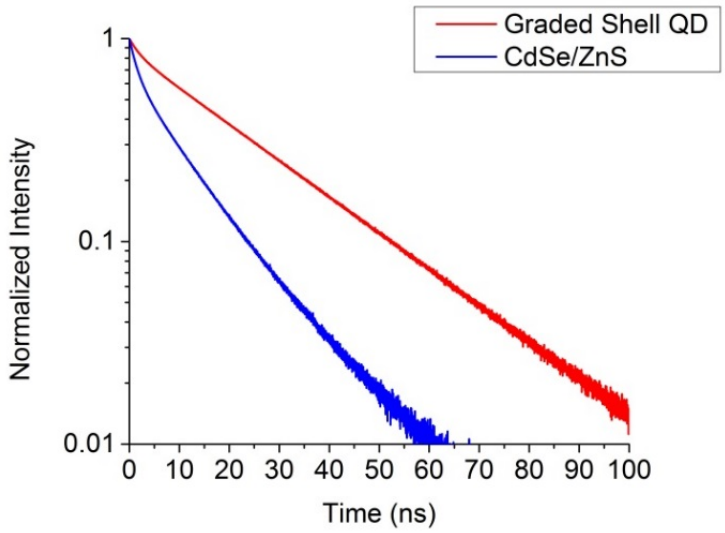

Figure 4.9 Fluorescent Lifetimes of QDs. Fluorescent lifetimes of the graded shell QDs compared to cores of similar size with 2 monolayers of ZnS (24.3 ns and 10.2 ns respectively).

In the study by Fisher et al. of fluorescence lifetimes of traditional CdSe/ZnS QDs, they found that if the fluorescence lifetime is only measured for times where the single QD fluorescence exceeds the on state threshold, the single and extrapolated ensemble lifetimes will exhibit monoexponential behavior.[230] As dark and grey states were introduced into the ensemble lifetime measurement, the multiexponential behavior became present.[230] Such multiexponential behavior is attributed to nonuniform

fluctuations in the nonradiative rates present among the individual particles. It was determined that the radiative rates were rather uniform if the dynamic traces were recorded in the periods above the on state threshold.[230] Thus, monoexponential decay in the fluorescent lifetime can be indication of blinking suppressed samples. Indeed, other studies have observed blinking suppressed particles having a vast majority of the emission time spent above the on state threshold exhibit monoexponetial decays without preferential period selections in the time traces.[48,49]

4.4.6 Blinking Suppression Maintained with Aqueous Solubilization

The three aqueous stabilization strategies carried out for the gradient alloy QDs were also compared in blinking behavior. Surprisingly, the optical properties were invariant to the ligands on the surface of the nanoparticles. The frequency and durations of the off times were left unchanged just as the QY observed in **Chapter 3**.

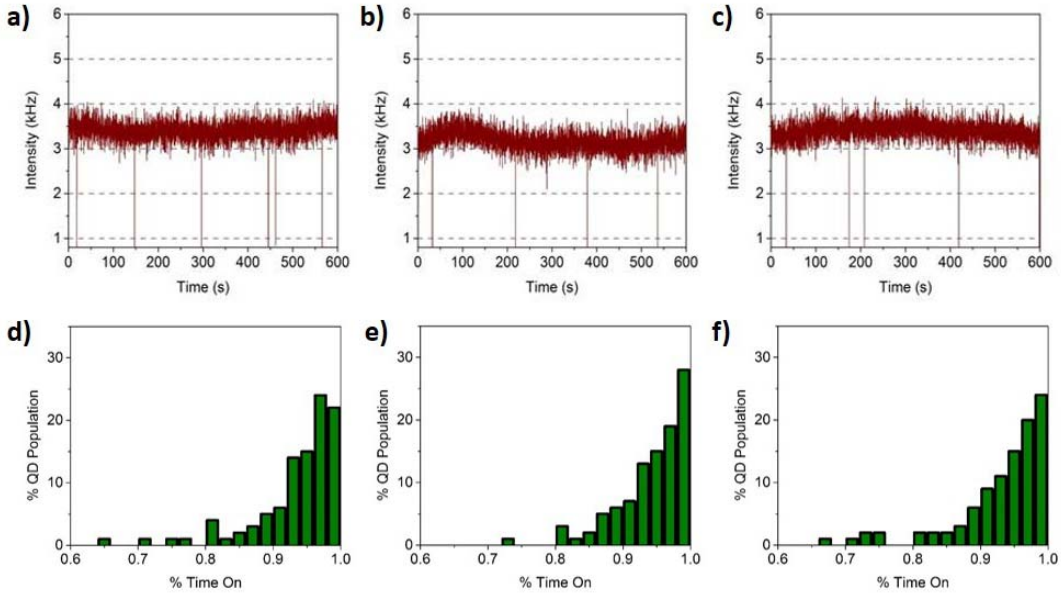

Figure 4.10 Dynamic Fluorescent Traces and % On Distributions of Blinking Suppressed QDs with Different Aqueous Soluble Ligand Coatings. Dynamic intensity traces of the blinking suppressed gradient alloy shell QDs with aqueous solvating ligands of the minimized multidentate polymer **(a)**, TA-750PEG-OCH3 **(b)**, and SH-5000PEG-OCH3 **(c)**; along with their corresponding on time percentage histograms of 100 particles inspected for 600 s each (**d**, **e**, **f**, respectively).

To date this is the first study to show QDs which are able to preserve the optical properties of QY and blinking suppression under aqueous transfer using a variety of ligand thicknesses (2-6 nm) and anchoring moieties chosen (thiols, bidentate thiols, and amines). The distributions for the ensemble on time percentages were maintained with the original hexane solution being 92.6 ± 8.1 % and the aqueous solutions having coatings of the multidentate polymer, TA-750PEG-OCH3, and SH-5000PEG-OCH3 being 93.1 ± 6.9 % , 94.2 ± 5.1 % , 93.5 ± 6.4 % respectively. These results show promising application to biological single molecule imaging where dynamical information can be obtained at high acquisition rates without significant loss of signal

over extended periods of time along with allowing any ligand functionalization strategy without compromising the enhanced optical properties.

CHAPTER 5

CELLULAR STUDY OF SINGLE QUANTUM DOT TRACKING

Single particle tracking using gold particles,[231] quantum dots,[232] or fluorescent dyes and proteins[233] as detectable probes permits the reconstruction of single molecular trajectories with nanometer precision. As a result, tracking of single molecules can reveal comprehensive information on the molecule's lateral dynamics. In addition, through inference of the observed motion, one can extract features of the immediate surroundings of the molecule.[234] Due to the detailed dynamic information single particle imaging offers, it has become a valuable experimental technique which has found abundant use within biological studies over the last few decades.[233,235,236] The method has specifically been paramount in investigations of the spatial organization of the plasma membrane.[50,237-240] A majority of these studies have revealed that the motion of single molecules in the plasma membrane is diverse in types of detected motions consisting of: Brownian diffusion, confined diffusion, directed diffusion, and various combinations of these motions.[51,237,241,242] These studies have contributed to the current knowledge of the plasma membrane structure as highly complex and heterogeneous.[243]

However, there are experimental concerns in single particle tracking, most of which are solely associated with the choice of probe.[244] For example, labels such as fluorescent dyes and proteins are preferred for their small size and simplicity in the production of monovalent probes, but suffer from very limited temporal sampling frequencies and short durations for observation due to rapid photobleaching. In contrast,

larger labels such as gold particles that are preferred for their photostability and brightness, which enables extreme sampling frequencies at rates up to 50 kHz for long durations, suffer from increased drag forces leading to slower observed diffusion rates. Furthermore, the analysis methods are strongly influenced by the choice of labels because the duration of the observations in the case of smaller probes, such as fluorescent dyes and proteins, are restricted to only a few frames with signal before photobleaching which prohibits single molecule trajectory analysis.[233] QDs, on the contrary, have greater photostability than organic dyes and proteins allowing trajectory construction while being smaller than gold particles which lessens perturbations to the natural diffusion of the tagged molecules. One of the major limitations of QDs as single molecule tracking probes, however, was blinking. The off periods found in commercially available QDs were observed up to durations of 100 seconds[28], which consequently leads to numerous frames without a signal leaving similar limitations on trajectory analysis as organic fluorophores. Thus, with blinking suppressed quantum dots one gets the benefits of full photostability with the smaller probe sizes for enhanced data quality in single molecule imaging.

In this chapter the wide field illumination apparatus will be explained, developing the bioconjugation for the blinking suppressed probes, preparation of the cells and imaging conditions of the single particle tracking experiments, and the benefits of the blinking suppressed probes will be shown compared to commercially available QDs.

5.1 Wide Field Microscopy Apparatus

Possibly the easiest method to image the fluorescence from single emitters is to use wide-field microscopy. Here a mercury lamp is used to illuminate an area of microns in diameter similar to that of a traditional light microscope. Filtering is used to remove the excitation wavelengths from the light collected from the objective and to pass the sample fluorescence to a CCD. Performing single molecule imaging in this manner has two main advantages: many individual fluorophores can be observed concurrently, and the position of the fluorophores can be obtained at high video rates allowing the observation of translation of the emitters in real time. The main drawback of wide-field microscopy methods is that the maximum frame acquisition rates for CCD cameras is slower than the response time for single element detectors such as an APD which was used in the fluorescence spectroscopy measurements in the previous chapter. Though for experiments requiring a maximum temporal resolution in the tens of milliseconds, wide-field methods are adequate for single molecule tracking experiments. For example, a typical CCD frame rate of 33 Hz has a temporal resolution near 30 ms.

Despite a large region of the sample being imaged onto the detector, the spatial resolution of wide-field microscopy will be diffraction limited. Even with high numerical aperture (*NA*) optics, single emitters will be viewed as spots on the CCD with diameters nearing 300 nm. However, with an adequate signal to noise ratio, it is possible to determine the location of the emitter's location better than the diffraction limit. The accuracy with which the position can be determined is controlled by the size of the CCD

pixels and the overall magnification of the microscope. For the microscope used in this study, a CCD camera with 16 micron pixels mounted on a microscope with a 100x objective, 1.5x auxiliary amplifier, and a 10x beam expander (giving a 1500x total microscope magnification), a wide-field image would display a single molecule as a spot having around 30 pixels in diameter. The position of the center of this spot can easily be known to the nearest pixel, or 10.6 nm in this case. This location determination is through fitting the illuminated pixels to a Gaussian profile to find the center of emission. In principle, unlimited spatial resolution could be attained (for a single spot only; the limitations on the capability to resolve two spots still apply unless different colors are used to differentiate overlapping spots[245]) by dispersing the image over a greater number of CCD pixels. This could be done through the use of a CCD with smaller pixels, or by increasing the magnification. However, there are issues preventing such limitless spatial resolution: Photobleaching or prolonged nonemissive states will limit the total number of detected photons which prevents the sufficient signal to noise ratio needed. Though blinking suppressed QDs are devoid of these problems, however, CCD cameras will have read out noise which limits the amount to which the emitted photons can be spread over detector pixels.

For all single molecule tracking experiments, the *NA* is also a vital parameter.

$$NA = n\sin\left(\theta_{\max}\right) , \tag{5.1}$$

where n is the refractive index of the medium between the sample and the objective and θ_{max} is the maximum collection angle of the objective. In order to maximize the detected light, the *NA* should be as high as possible. This is typically done by using an objective intended to be immersed in a high refractive index medium such as oil. For imaging single emitters, an oil immersion (n = 1.51) objective is favored, and such objectives have a *NA* as high as 1.4. The flatness of field for the microscope objective also has a substantial bearing on wide field imaging applications, particularly if distance parameters across the image need to be precisely measured. Objectives which are designated as PlanApo are designed with the highest flatness of field and color correction, and are used for all wide-field imaging in this study.

The wide absorbance envelope and absorption cross section of QDs enables great flexibility on the excitation source used in the wide field apparatus. The QD absorption of light energy does increase at shorter wavelengths (350–400 nm), though this may lead to increased cellular autofluorescence and also be damaging to the live cells being imaged. Generally an improved signal to noise ratio (SNR) is attained using excitation wavelengths in the region of 530–580 nm along with minimizing light induced cellular damage. For fluorescence detection, QDs emitting in the red region (600–700 nm) is preferred as it is in a spectral region where the cellular autofluorescence minimal. For common CCD cameras employed in fluorescence imaging it is recommended not going beyond 700 nm in QD detection as at these wavelengths the quantum efficiency of the detector drops precipitously leading to poor SNR.

5.2 Quantum Dot Bioconjugation for Membrane Receptor Tracking

Commercially available bioconjugation cross-linkers have been regularly used to activate nanoparticles for biological applications. Among these agents, 1-ethyl- 3-(3-dimethylaminoprophyl)carbodiimide hydrochloride (EDC) has been widely used to prepare antibody-conjugated nanoparticles. Though this method has observed success in QD-conjugate structure development, aggregation is a common problem with this technique. In addition, using zero length crosslinking agents such as EDC may leave too great of steric hindrance between the PEG molecules and the antibody leading to reduced target binding affinity.[246] Therefore, the coupling strategy of using sulfo-LC-SPDP and sulfo-SMCC was chosen to avoid these issues for the QD-antibody (QD-Ab) conjugates to be used for tracking studies.

The method for coupling the antibody to the blinking suppressed QDs is as follows (**Figure 5.1**): First, sulfo-LC-SPDP was reacted with QDs having solvating ligands of DHLA-PEG3400-NH_2 (Nanocs) at room temperature for 1 hour at a ratio of 10,000 linkers per QD. Once the reaction is complete, the disulfide bond of the linker is reduced through adding an excess of DTT. The resulting QDs, presenting thiol end groups, were then purified with a desalting column equilibrated with phosphate buffered saline to remove unreacted sulfo-LC-SPDP along with DTT. In a separate vial, to introduce thiol reactive groups of maleimido to the antibody, the amine groups of anti-EGFR (Invitrogen 31G7) were activated by reacting with sulfo-SMCC at a ratio of 10 linking agents to 1 antibody. Excess SMCC linker was removed by membrane filtration

(MWCO 30 kDa). Finally, the maleimido functionalized anti-EGFR was reacted with the surface thiol groups of the QDs in a 1.2:1 molar ratio for 3 hours in phosphate buffered saline under vigorous mixing. The subsequent QD-Ab conjugates were purified through size exclusion column chromatography using Superdex 200 equilibrated with phosphate buffered saline.

QD multivalency is a serious concern in single molecule tracking studies, as cross-linking of surface proteins can trigger signaling pathways and radically decrease the targeted receptor mobility.[231] Numerous methods have been utilized by researchers in order to maximize the content of monovalent probes within the sample. One tactic in preparing monovalent nanoparticles exploited the low density of functional sites on the surface resulting in near 70 % monovalency of the sample.[247,248] Another method tried nickel affinity separation, however there was overlap amongst the monovalent and multivalent particles.[249] Nanoparticles have also been separated according to the number of DNA strands attached,[250] though this method has substantial increases in the hydrodynamic diameter and promotes nonspecific binding to cells.

The low stoichiometric ratio method applied here is in hopes that most particles will have one antibody with very few having two. This method has been applied successively for QD single molecule tracking previously,[164] but it is understood that the stochastic nature of the conjugation reaction can leave a distribution on the number and geometric orientation of antibodies present on the surface of the particles. The valencey among the sample using this method generally follows a Poisson distribution[251]

$$P(N,n) = \frac{N^n e^{-N}}{n!}, \tag{5.2}$$

where N is the stoichiometric ratio (also the mean of the distribution) applied between the affinity molecules to the QDs and n is the resulting number of affinity molecules found on the QD. According to this distribution, the sample fractions displaying 0 or 1 affinity molecules will be 30 % and 36 % respectively. This leaves the remaining 34 % at higher valences which may adopt geometrical configurations to bind more than one cell surface target. Thus this method cannot rule out possibilities of multivalent binding in the single molecule tracking experiments, however, the following results are still able to illustrate the benefits of the blinking suppressed probes opposed to traditional core/shell particles in this proof of concept study.

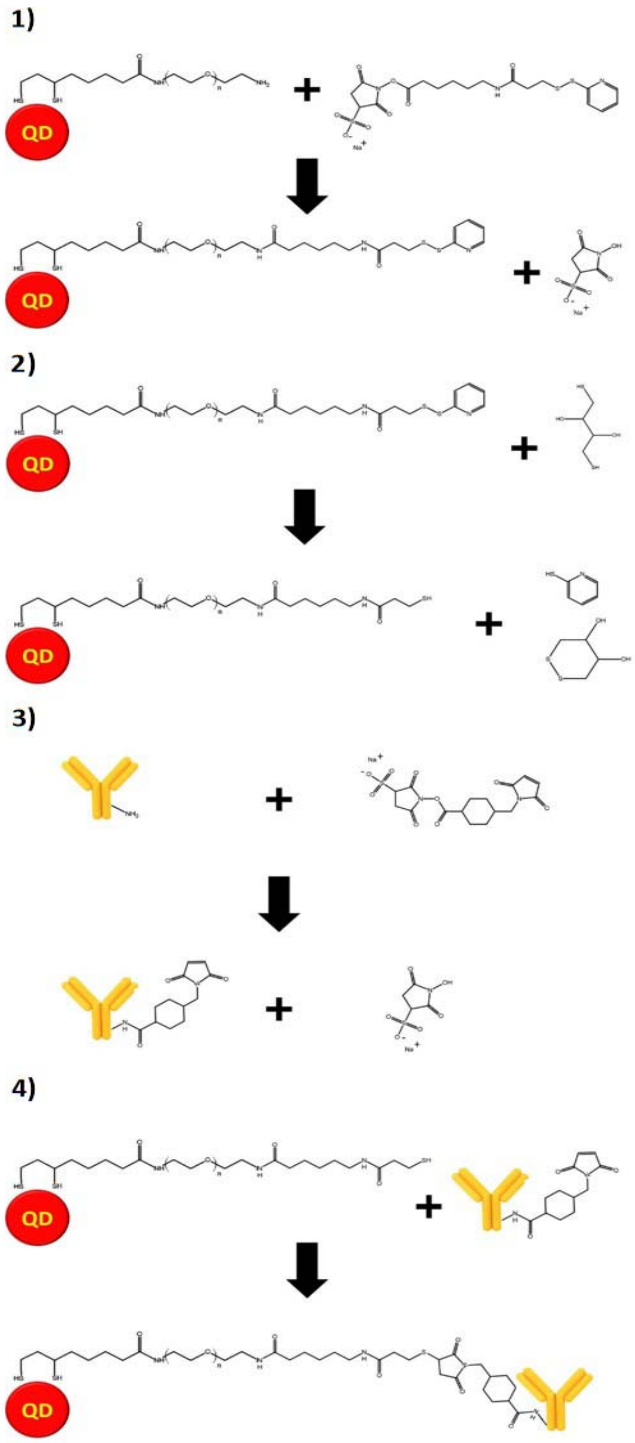

Figure 5.1 Procedure for Functionalizing QDs with Antibodies. 1) DHLA-PEG3400-Amine coated QDs are activated with sulfo-LC-SPDP. **2)** The disulfide of this cross linker reagent is then reduced with DTT. **3)** In a separate solution the antibody is activated by sulfo-SMCC. **4)** Upon mixing 2 and 3, the QD-Ab conjugates were produced.

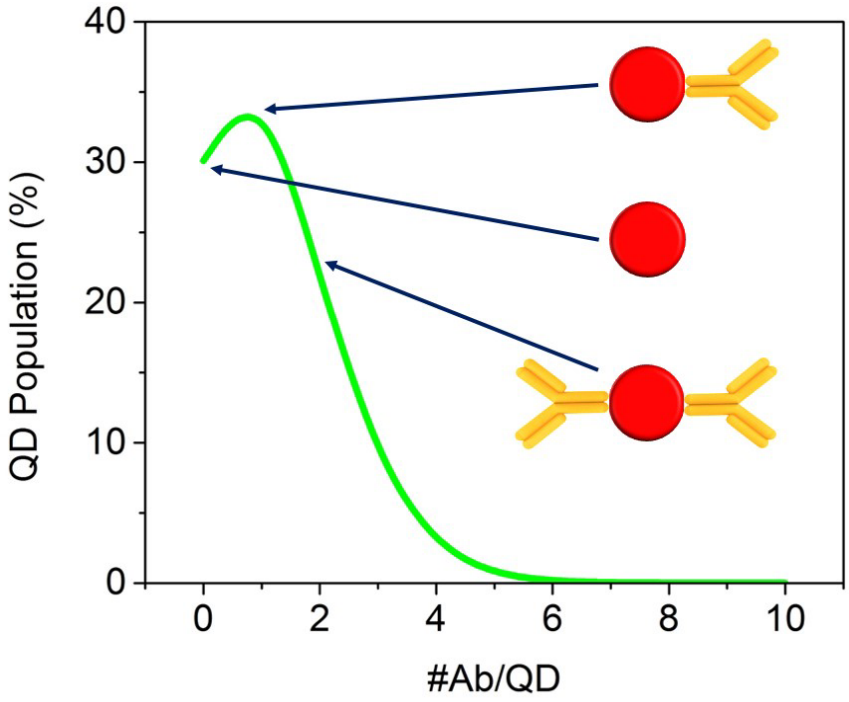

Figure 5.2 Poisson Distribution of the Number of Attached Antibodies per QD. Poisson distribution showing the resulting percentages of the sample having varying antibodies bound to the surface using a stoichiometric ratio of 1.2 antibodies per QD.

5.3 Cell Culture and Imaging Conditions

The human lung carcinoma cell line A549, which overexpresses EGFR, was grown on coverslips and imaged in medium containing 10 mM HBSS, 10 mM HEPES, and 5 % FBS, pH 7.4. For labeling, cells were first washed with PBS, then incubated at 4 °C for 30 minutes in 1 % BSA in PBS and for 1 hour with the QD-Ab conjugates in picomolar quantities. Unbound QDs were removed through washings of PBS. The coverslip is then mounted on the microscope chamber at room temperature. A region of interest is then selected based on the bright field image of the cell. Once this region is

chosen the fluorescence image is then taken to observe the QDs present in the area. Once a well isolated QD has been spotted, real time fluorescence image recording is performed at 33 frames per second. The total duration of an imaging experiment does not exceed 15 minutes to ensure cell viability when tracking the surface receptors.

5.4 Tracking and Data Analysis

The tracking analysis applied to the stack of frames gathered from a single QD experiment consists of two main steps applied successively to each frame within the sequence. In the first step, fluorescent spots in each frame are cross correlated and QD centers are determined using a Gaussian model of the point spread function (PSF). Here a least-squares fit is applied to determine the spatial accuracy of the center of each fluorescent spot to 10 nm or less. Next, the QD trajectories are linked from frame to frame using the centers of the fluorescent spots detected.

For the data analysis of the QD diffusion, paths were time-averaged by computing the mean squared displacements (*MSD*) for each single trajectory, *m*. The trajectories were analyzed for time intervals, nt_{lag} = 15 min, with *n* being the image frame number, and t_{lag} being the time between successive image frames (t_{lag} = 30 ms). The *MSD* for an image stack of *N* frames was calculated by the following equation.[252]

$$MSD_m\left(nt_{lag}\right)=\frac{1}{N-n}\sum_{i=1}^{N-n}\left[\left(x_m\left(\left(i+n\right)t_{lag}\right)-x_m\left(it_{lag}\right)\right)^2+\left(y_m\left(\left(i+n\right)t_{lag}\right)-y_m\left(it_{lag}\right)\right)^2\right] \tag{5.3}$$

Afterwards curve fitting was applied to the *MSD* curves to two basic diffusion models:

a) Brownian diffusion with a single diffusion constant D_{free} where c is a constant related to the spatial localization accuracy.[233]

$$MSD_{free}\left(nt_{lag}\right)=4D_{free}nt_{lag}+c \tag{5.4}$$

b) Diffusion confined within a limited area L^2 with a short-term diffusion constant D_{conf}.[242,252]

$$MSD_{conf}\left(nt_{lag}\right)=\frac{L^2}{3}\left(1-\exp\left(-\frac{12D_{conf}nt_{lag}}{L^2}\right)\right)+c \tag{5.5}$$

From the values obtained in the above equation one can extract $\tau_{barrier}$, the time it takes for the QD to experience the effect of the barrier confinement with the following equation.

$$\tau_{barrier} = \frac{L^2}{12D_{conf}} \tag{5.6}$$

Another commonly observed behavior in cellular single molecule tracking is directed diffusion which has the form

$$MSD\left(nt_{lag}\right) = 4Dnt_{lag} + \left(Vnt_{lag}\right)^2, \tag{5.7}$$

where V is the velocity of the entity (e.g. endosome) directing the particle motion.[231] This model is excluded as such directed motions were not observed in this study. The appropriateness of which model to choose between those of 5.3, 5.4, or 5.6 can be known from inspection of the plot of the *MSD* with time. A linear plot would indicate more Brownian like behavior whereas superlinear or sublinear plots would indicate directed or confined motion respectively.

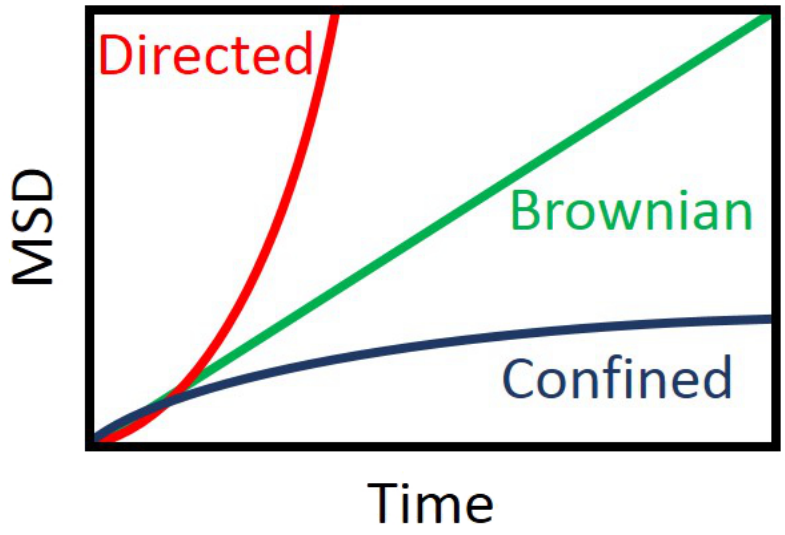

Figure 5.3 MSD as a Function of Time for Different Types of Diffusion. The differences between directed, Brownian, and confined diffusional behavior can be observed by plotting the MSD with time.

There are also several other diffusion models found in the literature for fitting *MSD* curves. These include anomalous diffusion, $MSD\left(nt_{lag}\right) = 4D_{free}nt_{lag}^{\alpha}$, where $0 < \alpha \leq 1$ ($\alpha = 1$ corresponds to free diffusion)[233,253] but α has no physical significance. In addition, a model for hop diffusion, which comprises an infinite sum of components, has been derived by Powles et al.[254] In this study, however, the simpler models for diffusion described above were adopted for a more straight forward and understandable description of the dynamics.

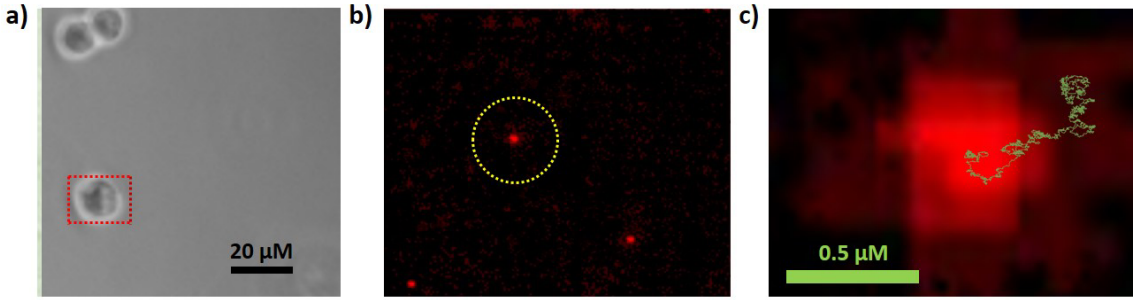

Figure 5.4 Imaging Process of Tracking Single QDs Adhered to Cellular Membranes. First, a cell is located using the bright-field mode of the microscope (**a**). Then the microscope is switched to fluorescence imaging mode where an isolated QD is chosen for tracking (**b**). A trajectory is then developed by linking the centers of the PSF of the fluorescent spot from a 60 s image stack of frames taken at 33 Hz (**c**).

5.5 Single QD Tracking of EGFR Results

Traditional core shell structure QDs (TQDs) composed of CdSe/CdS/ZnS were compared to the blinking suppressed gradient alloy shell CdSe/$Cd_{(1-x)}Zn_xSe$/ZnSe particles (BSQDs), where the sample emission is 630 nm and 620 nm respectively. The samples were excited at 560 nm with a 40 nm bandwidth where sample fluorescence was separated with a 610 nm long pass filter. Both samples were biofunctionalized and applied to A549 cells according to the methods described earlier in the chapter. The notable differences between the two probes are that the gradient alloy QDs are 5 nm larger in diameter (HD_{TQD}=26±5.8nm, HD_{BSQD}=31±6.4nm), the TQDs have a higher quantum yield of 65 % (BSQD has 50 % quantum yield), and the TQDs have easily noticeable blinking whereas the gradient alloy QDs do not when observed in the fluorescent microscope.

For both QD samples, during the initial minutes (< 3 min) of tracking, the MSD showed a linear relationship with time. After this period the diffusion was found to decrease showing a plateau in the MSD v. time plot. This plateau indicates that the diffusion of the particles is being confined to a localized region within the membrane. The switching of initial Brownian diffusion to confined diffusion behavior is commonly seen in single particle tracking studies.[31,252] Such decreases in the diffusional motion are attributed to the particles being confined into compartmentalized lipid rafts within the cellular membrane.[237,255,256]

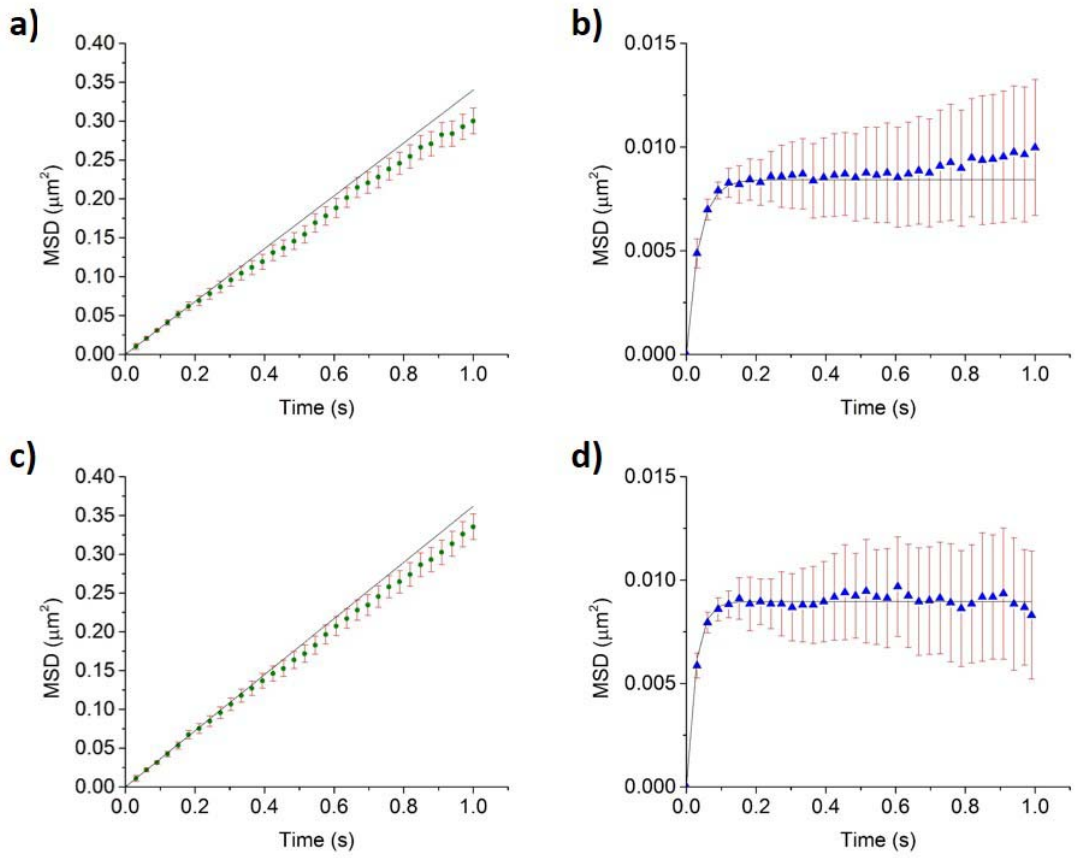

Figure 5.5 MSD Plots of Brownian and Confined Cellular Membrane Diffusion of QDs. MSD v. time plots for the blinking suppressed QDs in a Brownian diffusion period where the extracted linear fit diffusion coefficient is 0.085 μm2/s (a), blinking suppressed QDs in a confined diffusion period where the diffusion coefficient is 0.065 μm2/s and the confinement length is 159 nm (b), traditional core/shell QD in a Brownian diffusion period with diffusion coefficient of 0.091 μm2/s (c), and traditional QD in a confined diffusion period with diffusion coefficient of 0.087 μm2/s and confinement length of 164 nm (d).

There are little differences observed in the diffusional behavior of the BSQDs and TQDs despite the BSQDs displaying a slightly larger hydrodynamic diameter. For the Brownian regime, the free diffusion coefficients were found to be 0.085 $\mu m^2/s$ and 0.091 $\mu m^2/s$ for the BSQDs and TQDs respectively. The confinement diffusion coefficients and lengths were also similar being 0.065 $\mu m^2/s$ and 159 nm for the BSQD and 0.087 $\mu m^2/s$ and 164 nm for the TQD. Similar diffusion coefficients and

confinement sizes have been observed in previous membrane receptor tracking experiments using QD probes.[257] In addition, the confinement lengths are within the range of determined sizes of lipid rafts of cellular membranes (10-200 nm).[258]

It is deemed in the observed initial stages of Brownian diffusion of the particles are not freely diffusing in the membrane. If one considers the Stokes-Einstein Equation for diffusing spheres

$$D = \frac{k_B T}{6\pi\eta R} \ , \tag{5.8}$$

where k_B is the Boltzmann constant, T is temperature, η is the viscosity of the solvent, and R is the hydrodynamic radius of the particle, it is determined that an unbound 31 nm QD would have an observed diffusion coefficient of 0.14 $\mu m^2/s$ with a typical membrane viscosity of 100 cP[259] at room temperature. This value is 1.65 times that of the value observed in the tracking experiments. The slower observed diffusion coefficients are indicative of the QD interacting with cellular components which increase the drag in its motions. In addition, motion is not believed to occur from endosomal trafficking as directed kinesin and dynesin movements typically have velocities around 1 $\mu m/s$[260] and show superlinear MSD v. time plots.

Significant differences, however, were observed for the single particle trajectories during frame correlation. As can be seen in **Figure 5.6**, a TQD during an off

state traveled a distance near 250 nm before reappearing more than 20 frames later. During the faster diffusion regimes in the initial stages of the imaging experiment, most TQDs inspected have significant regions where there is no signal to reconstruct the trace whereas the BSQDs had no such problem. It is deemed that signal disappearances of the TQDs are not due to movement away from the depth of field as membrane undulations are smaller than the depth of field[261] and possible endosomal trafficking would unlikely oscillate particles back and forth within the recorded timescales of the experiment. Additionally, if such effects were occurring the BSQDs should exhibit similar behaviors, which were not observed. There are programs which can reconstruct lost traces from nonemissive periods of the probe by assuming a diffusion coefficient determined from the previous frames, but as can be seen in the MSD plots in **Figure 5.5**, errors in assigning possible trajectories will grow continually with time. Therefore for prolonged off periods, or a greater number of frames taken without signal, these assumed trajectories can accumulate significant errors. In the case of Brownian diffusion, the standard error can be calculated from the following formula.[262]

$$\sigma = 4Dt_{lag}\begin{cases}\left[\left(4n^2(N-n)+2(N-n)+n-n^3\right)\Big/\left(6n(N-n)^2\right)\right]^{1/2} & n \le \dfrac{N}{2} \\ \left[1+\left((N-n)^3-4n(N-n)^2+4n-(N-n)\right)\Big/\left(6n^2(N-n)\right)\right]^{1/2} & n > \dfrac{N}{2}\end{cases} \quad (5.9)$$

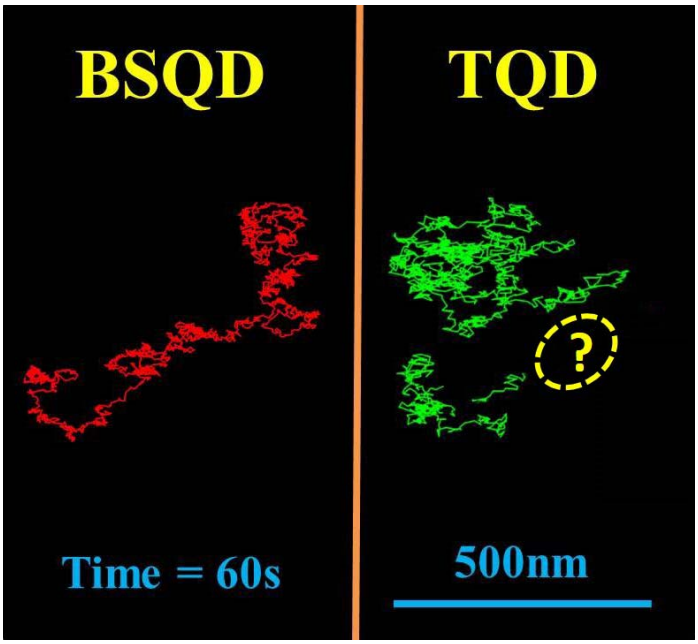

Figure 5.6 60 Second Trajectories of QDs Exhibiting Brownian Type Diffusion. 60 s time traces of a blinking suppressed quantum dot (BSQD) compared to a commercially available traditional core shell QD. As can be seen in the traditional QD, prolonged off times leave frames with no signal when taken at frame rates of 33 Hz as for the blinking suppressed QD all frames had a signal.

Dynamic intensity traces were created of single emitters using the wide field imaging CCD camera images, where intensity values are recorded for each frame within a 60 s stack at a 33 Hz frame rate using the MacBiophotonics plugin within the software Image J. Upon inspection of the dynamic intensity traces of a single dot from the TQD and BSQD samples, markedly different optical characteristics are observed as seen in **Figure 5.7**. There are great fluctuations in the intensity profile of the TQD, whereas the BSQDs have more consistent emission during a 60 s interval exhibiting much less variance in the intensity distribution. Though the single TQD can yield signals almost 3 times brighter than the BSQD in several frames, this brightness is highly unstable over time. If one considers the integrated intensity over the 60 s interval, the BSQD has 1.2

times the output of TQD. Greater intensities are desired as one can achieve higher signal to noise ratios needed for moving to higher magnifications, but for observing dynamics with high speeds, a consistent signal is of greater importance.

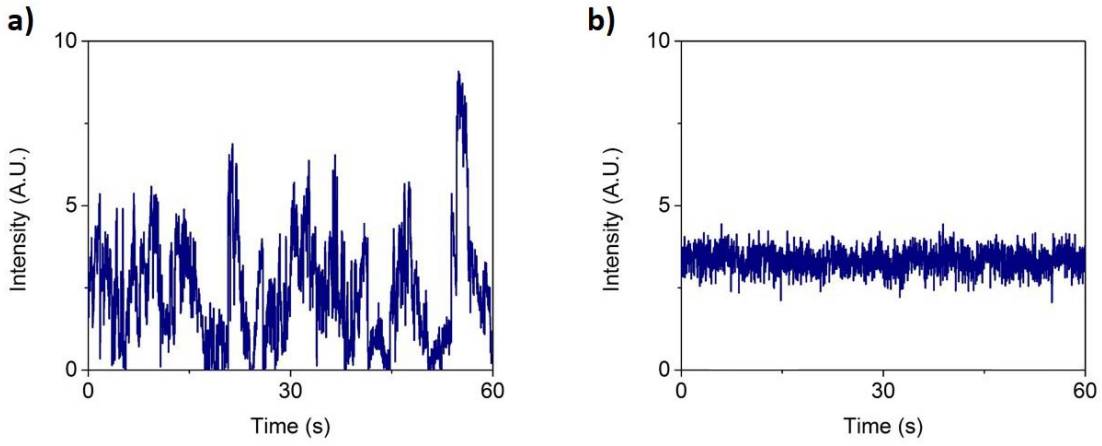

Figure 5.7 60 Second Intensity Traces of Single QDs in a Biological Environment. **a)** traditional core/shell QD, and **b)** blinking suppressed QD.

In confined diffusion regimes, the regions of travel for the particles are kept in domains less than 200 nm. Therefore in the final trace reconstruction of the TQD within such domains, large regions of uncertainty in travel are not commonly observed. Generally the lost connections of the TQD trajectory, due to the lost points from frames with no signal, are unnoticed when looking at the final trace. With the full trace plotted, no observable differences between the BSQD and the TQD are seen (**Figure 5.8)**. Though if the experiment was conducted with an apparatus that had a CCD with greater pixel number and faster acquisition rates along with higher objective magnification, off regions in this diffusional regime may become more evident.

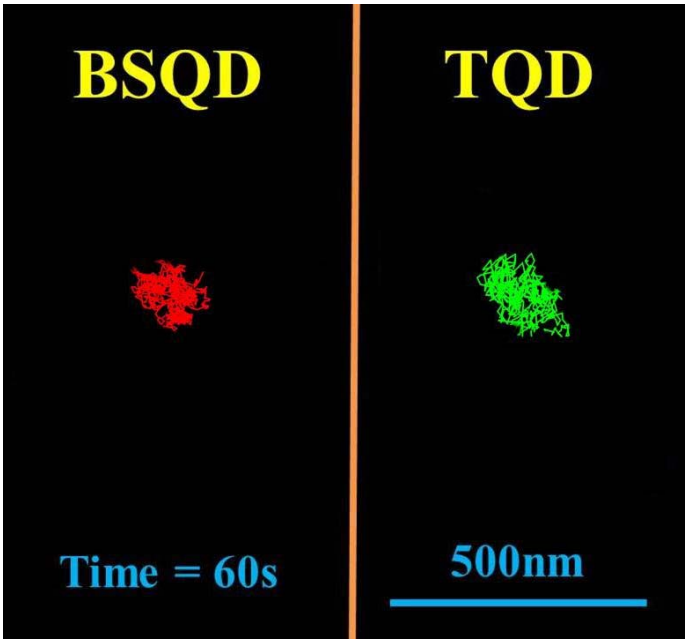

Figure 5.8 60 Second Trajectories of QDs Exhibiting Confined Type Diffusion. 60 s time traces of a blinking suppressed quantum dot (BSQD) compared to a commercially available traditional core shell QD displaying confined diffusion. Since the trajectories in a frame are limited, the region of uncertainty in an off time for a traditional QD is less noticed.

CHAPTER 6

FUTURE DIRECTIONS

In this chapter, the work presented in the previous chapters will be summarized. Also, a discussion of future directions for building upon this work is provided.

6.1 Summary

The work of this dissertation is focused on the design and synthesis of blinking suppressed probes for live cell single molecule tracking applications. The framework in which to design these probes was developed on the basis of preventing the exciton carriers from reaching trap states in order to minimize nonradiative events. With an established design, synthesis measures had to be established in order to produce particles adhering to such a framework. After successful synthesis of the blinking suppressed probes, their optical properties were inspected and a comparative single molecule tracking experiment was performed to elucidate the potential benefits these probes may have over conventional quantum dots.

The first chapter started with a description of how small nanosized objects are, then moved to introduce an emergent phenomenon seen with these tiny objects. This phenomenon is that materials shrunken to nanometer scales can have optical properties tuned solely through adjustments in their size without changes in chemical composition.

A subclass of such nanomaterials, called quantum dots, have exceptional size-tunable fluorescent properties which have a number of considerable advantages in bioimaging applications when compared to conventional organic dyes. Despite the superior optical properties, the undesired phenomenon observed on the single particle level of fluorescent intermittency (blinking) is shared between quantum dots and other fluorescent emitters. In the midst of fluorescence intermittency, periods of off states can be prolonged to time scales where significant diffusion lengths have been traversed by the particle in a single molecule tracking experiment. Having long paths without a signal leaves significant complications on reconstructing the trajectory accurately as cells are heterogeneous and can display time varying anisotropic diffusion coefficients. Though there are quite a few reports on blinking suppressed probes, only a couple of reports have shown applicability in low loss data acquisition in single molecule tracking experiments. In addition, these successfully applied probes are limited in materials which can be used for synthesis preventing the establishment of a generalized method in which to create such structures. The problem was then laid to generate blinking suppressed quantum dots with a generalizable method where one will not be limited in the materials of particle synthesis or bioconjugation techniques in order to advance their use in single molecule tracking.

Chapter 2 begins with the physics behind the electronic structure of crystalline materials starting from single atoms and working up to infinite lattices. From this analysis it is found that the electronic structure of bulk semiconductors display a region of energies which are not permissible for an electron to access which is called the band gap. This band gap specifies a threshold absorption energy above which is required for

excitation, and what wavelength of photons can be emitted from the structure after excitation. Results obtained from Fermi's Golden Rule are then introduced to show the efficiency and lifetime of the fluorescence depending on the type of band gap the structure has which indicates direct gap materials are better emitters with shorter lifetimes than indirect. The chapter then presents the electronic structure of quantum dots which are somewhere in between single atoms and bulk structures. Afterwards, the chapter gives a basic overview on the methods of QD synthesis, how to maintain monodispersity, in addition to controlling optical properties such as the quantum yield along with fluorescent wavelength and lifetimes through use of core/shell architectures based on the band offsets between these materials. Finally, some biological applications of quantum dots are presented. Within this section, the superior optical properties which these probes have over conventional fluorophores utilized in fluorescent labeling of biological molecules is discussed in greater depth. Next, their uses in cellular and tissue imaging with a brief introduction to toxicity concerns of the probes for in vivo applications is provided. Lastly, works successfully applying quantum dots to single molecule tracking experiments are presented showing the great potential for use of these probes in this area where toxicity issues are less of a concern.

In chapter 3, the blinking behavior of quantum dots is explained in more depth along with the current theories of its occurrence. The theories of the blinking process, though with quite varying descriptions, mainly boil down to two types of nonradiative events consisting of exciton carrier trapping or Auger recombination. These two processes are not necessarily independent as an Auger event may first require trapping of a carrier. Therefore the design of the blinking suppressed probes of this work was

focused on minimizing the exciton carrier's access to trap sites. Previous works on such a method have been dedicated towards avoiding surface traps where access is minimized through generating type-I structures having giant shells to surround the quantum dot core. Despite the success of this method, it has been limited to only the CdSe/CdS core/shell system. It is then proposed that the inability of thick shells of other materials to generate type-I structures displaying blinking suppression for CdSe cores is due to the greater lattice mismatches than CdS which accumulate enough strain at the heterojunction to introduce new internal defects which act as trap sites. At this point the concept of minimizing epitaxial strain to prevent defect formation within the crystal is introduced in order to move beyond shells of only CdS for obtaining shell thicknesses required for blinking suppression. Such strain minimization can be provided by linearly grading the shell material from the pure core material to the pure shell material. Linear grading methods are routinely applied in the electronics industry where interfacial defect formation is avoided by linearly grading a pure silicon substrate to pure germanium on the surface of the epitaxial layer. The CdSe/$Cd_{1-x}Zn_xSe$ linearly graded shell system was chosen to apply this concept due to the simplicity of only needing to change the cation in the system. To carry out the synthesis of the structure, particular choices in precursors and reaction conditions were needed in order to ensure successful outcomes. The procedure mainly entailed using highly reactive shell precursors introduced slowly into the reaction vessel using the SILAR method while gradually increasing the content of primary to secondary amines for isotropic growth and aggregation prevention. After synthesis, the structures were phase transferred to aqueous solutions using three different ligand replacement strategies to ensure that they maintain their optical properties

regardless of the solubilization ligands chosen to widen ones choices in bioconjugation strategies in applying the probes to biomolecule tracking.

Chapter 4 starts with introducing the components and operating principles behind the TCSPC apparatus used in the single particle fluorescence spectroscopy measurements carried out in the study. In these studies dilute QD samples are spun onto microscope slides which are then inspected with an apparatus which records the number of fluorescent photons coming from a diffraction limited spot on the slide over time. In addition, an AFM is used to verify if a single quantum dot is being inspected within the illumination region. Here, once an intensity trace is recorded, an AFM scan is performed and the intensity data is rejected if more than one QD is within a diffraction limited area. The first experimental results presented in the chapter are the dynamic intensity traces between the starting cores used to prepare the linear graded alloy shell particles and the final shelled product, both in the organic phase. A remarkable change in the blinking properties was observed between the starting and final product as the cores were almost always off whereas with the linearly graded shell particles were almost always on. With 100 particles of the blinking suppressed probes being examined for at least 600 seconds, the ensemble on time percentages followed a closely to a Gaussian distribution having a mean above 92 % on. Almost a quarter of the sample was able to display on times greater than 99 %. Also, the fluorescent lifetime was recorded for the blinking suppressed probes showing little lifetime increase from that of the starting cores, but displayed greater monoexponential behavior. Monoexponetial behavior, opposed to multiexponetial, of the fluorescent lifetime is typically observed when blinking suppression has been achieved possibly due to elimination of short lived trap states.

Finally, the linearly graded alloy shell particles that were transferred to the aqueous phase were compared. Remarkably little to no optical property changes were observed whether the blinking suppressed probes were in the organic phase or what type of solubilizing ligand was chosen for the samples in the aqueous phase. The distribution of 100 particles inspected for each sample had similar means and variances for the percent on time.

To start chapter 5, the operating principles and methods of the wide field apparatus employed for single molecule tracking was presented. Then the method for bioconjugating EGFR antibodies to the QDs was described along with the procedures for adhering such QDs to the surface of A549 cells for single molecule tracking studies. For the tracking studies the data was fitted into either two diffusion regimes: one being Brownian like diffusion where the mean squared displacement of the probe is a linear function with time, the other being confined diffusion where the mean squared displacement follows a sublinear function with time. In order to illustrate the benefits of using blinking suppressed probes for single molecule tracking, a traditional core shell particle with the same solvating ligands and bioconjugation strategy as the linearly graded alloy shell QDs was used as a comparison**.** Results found that under faster diffusional velocities, typically in the Brownian regime, large regions of uncertainty can be easily seen in the trajectories for traditional QDs whereas the blinking suppressed QDs had no such issues. Though, under confined diffusion regimes where the velocities are slowed and the regions of travel are much shorter, no large trace gaps are observed under our experimental conditions. Interestingly despite slight changes in the

hydrodynamic diameter between the traditional and blinking suppressed QDs, little changes to the diffusional behavior were observed.

6.2 Future Directions for Blinking Suppressed Probes

As described above, the work discussed in this dissertation mainly focuses on the development of blinking suppressed probes for single molecule tracking. While the results of this work can convincingly demonstrate the usefulness of such particles for tracking studies, further developments can be applied: demonstrate the generalizable gradient allying method for the shell to a wider variety of material systems, verifying gradients which suppress blinking using newly developed depth profiling methods with atomic layer resolution, increase and confirm the monovalency of the probe sample, and track particle motions using a CCD with higher frame rates and greater number of pixels for better inspection of confined diffusion regimes. Here, we discuss these future directions of studies that should be undertaken to further advance the use of blinking suppressed probes in single molecule tracking studies.

6.2.1 Extending the Gradient Alloying Method to Other Semiconducting Materials

The method applied for blinking suppression in this work should be generalizable to other materials than the CdZnSe system in this work. It has been found in the CdSe/CdS core/shell system that though alloying is not needed for blinking suppression, it is a contributor in suppression of Auger recombination which is believed

to be one of the factors for nonradiative events in nanocrystals.[263] The next system to investigate would be CdSe alloying with ZnS. Quantum dots with ZnS outer layers are least prone to oxidation of the II-VI materials in addition to being more biocompatible. It has been found previously that compositionally graded steps from CdSe to a pure ZnS outer layer had lowered the fluorescent intermittency.[196] In this case since ZnS has a higher lattice mismatch than the ZnSe employed in this work, a linear gradient with less of a slope may be needed in order to extend the critical thickness sufficient enough to curb exciton carriers from the surface of the crystal. The method also has potential to be applied to III-V quantum dots, however, the chemistry is less understood than the II-VI materials with results of less monodisperse samples with lower quantum yields. In addition, the III-V QDs are more prone to oxidation. Despite these hurdles, there are great opportunities for improving III-V synthesis methods. With these materials one can get fluorescent wavelengths suitable for biological imaging without the use of cadmium, thereby alleviating heavy metal concerns. This avenue may open the doors to QDs being able to perform in vivo single molecule tracking experiments in the future.

6.2.2 Verifying Gradient Structures through Use of Newly Developed High Resolution Compositional Profiling Techniques

The ability to quantitatively confirm the compositional profile throughout a graded alloy nanocrystal is lacking with conventional material characterization methods. Quantum dots have been characterized through such methods as scanning transmission electron microscopy[264,265] together with electron energy loss spectroscopy or energy

dispersive spectrometry, high-resolution transmission electron microscopy (HRTEM),[266] X-ray phasing,[267] and X-ray photoelectron spectroscopy (XPS).[268-270] These methods though are incapable of depth profiling at resolutions of single atomic layers which are necessary to verify gradient alloy crystals. For instance, XPS delivers surface compositions weighted by an electron attenuation length of a few nanometers which leaves the resolution below that which is needed. New methods which recently developed such as Time-of-Flight Medium Energy Ion Scattering Spectroscopy[271] or possibly enhancing the resolution of XPS by using highly controlled radiation energies via a synchrotron radiation source which can regulate the sampling depth within the particle.[272] With such detailed information one can begin to analyze what types of gradient profiles and at what thicknesses shells of varying materials provide the optimal blinking suppression and quantum yield for continuously bright particles.

6.2.3 Controlling and Confirming Monovalency of Single Molecule Probes

Frequently used methods for bioconjugating QDs result in samples with valencies following a Poisson distribution due to the existence of several reactive sites at the particle surface.[251] The multivalent probes within the sample may upset the function of their target through oligomerization, causing receptor activation, internalization or redistribution on the cell surface.[231,273,274] Such effects may be observed as significant variations in the mobility of the targeted probe.[231] Initial efforts for increased monovalent probes within samples focused on advancement of purification procedures to remove multivalent particles from the solution.[273,275,276] These methods,

however, are quite tedious, having multiple steps involved and results in low sample yields. Recent efforts have focused on synthesizing QDs of controlled valency without need for purification,[277,278] though these methods suffer from low product yields as well. A method which may be promising on generating larger yields of monovalent probes is through using steric exclusion effects of the affinity agents on the probes.[279] This technique exploits the large size of the affinity molecules, compared to the area for binding on the QDs, to limit valency of products where steric crowding prevents multiple molecules adhering to the surface.[277,280] The authors have reported to yield almost complete monovalent samples through this method.[279] Such improved techniques for complete monovalent samples in combination with blinking suppression of the QDs can make great strides in the single molecule tracking field.

6.2.4 Single Molecule Tracking of Blinking Suppressed Probes with Higher Frame Rates

A majority of the single particle tracking experiments to date, including the tracking experiments in this work, have been accomplished at sampling frequencies at 30 Hz or lower. With such frame rates of image acquisition, one can see the fluorophores transiently confined for extended periods inside domains with a size of 100−300 nm in diameter,[51,255,281,282] which has also been observed in this study. In tracking studies using much faster frame rates of 50 kHz have revealed that the motion of both lipids and proteins within the plasma membrane are subject to transient confinement in nanosized compartments.[237,283,284] Within these compartments, the

objects are assumed to diffuse freely with diffusion constants similar to those found in model membranes, while on an extended time scale the objects move among neighboring compartments resulting in long-term diffusion at an order of magnitude slower.[283] Such diffusion behavior has been named hop diffusion and can only be observed at sampling rates which are considerably faster than the corresponding duration of time that the object spends within these nanosized compartments.[285] For example, the confinement time to experience the effect of the barrier from the studies carried out in this work using equation 5.6 was calculated to be 25 ms. This is shorter than the time between corresponding frames (30.3ms) of the experiment, therefore to attain better information about this transition it will require the ability to reach frame rates on the kHz scale. Additionally, the blinking suppressed probes of this work may be even more beneficial for tracking at very high frame rates where the number of frames without signal would increase substantially using traditional QDs.

6.3 Conclusions

In conclusion, this chapter summarized the work of this dissertation and described several future directions for extending this research. This work has made contributions of developing a generalized method for synthesizing blinking suppressed quantum dots which can be applied to single biomolecule tracking experiments and showed their potential in such experiments. These particles have the ability to remain valuable single molecule tracking probes as cameras continue to gain more pixels

operating at faster speeds allowing experiments to be performed with greater magnifications at higher frame rates.

REFERENCES

1 Sun, Q. *et al.* Bright, multicoloured light-emitting diodes based on quantum dots. *Nat Photon* **1**, 717-722 (2007).

2 Zhao, J. *et al.* Efficient CdSe/CdS Quantum Dot Light-Emitting Diodes Using a Thermally Polymerized Hole Transport Layer. *Nano Letters* **6**, 463-467 (2006).

3 Caruge, J. M., Halpert, J. E., Wood, V., Bulovic, V. & Bawendi, M. G. Colloidal quantum-dot light-emitting diodes with metal-oxide charge transport layers. *Nat Photon* **2**, 247-250 (2008).

4 Tan, Z. *et al.* Bright and Color-Saturated Emission from Blue Light-Emitting Diodes Based on Solution-Processed Colloidal Nanocrystal Quantum Dots. *Nano Letters* **7**, 3803-3807 (2007).

5 McDonald, S. A. *et al.* Solution-processed PbS quantum dot infrared photodetectors and photovoltaics. *Nat Mater* **4**, 138-142 (2005).

6 Leschkies, K. S. *et al.* Photosensitization of ZnO Nanowires with CdSe Quantum Dots for Photovoltaic Devices. *Nano Letters* **7**, 1793-1798 (2007).

7 Chan, W. C. W. & Nie, S. Quantum Dot Bioconjugates for Ultrasensitive Nonisotopic Detection. *Science* **281**, 2016-2018 (1998).

8 Jaiswal, J. K., Mattoussi, H., Mauro, J. M. & Simon, S. M. Long-term multiple color imaging of live cells using quantum dot bioconjugates. *Nat Biotech* **21**, 47-51 (2003).

9 Wu, X. *et al.* Immunofluorescent labeling of cancer marker Her2 and other cellular targets with semiconductor quantum dots. *Nat Biotech* **21**, 41-46 (2003).

10 Hohng, S. & Ha, T. Single-Molecule Quantum-Dot Fluorescence Resonance Energy Transfer. *ChemPhysChem* **6**, 956-960 (2005).

11 Dahan, M. *et al.* Diffusion dynamics of glycine receptors revealed by single-quantum dot tracking. *Science* **302**, 442-445 (2003).

12 Bruchez, M., Moronne, M., Gin, P., Weiss, S. & Alivisatos, A. P. Semiconductor Nanocrystals as Fluorescent Biological Labels. *Science* **281**, 2013-2016 (1998).

13 Schröck, E. *et al.* Multicolor Spectral Karyotyping of Human Chromosomes. *Science* **273**, 494-497 (1996).

14 Hermanson, G. T. (Academic Press, London, 1996).

15 Heim, R. & Tsien, R. Engineering green fluorescent protein for improved brightness, longer wavelengths and fluorescence resonance energy transfer. *Current Biology* **6**, 178-182 (1996).

16 Michalet, X. *et al.* Quantum Dots for Live Cells, in Vivo Imaging, and Diagnostics. *Science* **307**, 538-544 (2005).

17 Medintz, I. L., Uyeda, H. T., Goldman, E. R. & Mattoussi, H. Quantum dot bioconjugates for imaging, labelling and sensing. *Nat Mater* **4**, 435-446 (2005).

18 Resch-Genger, U., Grabolle, M., Cavaliere-Jaricot, S., Nitschke, R. & Nann, T. Quantum dots versus organic dyes as fluorescent labels. *Nat Meth* **5**, 763-775 (2008).

19 Mattoussi, H., Kuno, M. K. & Goldman, E. R. Colloidal semiconductor quantum dot conjugates in biosensing,. *Optical Biosensors: Present and Future*, 537-569 (2002).
20 Bruchez, M., Jr. & Hotz, C. Z. (Humana Press, Totowa, NJ, 2007).
21 Alivisatos, P. The use of nanocrystals in biological detection. *Nat Biotech* **22**, 47-52 (2004).
22 Kim, S. *et al.* Near-infrared fluorescent type II quantum dots for sentinel lymph node mapping. *Nat Biotech* **22**, 93-97 (2004).
23 Dabbousi, B. O. *et al.* (CdSe)ZnS Core−Shell Quantum Dots: Synthesis and Characterization of a Size Series of Highly Luminescent Nanocrystallites. *The Journal of Physical Chemistry B* **101**, 9463-9475 (1997).
24 Han, M., Gao, X., Su, J. Z. & Nie, S. Quantum-dot-tagged microbeads for multiplexed optical coding of biomolecules. *Nat Biotech* **19**, 631-635 (2001).
25 Smith, A. M. & Nie, S. Bright and Compact Alloyed Quantum Dots with Broadly Tunable Near-Infrared Absorption and Fluorescence Spectra through Mercury Cation Exchange. *Journal of the American Chemical Society* **133**, 24-26 (2010).
26 Zondervan, R., Kulzer, F., Orlinskii, S. B. & Orrit, M. Photoblinking of Rhodamine 6G in Poly(vinyl alcohol): Radical Dark State Formed through the Triplet. *The Journal of Physical Chemistry A* **107**, 6770-6776 (2003).
27 Frantsuzov, P., Kuno, M., Janko, B. & Marcus, R. A. Universal emission intermittency in quantum dots, nanorods and nanowires. *Nat Phys* **4**, 519-522 (2008).
28 Jaiswal, J. K. & Simon, S. M. Potentials and pitfalls of fluorescent quantum dots for biological imaging. *Trends in Cell Biology* **14**, 497-504 (2004).
29 Pinaud, F., Clarke, S., Sittner, A. & Dahan, M. Probing cellular events, one quantum dot at a time. *Nat Meth* **7**, 275-285 (2010).
30 Calamai, M. *et al.* Gephyrin oligomerization controls GlyR mobility and synaptic clustering. *The Journal of Neuroscience* **29**, 7639-7648 (2009).
31 Chang, Y. P., Pinaud, F., Antelman, J. & Weiss, S. Tracking bio-molecules in live cells using quantum dots. *Journal of biophotonics* **1**, 287-298 (2008).
32 Groc, L. *et al.* Surface trafficking of neurotransmitter receptor: comparison between single-molecule/quantum dot strategies. *The Journal of Neuroscience* **27**, 12433-12437 (2007).
33 Schwille, P., Korlach, J. & Webb, W. W. Fluorescence correlation spectroscopy with single-molecule sensitivity on cell and model membranes. *Cytometry* **36**, 176-182 (1999).
34 Nirmal, M. *et al.* Fluorescence intermittency in single cadmium selenide nanocrystals. *Nature* **383**, 802-804 (1996).
35 Galland, C. *et al.* Two types of luminescence blinking revealed by spectroelectrochemistry of single quantum dots. *Nature* **479**, 203-207 (2011).
36 Efros, A. L. & Rosen, M. Random Telegraph Signal in the Photoluminescence Intensity of a Single Quantum Dot. *Physical Review Letters* **78**, 1110-1113 (1997).
37 Frantsuzov, P. A. & Marcus, R. A. Explanation of quantum dot blinking without the long-lived trap hypothesis. *Physical Review B* **72**, 155321 (2005).

38 Kuno, M., Fromm, D. P., Hamann, H. F., Gallagher, A. & Nesbitt, D. J. ``On"/``off" fluorescence intermittency of single semiconductor quantum dots. *The Journal of Chemical Physics* **115**, 1028-1040 (2001).
39 Tang, J. & Marcus, R. A. Mechanisms of fluorescence blinking in semiconductor nanocrystal quantum dots. *The Journal of Chemical Physics* **123**, 054704-054712 (2005).
40 Cragg, G. E. & Efros, A. L. Suppression of Auger Processes in Confined Structures. *Nano Letters* **10**, 313-317, doi:10.1021/nl903592h (2009).
41 Cherniavskaya, O., Chen, L. & Brus, L. Imaging the Photoionization of Individual CdSe/CdS Core−Shell Nanocrystals on n- and p-Type Silicon Substrates with Thin Oxides. *The Journal of Physical Chemistry B* **108**, 4946-4961 (2004).
42 Hohng, S. & Ha, T. Near-Complete Suppression of Quantum Dot Blinking in Ambient Conditions. *Journal of the American Chemical Society* **126**, 1324-1325, doi:10.1021/ja039686w (2004).
43 Fomenko, V. & Nesbitt, D. J. Solution Control of Radiative and Nonradiative Lifetimes: A Novel Contribution to Quantum Dot Blinking Suppression. *Nano Letters* **8**, 287-293 (2007).
44 Chen, Y. *et al.* "Giant" multishell CdSe nanocrystal quantum dots with suppressed blinking. *Journal of the American Chemical Society* **130**, 5026-5027 (2008).
45 Wang, X. *et al.* Non-blinking semiconductor nanocrystals. *Nature* **459**, 686-689 (2009).
46 Nakagawa, Y., Nakajima, K., Tayama, S. & Moldéus, P. Metabolism and cytotoxicity of propyl gallate in isolated rat hepatocytes: effects of a thiol reductant and an esterase inhibitor. *Molecular Pharmacology* **47**, 1021-1027 (1995).
47 Gregory, L. *et al.* The solution conformations of the subclasses of human IgG deduced from sedimentation and small angle X-ray scattering studies. *Molecular Immunology* **24**, 821-829 (1987).
48 Qin, H. *et al.* Single-Dot Spectroscopy of Zinc-Blende CdSe/CdS Core/Shell Nanocrystals: Nonblinking and Correlation with Ensemble Measurements. *Journal of the American Chemical Society* **136**, 179-187 (2013).
49 Chen, O. *et al.* Compact high-quality CdSe–CdS core–shell nanocrystals with narrow emission linewidths and suppressed blinking. *Nat Mater* **12**, 445-451 (2013).
50 Andrews, N. L. *et al.* Actin restricts Fcϵ RI diffusion and facilitates antigen-induced receptor immobilization. *Nature cell biology* **10**, 955-963 (2008).
51 Pinaud, F. *et al.* Dynamic Partitioning of a Glycosyl-Phosphatidylinositol-Anchored Protein in Glycosphingolipid-Rich Microdomains Imaged by Single-Quantum Dot Tracking. *Traffic* **10**, 691-712 (2009).
52 Frischknecht, R. *et al.* Brain extracellular matrix affects AMPA receptor lateral mobility and short-term synaptic plasticity. *Nature neuroscience* **12**, 897-904 (2009).
53 Triller, A. & Choquet, D. New concepts in synaptic biology derived from single-molecule imaging. *Neuron* **59**, 359-374 (2008).

54 Marchuk, K., Guo, Y., Sun, W., Vela, J. & Fang, N. High-precision tracking with non-blinking quantum dots resolves nanoscale vertical displacement. *Journal of the American Chemical Society* **134**, 6108-6111 (2012).
55 Nishimura, H. *et al.* Biocompatible fluorescent silicon nanocrystals for single-molecule tracking and fluorescence imaging. *The Journal of cell biology* **202**, 967-983 (2013).
56 Sako, Y. Single molecule imaging of EGFR signal transduction on the living cell surface. *Nature Cell Biol* **2**, 168-172 (2000).
57 Seisenberger, G. *et al.* Real-Time Single-Molecule Imaging of the Infection Pathway of an Adeno-Associated Virus. *Science* **294**, 1929-1932 (2001).
58 Visnapuu, M.-L. & Greene, E. C. Single-molecule imaging of DNA curtains reveals intrinsic energy landscapes for nucleosome deposition. *Nat Struct Mol Biol* **16**, 1056-1062 (2009).
59 Efros, A. L. & Efros, A. L. Interband absorption of light in a semiconductor sphere. *Sov. Phys. Semiconduct* **16**, 775-778 (1982).
60 Ekimov, A. I. & Onushchenko, A. A. Quantum size effect in the optical-spectra of semiconductor micro-crystals. *Sov. Phys. Semiconduct* **16**, 775-778 (1982).
61 Rossetti, R., Ellison, J., Gibson, J. & Brus, L. Size effects in the excited electronic states of small colloidal CdS crystallites. *The Journal of chemical physics* **80**, 4464 (1984).
62 Rossetti, R., Nakahara, S. & Brus, L. Quantum size effects in the redox potentials, resonance Raman spectra, and electronic spectra of CdS crystallites in aqueous solution. *The Journal of Chemical Physics* **79**, 1086-1088 (1983).
63 Murray, C., Norris, D. & Bawendi, M. G. Synthesis and characterization of nearly monodisperse CdE (E= sulfur, selenium, tellurium) semiconductor nanocrystallites. *Journal of the American Chemical Society* **115**, 8706-8715 (1993).
64 Chan, W. C. & Nie, S. Quantum dot bioconjugates for ultrasensitive nonisotopic detection. *Science* **281**, 2016-2018 (1998).
65 Segall, M. *et al.* First-principles simulation: ideas, illustrations and the CASTEP code. *Journal of Physics: Condensed Matter* **14**, 2717 (2002).
66 Wei, S.-H. & Zunger, A. Calculated natural band offsets of all II–VI and III–V semiconductors: Chemical trends and the role of cation d orbitals. *Applied Physics Letters* **72**, 2011-2013 (1998).
67 Reiss, P., Protière, M. & Li, L. Core/Shell Semiconductor Nanocrystals. *Small* **5**, 154-168 (2009).
68 Borrelli, N. F., Hall, D., Holland, H. & Smith, D. Quantum confinement effects of semiconducting microcrystallites in glass. *Journal of Applied Physics* **61**, 5399-5409 (1987).
69 Brus, L. E. A simple model for the ionization potential, electron affinity, and aqueous redox potentials of small semiconductor crystallites. *The Journal of Chemical Physics* **79**, 5566-5571 (1983).
70 Brus, L. E. Electron–electron and electron-hole interactions in small semiconductor crystallites: The size dependence of the lowest excited electronic state. *The Journal of Chemical Physics* **80**, 4403-4409 (1984).

71 Petroff, P. & Medeiros-Ribeiro, G. Three-dimensional carrier confinement in strain-induced self-assembled quantum dots. *MRS Bulletin-Materials Research Society* **21**, 50-54 (1996).
72 Yoffe, A. Semiconductor quantum dots and related systems: electronic, optical, luminescence and related properties of low dimensional systems. *Advances in Physics* **50**, 1-208 (2001).
73 Lipovskii, A. *et al.* Synthesis and characterization of PbSe quantum dots in phosphate glass. *Applied physics letters* **71**, 3406-3408 (1997).
74 Potter Jr, B. G. & Simmons, J. H. Quantum size effects in optical properties of CdS-glass composites. *Physical Review B* **37**, 10838 (1988).
75 Yu, W. W. & Peng, X. Formation of High-Quality CdS and Other II–VI Semiconductor Nanocrystals in Noncoordinating Solvents: Tunable Reactivity of Monomers. *Angewandte Chemie International Edition* **41**, 2368-2371 (2002).
76 LaMer, V. K. & Dinegar, R. H. Theory, production and mechanism of formation of monodispersed hydrosols. *Journal of the American Chemical Society* **72**, 4847-4854 (1950).
77 Murray, C. B. *et al.* Colloidal synthesis of nanocrystals and nanocrystal superlattices. *IBM Journal of Research and Development* **45**, 47-56 (2001).
78 Liu, H., Owen, J. S. & Alivisatos, A. P. Mechanistic study of precursor evolution in colloidal group II-VI semiconductor nanocrystal synthesis. *J Am Chem Soc* **129**, 305-312 (2007).
79 Steckel, J. S., Yen, B. K. H., Oertel, D. C. & Bawendi, M. G. On the mechanism of lead chalcogenide nanocrystal formation. *J Am Chem Soc* **128**, 13032-13033 (2006).
80 van Embden, J. & Mulvaney, P. Nucleation and growth of CdSe nanocrystals in a binary ligand system. *Langmuir* **21**, 10226-10233 (2005).
81 Thessing, J., Qian, J., Chen, H., Pradhan, N. & Peng, X. Interparticle influence on size/size distribution evolution of nanocrystals. *J Am Chem Soc* **129**, 2736-2737 (2007).
82 Xie, R. & Peng, X. Synthetic Scheme for High-Quality InAs Nanocrystals Based on Self-Focusing and One-Pot Synthesis of InAs-Based Core–Shell Nanocrystals. *Angewandte Chemie* **120**, 7791-7794 (2008).
83 Chen, Y., Johnson, E. & Peng, X. Formation of Monodisperse and Shape-Controlled MnO Nanocrystals in Non-Injection Synthesis: Self-Focusing via Ripening. *Journal of the American Chemical Society* **129**, 10937-10947, doi:10.1021/ja073023n (2007).
84 Nozik, A. J. & Micic, O. Colloidal quantum dots of III-V semiconductors. *MRS Bulletin-Materials Research Society* **23**, 24-30 (1998).
85 Peng, Z. A. & Peng, X. Formation of high-quality CdTe, CdSe, and CdS nanocrystals using CdO as precursor. *Journal of the American Chemical Society* **123**, 183-184 (2001).
86 Higginson, K. A. *et al.* Synthesis and characterization of colloidal β-HgS quantum dots. *The Journal of Physical Chemistry B* **106**, 9982-9985 (2002).
87 Peng, X., Wickham, J. & Alivisatos, A. Kinetics of II-VI and III-V colloidal semiconductor nanocrystal growth:"focusing" of size distributions. *Journal of the American Chemical Society* **120**, 5343-5344 (1998).

88 Qu, L., Peng, Z. A. & Peng, X. Alternative routes toward high quality CdSe nanocrystals. *Nano Letters* **1**, 333-337 (2001).
89 Peng, X. *et al.* Shape control of CdSe nanocrystals. *Nature* **404**, 59-61 (2000).
90 Qu, L. & Peng, X. Control of photoluminescence properties of CdSe nanocrystals in growth. *Journal of the American Chemical Society* **124**, 2049-2055 (2002).
91 Hines, M. A. & Guyot-Sionnest, P. Bright UV-blue luminescent colloidal ZnSe nanocrystals. *The Journal of Physical Chemistry B* **102**, 3655-3657 (1998).
92 Peng, X., Schlamp, M. C., Kadavanich, A. V. & Alivisatos, A. Epitaxial growth of highly luminescent CdSe/CdS core/shell nanocrystals with photostability and electronic accessibility. *Journal of the American Chemical Society* **119**, 7019-7029 (1997).
93 Murphy, C. J. Peer reviewed: Optical sensing with quantum dots. *Analytical Chemistry* **74**, 520 A-526 A (2002).
94 Hines, M. A. & Guyot-Sionnest, P. Synthesis and characterization of strongly luminescing ZnS-capped CdSe nanocrystals. *The Journal of Physical Chemistry* **100**, 468-471 (1996).
95 Dabbousi, B. *et al.* (CdSe) ZnS core-shell quantum dots: synthesis and characterization of a size series of highly luminescent nanocrystallites. *The Journal of Physical Chemistry B* **101**, 9463-9475 (1997).
96 Reiss, P., Bleuse, J. & Pron, A. Highly luminescent CdSe/ZnSe core/shell nanocrystals of low size dispersion. *Nano letters* **2**, 781-784 (2002).
97 McBride, J., Treadway, J., Feldman, L., Pennycook, S. J. & Rosenthal, S. J. Structural basis for near unity quantum yield core/shell nanostructures. *Nano letters* **6**, 1496-1501 (2006).
98 Greytak, A. B. *et al.* Alternating layer addition approach to CdSe/CdS core/shell quantum dots with near-unity quantum yield and high on-time fractions. *Chemical Science* **3**, 2028-2034 (2012).
99 Saha, A. *et al.* Near-Unity Quantum Yield in Semiconducting Nanostructures: Structural Understanding Leading to Energy Efficient Applications. *The Journal of Physical Chemistry Letters* **4**, 3544-3549, doi:10.1021/jz401958u (2013).
100 Cao, Y. & Banin, U. Growth and properties of semiconductor core/shell nanocrystals with InAs cores. *Journal of the American Chemical Society* **122**, 9692-9702 (2000).
101 Micic, O. I., Smith, B. B. & Nozik, A. J. Core-shell quantum dots of lattice-matched ZnCdSe2 shells on InP cores: Experiment and theory. *The Journal of Physical Chemistry B* **104**, 12149-12156 (2000).
102 Li, J. J. *et al.* Large-Scale Synthesis of Nearly Monodisperse CdSe/CdS Core/Shell Nanocrystals Using Air-Stable Reagents via Successive Ion Layer Adsorption and Reaction. *Journal of the American Chemical Society* **125**, 12567-12575 (2003).
103 Xie, R., Kolb, U., Li, J., Basché, T. & Mews, A. Synthesis and characterization of highly luminescent CdSe-Core CdS/Zn0. 5Cd0. 5S/ZnS multishell nanocrystals. *Journal of the American Chemical Society* **127**, 7480-7488 (2005).
104 Kim, S., Fisher, B., Eisler, H.-J. & Bawendi, M. Type-II quantum dots: CdTe/CdSe (core/shell) and CdSe/ZnTe (core/shell) heterostructures. *Journal of the American Chemical Society* **125**, 11466-11467 (2003).

105 Yu, K., Zaman, B., Romanova, S., Wang, D.-s. & Ripmeester, J. A. Sequential synthesis of type II colloidal CdTe/CdSe core-shell nanocrystals. *Small* **1**, 332-338 (2005).
106 Schöps, O., Le Thomas, N., Woggon, U. & Artemyev, M. Recombination dynamics of CdTe/CdS core-shell nanocrystals. *The Journal of Physical Chemistry B* **110**, 2074-2079 (2006).
107 Ivanov, S. A. *et al.* Light amplification using inverted core/shell nanocrystals: Towards lasing in the single-exciton regime. *The Journal of Physical Chemistry B* **108**, 10625-10630 (2004).
108 Ivanov, S. A. *et al.* Type-II core/shell CdS/ZnSe nanocrystals: synthesis, electronic structures, and spectroscopic properties. *J Am Chem Soc* **129**, 11708-11719 (2007).
109 Murray, C. B., Kagan, C. & Bawendi, M. Synthesis and characterization of monodisperse nanocrystals and close-packed nanocrystal assemblies. *Annual Review of Materials Science* **30**, 545-610 (2000).
110 Efros, A. L. & Rosen, M. The Electronic Structure of Semiconductor Nanocrystals 1. *Annual Review of Materials Science* **30**, 475-521 (2000).
111 Klimov, V. I. Mechanisms for photogeneration and recombination of multiexcitons in semiconductor nanocrystals: implications for lasing and solar energy conversion. *The Journal of Physical Chemistry B* **110**, 16827-16845 (2006).
112 Schlamp, M., Peng, X. & Alivisatos, A. Improved efficiencies in light emitting diodes made with CdSe (CdS) core/shell type nanocrystals and a semiconducting polymer. *Journal of Applied Physics* **82**, 5837-5842 (1997).
113 Mattoussi, H. *et al.* Electroluminescence from heterostructures of poly (phenylene vinylene) and inorganic CdSe nanocrystals. *Journal of applied physics* **83**, 7965-7974 (1998).
114 Steckel, J. S. *et al.* Color-Saturated Green-Emitting QD-LEDs. *Angewandte Chemie International Edition* **45**, 5796-5799 (2006).
115 Steckel, J. S., Coe-Sullivan, S., Bulović, V. & Bawendi, M. G. 1.3 μm to 1.55 μm tunable electroluminescence from PbSe quantum dots embedded within an organic device. *Advanced Materials* **15**, 1862-1866 (2003).
116 Anikeeva, P. O., Halpert, J. E., Bawendi, M. G. & Bulovic, V. Electroluminescence from a mixed red-green-blue colloidal quantum dot monolayer. *Nano Letters* **7**, 2196-2200 (2007).
117 Sun, Q. *et al.* Bright, multicoloured light-emitting diodes based on quantum dots. *Nature Photonics* **1**, 717-722 (2007).
118 Robel, I., Subramanian, V., Kuno, M. & Kamat, P. V. Quantum dot solar cells. Harvesting light energy with CdSe nanocrystals molecularly linked to mesoscopic TiO2 films. *Journal of the American Chemical Society* **128**, 2385-2393 (2006).
119 Plass, R., Pelet, S., Krueger, J., Grätzel, M. & Bach, U. Quantum dot sensitization of organic-inorganic hybrid solar cells. *The Journal of Physical Chemistry B* **106**, 7578-7580 (2002).
120 Alivisatos, A. P., Gu, W. & Larabell, C. Quantum dots as cellular probes. *Annu. Rev. Biomed. Eng.* **7**, 55-76 (2005).

121 Alivisatos, P. The use of nanocrystals in biological detection. *Nature biotechnology* **22**, 47-52 (2003).
122 Chan, W. C. *et al.* Luminescent quantum dots for multiplexed biological detection and imaging. *Current opinion in biotechnology* **13**, 40-46 (2002).
123 Michalet, X. *et al.* Quantum dots for live cells, in vivo imaging, and diagnostics. *Science* **307**, 538-544 (2005).
124 Medintz, I. L., Uyeda, H. T., Goldman, E. R. & Mattoussi, H. Quantum dot bioconjugates for imaging, labelling and sensing. *Nature materials* **4**, 435-446 (2005).
125 Schröck, E. *et al.* Multicolor spectral karyotyping of human chromosomes. *Science* **273**, 494-497 (1996).
126 Hermanson, G. T. *Bioconjugate techniques*. (Academic press, 1996).
127 Roederer, M. *et al.* 8 color, 10-parameter flow cytometry to elucidate complex leukocyte heterogeneity. *Cytometry* **29**, 328-339 (1997).
128 Jaiswal, J. K., Mattoussi, H., Mauro, J. M. & Simon, S. M. Long-term multiple color imaging of live cells using quantum dot bioconjugates. *Nature Biotechnology* **21**, 47-51 (2002).
129 Gerion, D. *et al.* Synthesis and Properties of Biocompatible Water-Soluble Silica-Coated CdSe/ZnS Semiconductor Quantum Dots†. *The Journal of Physical Chemistry B* **105**, 8861-8871 (2001).
130 Pietryga, J. M. *et al.* Pushing the band gap envelope: mid-infrared emitting colloidal PbSe quantum dots. *Journal of the American Chemical Society* **126**, 11752-11753 (2004).
131 Smith, A. M., Dave, S., Nie, S., True, L. & Gao, X. Multicolor quantum dots for molecular diagnostics of cancer. (2006).
132 Zhang, H. *et al.* Hydrothermal Synthesis for High-Quality CdTe Nanocrystals. *Advanced Materials* **15**, 1712-1715 (2003).
133 Rogach, A. L. *et al.* Aqueous synthesis of thiol-capped CdTe nanocrystals: state-of-the-art. *The Journal of Physical Chemistry C* **111**, 14628-14637 (2007).
134 Mitchell, G. P., Mirkin, C. A. & Letsinger, R. L. Programmed assembly of DNA functionalized quantum dots. *Journal of the American Chemical Society* **121**, 8122-8123 (1999).
135 Mattoussi, H. *et al.* Self-assembly of CdSe-ZnS quantum dot bioconjugates using an engineered recombinant protein. *Journal of the American Chemical Society* **122**, 12142-12150 (2000).
136 Susumu, K. *et al.* Enhancing the stability and biological functionalities of quantum dots via compact multifunctional ligands. *Journal of the American Chemical Society* **129**, 13987-13996 (2007).
137 Smith, A. M. & Nie, S. Minimizing the Hydrodynamic Size of Quantum Dots with Multifunctional Multidentate Polymer Ligands. *Journal of the American Chemical Society* **130**, 11278-11279, doi:10.1021/ja804306c (2008).
138 Dubertret, B. *et al.* In vivo imaging of quantum dots encapsulated in phospholipid micelles. *Science* **298**, 1759-1762 (2002).
139 Wu, X. *et al.* Immunofluorescent labeling of cancer marker Her2 and other cellular targets with semiconductor quantum dots. *Nature biotechnology* **21**, 41-46 (2002).

140 Duan, H. & Nie, S. Cell-penetrating quantum dots based on multivalent and endosome-disrupting surface coatings. *Journal of the American Chemical Society* **129**, 3333-3338 (2007).
141 Yu, X. *et al.* Immunofluorescence detection with quantum dot bioconjugates for hepatoma in vivo. *Journal of Biomedical Optics* **12**, 014008-014008-014005 (2007).
142 Yu, W. W. *et al.* Forming biocompatible and nonaggregated nanocrystals in water using amphiphilic polymers. *Journal of the American Chemical Society* **129**, 2871-2879 (2007).
143 Pellegrino, T. *et al.* Hydrophobic nanocrystals coated with an amphiphilic polymer shell: a general route to water soluble nanocrystals. *Nano Letters* **4**, 703-707 (2004).
144 Kairdolf, B. A., Smith, A. M. & Nie, S. One-pot synthesis, encapsulation, and solubilization of size-tuned quantum dots with amphiphilic multidentate ligands. *Journal of the American Chemical Society* **130**, 12866-12867 (2008).
145 Sapsford, K. E. *et al.* Kinetics of metal-affinity driven self-assembly between proteins or peptides and CdSe-ZnS quantum dots. *The Journal of Physical Chemistry C* **111**, 11528-11538 (2007).
146 Pinaud, F., King, D., Moore, H.-P. & Weiss, S. Bioactivation and cell targeting of semiconductor CdSe/ZnS nanocrystals with phytochelatin-related peptides. *Journal of the American Chemical Society* **126**, 6115-6123 (2004).
147 Klimov, V. I. *Nanocrystal Quantum Dots*. (CRC Press, 2010).
148 Lagerholm, B. C. *et al.* Multicolor Coding of Cells with Cationic Peptide Coated Quantum Dots. *Nano Letters* **4**, 2019-2022, doi:10.1021/nl049295v (2004).
149 Delehanty, J. B. *et al.* Self-assembled quantum dot-peptide bioconjugates for selective intracellular delivery. *Bioconjugate chemistry* **17**, 920-927 (2006).
150 Ruan, G., Agrawal, A., Marcus, A. I. & Nie, S. Imaging and tracking of tat peptide-conjugated quantum dots in living cells: new insights into nanoparticle uptake, intracellular transport, and vesicle shedding. *Journal of the American Chemical Society* **129**, 14759-14766 (2007).
151 Bharali, D. J., Lucey, D. W., Jayakumar, H., Pudavar, H. E. & Prasad, P. N. Folate-receptor-mediated delivery of InP quantum dots for bioimaging using confocal and two-photon microscopy. *Journal of the American Chemical Society* **127**, 11364-11371 (2005).
152 Lidke, D. S. *et al.* Quantum dot ligands provide new insights into erbB/HER receptor–mediated signal transduction. *Nature biotechnology* **22**, 198-203 (2004).
153 Anikeeva, N. *et al.* Quantum dot/peptide-MHC biosensors reveal strong CD8-dependent cooperation between self and viral antigens that augment the T cell response. *Proceedings of the National Academy of Sciences* **103**, 16846-16851 (2006).
154 Zhang, T. *et al.* Cellular Effect of High Doses of Silica-Coated Quantum Dot Profiled with High Throughput Gene Expression Analysis and High Content Cellomics Measurements. *Nano Letters* **6**, 800-808, doi:10.1021/nl0603350 (2006).

155 Derfus, A. M., Chan, W. C. & Bhatia, S. N. Intracellular delivery of quantum dots for live cell labeling and organelle tracking. *Advanced Materials* **16**, 961-966 (2004).
156 Voura, E. B., Jaiswal, J. K., Mattoussi, H. & Simon, S. M. Tracking metastatic tumor cell extravasation with quantum dot nanocrystals and fluorescence emission-scanning microscopy. *Nature medicine* **10**, 993-998 (2004).
157 Larson, D. R. *et al.* Water-soluble quantum dots for multiphoton fluorescence imaging in vivo. *Science* **300**, 1434-1436 (2003).
158 Kim, S. *et al.* Near-infrared fluorescent type II quantum dots for sentinel lymph node mapping. *Nature biotechnology* **22**, 93-97 (2003).
159 Choi, H. S. *et al.* Renal clearance of quantum dots. *Nature biotechnology* **25**, 1165-1170 (2007).
160 Courty, S., Luccardini, C., Bellaiche, Y., Cappello, G. & Dahan, M. Tracking Individual Kinesin Motors in Living Cells Using Single Quantum-Dot Imaging. *Nano Letters* **6**, 1491-1495, doi:10.1021/nl060921t (2006).
161 Cho, S. J. *et al.* Long-term exposure to CdTe quantum dots causes functional impairments in live cells. *Langmuir* **23**, 1974-1980 (2007).
162 Allen, J. A., Halverson-Tamboli, R. A. & Rasenick, M. M. Lipid raft microdomains and neurotransmitter signalling. *Nature Reviews Neuroscience* **8**, 128-140 (2007).
163 Chang, J. C. & Rosenthal, S. J. Visualization of lipid raft membrane compartmentalization in living RN46A neuronal cells using single quantum dot tracking. *ACS chemical neuroscience* **3**, 737-743 (2012).
164 Cui, B. *et al.* One at a time, live tracking of NGF axonal transport using quantum dots. *Proceedings of the National Academy of Sciences* **104**, 13666-13671 (2007).
165 Zhang, Q., Li, Y. & Tsien, R. W. The dynamic control of kiss-and-run and vesicular reuse probed with single nanoparticles. *Science* **323**, 1448-1453 (2009).
166 Lowe, A. R. *et al.* Selectivity mechanism of the nuclear pore complex characterized by single cargo tracking. *Nature* **467**, 600-603 (2010).
167 Mahler, B. *et al.* Towards non-blinking colloidal quantum dots. *Nature materials* **7**, 659-664 (2008).
168 Efros, A. L. & Rosen, M. Random telegraph signal in the photoluminescence intensity of a single quantum dot. *Physical Review Letters* **78**, 1110 (1997).
169 Moerner, W. & Orrit, M. Illuminating single molecules in condensed matter. *Science* **283**, 1670-1676 (1999).
170 ALIVISATOS, A. Semiconductor clusters, nanocrystals, and quantum dots: Clusters. *Science* **271**, 933-937 (1996).
171 Kuno, M., Fromm, D., Hamann, H., Gallagher, A. & Nesbitt, D. "On"/"off" fluorescence intermittency of single semiconductor quantum dots. *The Journal of Chemical Physics* **115**, 1028-1040 (2001).
172 Lounis, B. & Moerner, W. Single photons on demand from a single molecule at room temperature. *Nature* **407**, 491-493 (2000).
173 García-Santamaría, F. *et al.* Suppressed auger recombination in "giant" nanocrystals boosts optical gain performance. *Nano letters* **9**, 3482-3488 (2009).

174 Empedocles, S. A., Norris, D. & Bawendi, M. Photoluminescence spectroscopy of single CdSe nanocrystallite quantum dots. *Physical Review Letters* **77**, 3873-3876 (1996).
175 Kuno, M., Fromm, D., Hamann, H., Gallagher, A. & Nesbitt, D. Nonexponential "blinking" kinetics of single CdSe quantum dots: A universal power law behavior. *The journal of chemical physics* **112**, 3117-3120 (2000).
176 Shimizu, K. *et al.* Blinking statistics in single semiconductor nanocrystal quantum dots. *Physical Review B* **63**, 205316 (2001).
177 Cichos, F., Von Borczyskowski, C. & Orrit, M. Power-law intermittency of single emitters. *Current Opinion in Colloid & Interface Science* **12**, 272-284 (2007).
178 Kuno, M., Fromm, D., Johnson, S., Gallagher, A. & Nesbitt, D. Modeling distributed kinetics in isolated semiconductor quantum dots. *Physical Review B* **67**, 125304 (2003).
179 Chepic, D. *et al.* Auger ionization of semiconductor quantum drops in a glass matrix. *Journal of Luminescence* **47**, 113-127 (1990).
180 Klimov, V., Mikhailovsky, A., McBranch, D., Leatherdale, C. & Bawendi, M. Quantization of multiparticle Auger rates in semiconductor quantum dots. *Science* **287**, 1011-1013 (2000).
181 Jha, P. P. & Guyot-Sionnest, P. Trion decay in colloidal quantum dots. *Acs Nano* **3**, 1011-1015 (2009).
182 Zhang, K., Chang, H., Fu, A., Alivisatos, A. P. & Yang, H. Continuous distribution of emission states from single CdSe/ZnS quantum dots. *Nano letters* **6**, 843-847 (2006).
183 Margolin, G., Protasenko, V., Kuno, M. & Barkai, E. Photon counting statistics for blinking CdSe-ZnS quantum dots: A lévy walk process. *The Journal of Physical Chemistry B* **110**, 19053-19060 (2006).
184 Tang, J. & Marcus, R. Mechanisms of fluorescence blinking in semiconductor nanocrystal quantum dots. *The Journal of chemical physics* **123**, 054704-054704-054712 (2005).
185 Frantsuzov, P. A. & Marcus, R. Explanation of quantum dot blinking without long-lived trap hypothesis. *arXiv preprint cond-mat/0505604* (2005).
186 Frantsuzov, P. A., Volkán-Kacsó, S. & Jankó, B. Model of fluorescence intermittency of single colloidal semiconductor quantum dots using multiple recombination centers. *Physical review letters* **103**, 207402 (2009).
187 Pelton, M., Smith, G., Scherer, N. F. & Marcus, R. A. Evidence for a diffusion-controlled mechanism for fluorescence blinking of colloidal quantum dots. *Proceedings of the National Academy of Sciences* **104**, 14249-14254 (2007).
188 Jones, M., Lo, S. S. & Scholes, G. D. Quantitative modeling of the role of surface traps in CdSe/CdS/ZnS nanocrystal photoluminescence decay dynamics. *Proceedings of the National Academy of Sciences* **106**, 3011-3016 (2009).
189 Shimizu, K., Woo, W., Fisher, B., Eisler, H. & Bawendi, M. Surface-enhanced emission from single semiconductor nanocrystals. *Physical review letters* **89**, 117401 (2002).
190 Fu, Y., Zhang, J. & Lakowicz, J. R. Suppressed blinking in single quantum dots (QDs) immobilized near silver island films (SIFs). *Chemical physics letters* **447**, 96-100 (2007).

191 Nirmal, M. & Brus, L. Luminescence Photophysics in Semiconductor Nanocrystals. *Accounts of Chemical Research* **32**, 407-414, doi:10.1021/ar9700320 (1998).
192 Riddoch, F. A. & Jaros, M. Auger recombination cross section associated with deep traps in semiconductors. *Journal of Physics C: Solid State Physics* **13**, 6181 (1980).
193 Molina, S. I. *et al.* Strain relief in linearly graded composition buffer layers: A design scheme to grow dislocation-free (< 10[sup 5] cm[sup - 2]) and unstrained epilayers. *Applied Physics Letters* **65**, 2460-2462 (1994).
194 Tersoff, J. Dislocations and strain relief in compositionally graded layers. *Applied Physics Letters* **62**, 693-695 (1993).
195 Heyes, C. D., Kobitski, A. Y., Breus, V. V. & Nienhaus, G. U. Effect of the shell on the blinking statistics of core-shell quantum dots: A single-particle fluorescence study. *Physical Review B* **75**, 125431 (2007).
196 Wang, R., Zhang, Y., Gan, C., Muhammad, J. & Xiao, M. Controlling blinking in multilayered quantum dots. *Applied Physics Letters* **96**, 151107-151107-151103 (2010).
197 Matthews, J. W. & Blakeslee, A. E. Defects in epitaxial multilayers: I. Misfit dislocations. *Journal of Crystal Growth* **27**, 118-125 (1974).
198 Fitzgerald, E. A. *et al.* 4 edn 1807-1819 (AVS).
199 Adachi, S. Vol. 3 (Kluwer Academic Publishers, 2004).
200 Yong-Ji, L., Tae-Geun, K. & Yun-Mo, S. Lattice distortion and luminescence of CdSe/ZnSe nanocrystals. *Nanotechnology* **17**, 3539 (2006).
201 Smith, A. M., Mohs, A. M. & Nie, S. Tuning the optical and electronic properties of colloidal nanocrystals by lattice strain. *Nat Nano* **4**, 56-63 (2009).
202 Orrit, M. & Basché, T. Steady light from quantum dots, at last. But how? *ChemPhysChem* **10**, 2383-2385 (2009).
203 Spinicelli, P. *et al.* Bright and grey states in CdSe-CdS nanocrystals exhibiting strongly reduced blinking. *Physical review letters* **102**, 136801 (2009).
204 Schooss, D., Mews, A., Eychmüller, A. & Weller, H. Quantum-dot quantum well CdS/HgS/CdS: Theory and experiment. *Physical Review B* **49**, 17072-17078 (1994).
205 Oron, D., Kazes, M. & Banin, U. Multiexcitons in type-II colloidal semiconductor quantum dots. *Physical Review B* **75**, 035330 (2007).
206 Dennis, A. M. *et al.* Suppressed Blinking and Auger Recombination in Near-Infrared Type-II InP/CdS Nanocrystal Quantum Dots. *Nano letters* **12**, 5545-5551 (2012).
207 Mahler, B. *et al.* Towards non-blinking colloidal quantum dots. *Nat Mater* **7**, 659-664 (2008).
208 Osovsky, R. *et al.* Continuous-wave pumping of multiexciton bands in the photoluminescence spectrum of a single CdTe-CdSe core-shell colloidal quantum dot. *Physical review letters* **102**, 197401 (2009).
209 García-Santamaría, F. *et al.* Breakdown of volume scaling in Auger recombination in CdSe/CdS heteronanocrystals: the role of the core− shell interface. *Nano letters* **11**, 687-693 (2011).

210 Yu, W. W. & Peng, X. Formation of High-Quality CdS and Other II–VI Semiconductor Nanocrystals in Noncoordinating Solvents: Tunable Reactivity of Monomers. *Angewandte Chemie International Edition* **41**, 2368-2371 (2002).
211 Peng, Z. A. & Peng, X. Formation of High-Quality CdTe, CdSe, and CdS Nanocrystals Using CdO as Precursor. *Journal of the American Chemical Society* **123**, 183-184 (2000).
212 Nose, K. *et al.* Chemical role of amines in the colloidal synthesis of CdSe quantum dots and their luminescence properties. *Journal of Luminescence* **126**, 21-26 (2007).
213 Talapin, D. V., Rogach, A. L., Kornowski, A., Haase, M. & Weller, H. Highly Luminescent Monodisperse CdSe and CdSe/ZnS Nanocrystals Synthesized in a Hexadecylamine−Trioctylphosphine Oxide−Trioctylphospine Mixture. *Nano Letters* **1**, 207-211 (2001).
214 Yu, W. W., Qu, L., Guo, W. & Peng, X. Experimental determination of the extinction coefficient of CdTe, CdSe, and CdS nanocrystals. *Chemistry of Materials* **15**, 2854-2860 (2003).
215 Jasieniak, J., Smith, L., Embden, J. v., Mulvaney, P. & Califano, M. Re-examination of the Size-Dependent Absorption Properties of CdSe Quantum Dots. *The Journal of Physical Chemistry C* **113**, 19468-19474 (2009).
216 Jasieniak, J., Bullen, C., van Embden, J. & Mulvaney, P. Phosphine-Free Synthesis of CdSe Nanocrystals. *The Journal of Physical Chemistry B* **109**, 20665-20668 (2005).
217 Bullen, C. *et al.* High Activity Phosphine-Free Selenium Precursor Solution for Semiconductor Nanocrystal Growth. *Chemistry of Materials* **22**, 4135-4143 (2010).
218 Mahler, B. t., Lequeux, N. & Dubertret, B. t. Ligand-Controlled Polytypism of Thick-Shell CdSe/CdS Nanocrystals. *Journal of the American Chemical Society* **132**, 953-959 (2009).
219 Ghosh, Y. *et al.* New Insights into the Complexities of Shell Growth and the Strong Influence of Particle Volume in Nonblinking "Giant" Core/Shell Nanocrystal Quantum Dots. *Journal of the American Chemical Society* **134**, 9634-9643 (2012).
220 Uyeda, H. T., Medintz, I. L., Jaiswal, J. K., Simon, S. M. & Mattoussi, H. Synthesis of Compact Multidentate Ligands to Prepare Stable Hydrophilic Quantum Dot Fluorophores. *Journal of the American Chemical Society* **127**, 3870-3878 (2005).
221 Mei, B. C., Susumu, K., Medintz, I. L., Delehanty, J. B. & Mattoussi, H. New ligand design to promote water compatibility of luminescent quantum dots and gold nanoparticles. 686606-686606 (2008).
222 Clapp, A. R., Goldman, E. R. & Mattoussi, H. Capping of CdSe-ZnS quantum dots with DHLA and subsequent conjugation with proteins. *Nat. Protocols* **1**, 1258-1266 (2006).
223 Mei, B. C., Susumu, K., Medintz, I. L., Delehanty, J. B. & Mattoussi, H. in *Proceedings of SPIE, the International Society for Optical Engineering.* 686606.686601-686606.686610 (Society of Photo-Optical Instrumentation Engineers).

224 KANG *et al. Preparation of water-soluble PEGylated semiconductor nanocrystals*. Vol. 33 (Chemical Society of Japan, 2004).
225 Xie, X. S. Single-molecule spectroscopy and dynamics at room temperature. *Accounts of chemical research* **29**, 598-606 (1996).
226 Xie, X. S. & Trautman, J. K. Optical studies of single molecules at room temperature. *Annual review of physical chemistry* **49**, 441-480 (1998).
227 Moerner, W. A dozen years of single-molecule spectroscopy in physics, chemistry, and biophysics. *The Journal of Physical Chemistry B* **106**, 910-927 (2002).
228 Chung, I. & Bawendi, M. G. Relationship between single quantum-dot intermittency and fluorescence intensity decays from collections of dots. *Physical Review B* **70**, 165304 (2004).
229 Jin, S., Song, N. & Lian, T. Suppressed Blinking Dynamics of Single QDs on ITO. *ACS Nano* **4**, 1545-1552 (2010).
230 Fisher, B. R., Eisler, H.-J., Stott, N. E. & Bawendi, M. G. Emission Intensity Dependence and Single-Exponential Behavior In Single Colloidal Quantum Dot Fluorescence Lifetimes. *The Journal of Physical Chemistry B* **108**, 143-148 (2003).
231 Saxton, M. J. & Jacobson, K. Single-particle tracking: applications to membrane dynamics. *Annual review of biophysics and biomolecular structure* **26**, 373-399 (1997).
232 Pinaud, F., Clarke, S., Sittner, A. & Dahan, M. Probing cellular events, one quantum dot at a time. *Nature methods* **7**, 275-285 (2010).
233 Wieser, S. & Schütz, G. J. Tracking single molecules in the live cell plasma membrane—Do's and Don't's. *Methods* **46**, 131-140 (2008).
234 Brameshuber, M. & Schütz, G. J. How the sum of its parts gets greater than the whole. *Nature Methods* **5**, 133-134 (2008).
235 Alcor, D., Gouzer, G. & Triller, A. Single-particle tracking methods for the study of membrane receptors dynamics. *European Journal of Neuroscience* **30**, 987-997 (2009).
236 Owen, D. M., Williamson, D., Rentero, C. & Gaus, K. Quantitative microscopy: protein dynamics and membrane organisation. *Traffic* **10**, 962-971 (2009).
237 Fujiwara, T., Ritchie, K., Murakoshi, H., Jacobson, K. & Kusumi, A. Phospholipids undergo hop diffusion in compartmentalized cell membrane. *The Journal of cell biology* **157**, 1071-1082 (2002).
238 Itano, M. S. *et al.* DC-SIGN and influenza hemagglutinin dynamics in plasma membrane microdomains are markedly different. *Biophysical journal* **100**, 2662-2670 (2011).
239 Jaqaman, K. *et al.* Cytoskeletal control of CD36 diffusion promotes its receptor and signaling function. *Cell* **146**, 593-606 (2011).
240 Wieser, S., Weghuber, J., Sams, M., Stockinger, H. & Schütz, G. J. Cell-to-cell variability in the diffusion constants of the plasma membrane proteins CD59 and CD147. *Soft Matter* **5**, 3287-3294 (2009).
241 Chen, Y., Thelin, W. R., Yang, B., Milgram, S. L. & Jacobson, K. Transient anchorage of cross-linked glycosyl-phosphatidylinositol–anchored proteins

depends on cholesterol, Src family kinases, caveolin, and phosphoinositides. *The Journal of cell biology* **175**, 169-178 (2006).
242 Kusumi, A., Sako, Y. & Yamamoto, M. Confined lateral diffusion of membrane receptors as studied by single particle tracking (nanovid microscopy). Effects of calcium-induced differentiation in cultured epithelial cells. *Biophysical journal* **65**, 2021-2040 (1993).
243 Jacobson, K., Mouritsen, O. G. & Anderson, R. G. Lipid rafts: at a crossroad between cell biology and physics. *Nature cell biology* **9**, 7-14 (2007).
244 P Clausen, M. & Christoffer Lagerholm, B. The probe rules in single particle tracking. *Current Protein and Peptide Science* **12**, 699-713 (2011).
245 Betzig, E. Proposed method for molecular optical imaging. *Optics letters* **20**, 237-239 (1995).
246 Lee, J. *et al.* Characterization and Cancer Cell Specific Binding Properties of Anti-EGFR Antibody Conjugated Quantum Dots. *Bioconjugate Chemistry* **21**, 940-946 (2010).
247 Worden, J. G., Shaffer, A. W. & Huo, Q. Controlled functionalization of gold nanoparticles through a solid phase synthesis approach. *Chemical communications*, 518-519 (2004).
248 Sung, K.-M., Mosley, D. W., Peelle, B. R., Zhang, S. & Jacobson, J. M. Synthesis of monofunctionalized gold nanoparticles by Fmoc solid-phase reactions. *Journal of the American Chemical Society* **126**, 5064-5065 (2004).
249 Lévy, R. *et al.* A Generic Approach to Monofunctionalized Protein-Like Gold Nanoparticles Based on Immobilized Metal Ion Affinity Chromatography. *ChemBioChem* **7**, 592-594 (2006).
250 Fu, A. *et al.* Discrete nanostructures of quantum dots/Au with DNA. *Journal of the American Chemical Society* **126**, 10832-10833 (2004).
251 Pons, T., Medintz, I. L., Wang, X., English, D. S. & Mattoussi, H. Solution-phase single quantum dot fluorescence resonance energy transfer. *Journal of the American Chemical Society* **128**, 15324-15331 (2006).
252 Bannai, H., Lévi, S., Schweizer, C., Dahan, M. & Triller, A. Imaging the lateral diffusion of membrane molecules with quantum dots. *Nature protocols* **1**, 2628-2634 (2007).
253 Saxton, M. J. Anomalous diffusion due to obstacles: a Monte Carlo study. *Biophysical journal* **66**, 394-401 (1994).
254 Powles, J., Mallett, M., Rickayzen, G. & Evans, W. Exact analytic solutions for diffusion impeded by an infinite array of partially permeable barriers. *Proceedings of the Royal Society of London. Series A: Mathematical and Physical Sciences* **436**, 391-403 (1992).
255 Dietrich, C., Yang, B., Fujiwara, T., Kusumi, A. & Jacobson, K. Relationship of lipid rafts to transient confinement zones detected by single particle tracking. *Biophysical journal* **82**, 274-284 (2002).
256 Triantafilou, M., Morath, S., Mackie, A., Hartung, T. & Triantafilou, K. Lateral diffusion of Toll-like receptors reveals that they are transiently confined within lipid rafts on the plasma membrane. *Journal of cell science* **117**, 4007-4014 (2004).

257 Clausen, M. P. & Lagerholm, B. C. Visualization of Plasma Membrane Compartmentalization by High-Speed Quantum Dot Tracking. *Nano Letters* **13**, 2332-2337 (2013).
258 Pike, L. J. The challenge of lipid rafts. *Journal of lipid research* **50**, S323-S328 (2009).
259 Kung, C. E. & Reed, J. K. Microviscosity measurements of phospholipid bilayers using fluorescent dyes that undergo torsional relaxation. *Biochemistry* **25**, 6114-6121 (1986).
260 Kural, C. *et al.* Kinesin and dynein move a peroxisome in vivo: a tug-of-war or coordinated movement? *Science* **308**, 1469-1472 (2005).
261 Domke, J., Parak, W. J., George, M., Gaub, H. E. & Radmacher, M. Mapping the mechanical pulse of single cardiomyocytes with the atomic force microscope. *European Biophysics Journal* **28**, 179-186 (1999).
262 Qian, H., Sheetz, M. P. & Elson, E. L. Single particle tracking. Analysis of diffusion and flow in two-dimensional systems. *Biophysical journal* **60**, 910-921 (1991).
263 Bae, W. K. *et al.* Controlled Alloying of the Core–Shell Interface in CdSe/CdS Quantum Dots for Suppression of Auger Recombination. *ACS nano* **7**, 3411-3419 (2013).
264 Van Schooneveld, M. M. *et al.* Imaging and quantifying the morphology of an organic-inorganic nanoparticle at the sub-nanometre level. *Nature nanotechnology* **5**, 538-544 (2010).
265 De Caro, L., Carlino, E., Caputo, G., Cozzoli, P. D. & Giannini, C. Electron diffractive imaging of oxygen atoms in nanocrystals at sub-Ångström resolution. *Nature nanotechnology* **5**, 360-365 (2010).
266 Li, Y., Ye, M., Yang, C., Li, X. & Li, Y. Composition-and Shape-Controlled Synthesis and Optical Properties of ZnxCd1–xS Alloyed Nanocrystals. *Advanced Functional Materials* **15**, 433-441 (2005).
267 Kumah, D. P., Shusterman, S., Paltiel, Y., Yacoby, Y. & Clarke, R. Atomic-scale mapping of quantum dots formed by droplet epitaxy. *Nature nanotechnology* **4**, 835-838 (2009).
268 Rosenthal, S. J., McBride, J., Pennycook, S. J. & Feldman, L. C. Synthesis, surface studies, composition and structural characterization of CdSe, core/shell and biologically active nanocrystals. *Surface science reports* **62**, 111-157 (2007).
269 Choi, H., Ko, J.-H., Kim, Y.-H. & Jeong, S. Steric-Hindrance-Driven Shape Transition in PbS Quantum Dots: Understanding Size-Dependent Stability. *Journal of the American Chemical Society* **135**, 5278-5281 (2013).
270 Wei, H. H.-Y. *et al.* Colloidal semiconductor quantum dots with tunable surface composition. *Nano letters* **12**, 4465-4471 (2012).
271 Jung, K.-W. *et al.* Quantitative Compositional Profiling of Conjugated Quantum Dots with Single Atomic Layer Depth Resolution via Time-of-Flight Medium-Energy Ion Scattering Spectroscopy. *Analytical Chemistry* **86**, 1091-1097, doi:10.1021/ac402753j (2013).
272 Fairclough, S. M. *et al.* Growth and Characterization of Strained and Alloyed Type-II ZnTe/ZnSe Core–Shell Nanocrystals. *The Journal of Physical Chemistry C* **116**, 26898-26907 (2012).

273 Howarth, M. *et al.* Monovalent, reduced-size quantum dots for imaging receptors on living cells. *Nature methods* **5**, 397-399 (2008).
274 Banerjee, D., Liu, A. P., Voss, N. R., Schmid, S. L. & Finn, M. Multivalent Display and Receptor-Mediated Endocytosis of Transferrin on Virus-Like Particles. *ChemBioChem* **11**, 1273-1279 (2010).
275 Clarke, S. *et al.* Covalent monofunctionalization of peptide-coated quantum dots for single-molecule assays. *Nano letters* **10**, 2147-2154 (2010).
276 You, C. *et al.* Self-Controlled Monofunctionalization of Quantum Dots for Multiplexed Protein Tracking in Live Cells. *Angewandte Chemie International Edition* **49**, 4108-4112 (2010).
277 Tikhomirov, G. *et al.* DNA-based programming of quantum dot valency, self-assembly and luminescence. *Nature nanotechnology* **6**, 485-490 (2011).
278 You, C. *et al.* Electrostatically Controlled Quantum Dot Monofunctionalization for Interrogating the Dynamics of Protein Complexes in Living Cells. *ACS chemical biology* **8**, 320-326 (2012).
279 Farlow, J. *et al.* Formation of targeted monovalent quantum dots by steric exclusion. *Nature Methods* **10**, 1203-1205 (2013).
280 Montenegro, J.-M. *et al.* Controlled antibody/(bio-) conjugation of inorganic nanoparticles for targeted delivery. *Advanced drug delivery reviews* **65**, 677-688 (2013).
281 Chen, Y., Yang, B. & Jacobson, K. Transient confinement zones: a type of lipid raft? *Lipids* **39**, 1115-1119 (2004).
282 Sheets, E. D., Lee, G. M., Simson, R. & Jacobson, K. Transient confinement of a glycosylphosphatidylinositol-anchored protein in the plasma membrane. *Biochemistry* **36**, 12449-12458 (1997).
283 Murase, K. *et al.* Ultrafine membrane compartments for molecular diffusion as revealed by single molecule techniques. *Biophysical journal* **86**, 4075-4093 (2004).
284 Umemura, Y. M. *et al.* Both MHC class II and its GPI-anchored form undergo hop diffusion as observed by single-molecule tracking. *Biophysical journal* **95**, 435-450 (2008).
285 Kusumi, A. *et al.* Paradigm shift of the plasma membrane concept from the two-dimensional continuum fluid to the partitioned fluid: high-speed single-molecule tracking of membrane molecules. *Annu. Rev. Biophys. Biomol. Struct.* **34**, 351-378 (2005).

VITA

LANE, LUCAS A

1760 Haygood Drive, Ste. E-100, Atlanta, GA 30322 **email:llane6@gatech.edu**

EDUCATION

Georgia Institute of Technology
Doctorate of Philosophy, Bioengineering FL 2009 – SU 2014
Dissertation: Advancement of Blinking Suppressed Quantum Dots for Enhanced Single Molecule Imaging
Advisor: Shuming Nie
Minor: Nonlinear and Applied Mathematics

Washington University in Saint Louis
B.S. Applied Science FL 2006 – SP 2009
Areas of Concentration: Chemical and Biomedical Engineering, Applied Mathematics, Physics

AWARDS

2nd Place Student Paper Competition AIChE Mid-America 2009
Best Poster Award Georgia Tech Institute for Electronics and Nanotechnology 2013

PUBLICATIONS

Formo E, Yavuz MS, Lee EP, **Lane L**, Xia Y. Functionalization of Electrospun Ceramic Nanofiber Membranes with Nobel-Metal Nanostructures for Catalytic Applications. *Journal of Materials Chemistry*, **2009**.

Smith AM, **Lane LA**, Nie S. Mapping the Spatial Distribution of Charge Carriers in Quantum-Confined Heterostructures. *Nature Communications,* **accepted**

Lane LA, Smith AM, Nie S. Compact and Blinking-Suppressed Quantum Dots: New Insights into the Mechanisms of Blinking. *Journal of the American Chemical Society,* **in preparation**

Lane LA, Smith AM, T. Lian, Nie S. Compact and Blinking-Suppressed Quantum Dots for Single Particle Tracking in Live Cells. *Journal of Physical Chemistry B,* **submitted**

Lane LA and Nie S. Quantum Dot Blinking: Fundamental Mechanisms and Suppression Strategies. *ACS Nano,* **in preparation**

Lane LA, Qian X, Nie S. Physical Chemistry of Nanomedicine. *Annual Review of Physical Chemistry,* **in preparation**

Lane LA, Qian X, Dai Y, Yang Z, Nie S. Hydrophobic Locking for Bright SERS Nanoparticles, Increasing Signal Intensity and Stability. *Journal of the American Chemical Society,* **in preparation**

Lane LA, Qian X, Zhou K, Nie S. Stabilizing and Detoxifying Silver Nanostructures for Cellular and In Vivo Applications. *ACS Nano,* **in preparation**